Multiphase Wireless Dynamic Charging Systems for Electric Vehicles

Van Binh Vu

B.Sc., M.Sc.

A thesis submitted for the degree of
Doctor of Philosophy

May 2020

School of Engineering

Newcastle University
United Kingdom

ABSTRACT

Electric vehicles (EVs) have been intensively developed as an attempt to reduce carbon-dioxide emissions caused by fossil-fuel vehicles. EVs require expensive batteries and power electronics for charging and discharging the battery. Unfortunately, battery technology, such as lithium-ion batteries requires substantial improvements to effectively compete with fossil-fuel cars in price. Also, batteries are usually heavy, take up large space and still have range limitation. Wireless Dynamic Charging (WDC), while the vehicles are in motion, is seen as an alternative to overcome the drawbacks associated with batteries. Due to the continues charging when driving, batteries can become smaller as most of the traction energy comes from the grid directly. WDC is fundamentally developed based on inductive power transfer (IPT) technology, where a time-varying magnetic field is generated by transmitter coils, which are installed underneath the road surface, to wirelessly power receiver coils, that charge the EV's battery continuously.

Presently, there are several technical challenges associated with WDC, which hinders commercialization. The output power fluctuation along the driving direction is one of the most serious problems. These fluctuations cause reduction in constant energy transfer thus requiring larger batteries. Also, batteries lifetime is significantly reduced as a result of increasing internal heating. Several studies attempted to realise constant output power for WDC. However, proposed methods so far, have disadvantages such as high cost, complexity or unable to sustain constant output power throughout the charging process.

The work in this thesis proposes a multiphase WDC system to simultaneously achieve constant and high output power for EV applications. The proposed WDC system utilizes multiple primary windings that guarantee a homogeneous mutual magnetic flux for the receiver along the driving direction. This results in a constant induced voltage across the receiver and hence constant output power to charge the EV battery. High output power capability is attained by using multiple transmitter windings arranged in a novel winding method. The effectiveness of the proposed system is analytically described, simulated and demonstrated experimentally using a 3-kW laboratory prototype with the three-phase transmitter. The proposed system requires only simple control, eliminates communications between the primary and secondary sides and delivers 125% higher power transfer capability compared to conventional single-phase WDC systems.

DEDICATION

I dedicate this work to my family and my home country, Việt Nam.

Một chặng đường đã đi qua, tôi thầm cảm ơn những ai đã bước cùng tôi trên hành trình đó.

Acknowledgment

My first words of acknowledgements are dedicated to my advisory board for supervising this work for nearly four years. I would like to thank Van-Tung Phan for introducing me to the research topic and his vital support for helping me to earn the NSS scholarship. I would like to thank Mohamed for his patience and meticulousness especially when he helps me to check all my manuscripts. I would like to thank Volker who always has bright ideas as well as useful advice for my long-term career. I am always comfortable and enjoyable to work with my supervisors, who always give me enough freedom to carry on the research. For me, this is the luckiest thing I have ever had in my PhD journey.

I would like to thank my examiners, Prof. Paul Mitcheson from Imperial College London and Dr Nick Baker from Newcastle University, not only for serving in my committee, but also for providing me valuable advice to improve my work. This thesis becomes more complete, logical, and convincing with all their suggestions and help.

I have the deepest gratitude to Newcastle University for funding this work in the Newcastle-Singapore Research Scholarship scheme. I would like to thank Dr Thillainathan Logenthiran from the Singapore campus for helping me during the applying process. Furthermore, I would like to thank the school of engineering and Dr Glynn Atkinson for selecting me to receive the school research scholarship.

I would like to thank James and Gordon in the UG Lab, Darren in the Electronic Lab, Dr Dave Atkinson, and all technicians in the mechanical workshop for helping to implement the experimental rig. I would like to thank Nicola from the school of engineering for helping me to sort out the paperwork.

It has been also a great time to discuss the power electronics and collaborate with my colleagues all over the world. Thank you, Ali Ramezani from McMaster University, Jose and Dr Alicia from Malaga University, Nam from Vrije University Brussel, Thuan from University of Texas at Dallas and especially Dr Tuan Doan from Soongsil University.

In Merz Court, I have a chance to know many intelligent and lovely people with whom I have had a great time of joyfulness. They are Bassey, Petros, George, Yara, Najib, Lee, Nasiru, Joe, Mansoureh, Bethany, Polycarp, Jacob, Luke, Nicola, Raihan, Haimeng, Cuili, Mohammed,

TABLE OF CONTENTS

LIST OF FIGURES

LIST OF Tables

LIST OF Abbreviations

AC charging   Alternative Current charging

BP   Bipolar pad

CC charging   Constant Current charging

CV charging   Constant Voltage charging

CPT   Capacitive Power Transfer

DC charging   Direct Current charging

DD   Double D pad

DDQ   Double DQ pad

DSP   Digital Signal Processor

EVs   Electric Vehicles

EMI   Electromagnetic Interference

ESR   Equivalent Series Resistance

FEA   Finite Element Analysis

IPT   Inductive Power Transfer

ICNIRP   International Commission on Non-Ionizing Radiation Protection

LiC	Lithium-Capacitor
LCL	Inductor–Capacitor–Inductor
LCC	Inductor–Capacitor– Capacitor
MOSFET	Metal–Oxide–Semiconductor Field-Effect Transistor
PS	Parallel-Series
PP	Parallel-Parallel
PFC	Power Factor Correction
PFM	Pulse Frequency Modulation
PWM	Pulse Width Modulation
PHEVs	Plug-in hybrid EVs
RMS	Root Mean Square
SS	Series-Series
SP	Series-Parallel
SoC	State of Charge
SiC MOSFETs	Silicon Carbide MOSFETs
V2G	Vehicle-to-grid
WPT	Wireless Power Transfer

WC	Wireless Charger
WDC	Wireless Dynamic Charging
ZVS	Zero Voltage Switching
ZCS	Zero Current Switching
ZPA	Zero Phase Angle

LIST OF SYMBOLS

A_r — Area of receiver's ferrite core

B — Maximum magnetic flux density

C_{ia} — Primary parallel capacitor of phase i

C_{ib} — Primary series capacitor of phase i

C_{com1} — Compensation capacitor on L_1

C_{com2} — Compensation capacitor on L_2

C_{com3} — Compensation capacitor on L_3

C_f — Fixed cost part of WDC system

C_v — Variable cost part of WDC system

d_p — Distance between two adjacent cores

D — Duty cycle of PWM signal

f — Switching frequency

I_{bat} — DC charging current of output battery

I_{SC} — Secondary short-circuit current

I_{in}	Input current of the WPT system
I_i	Current through the transmitter i
I_o	Amplitude of I_i
k_{is}	Coupling factor between transmitter i and receiver
L_i	Transmitter coil i
L_s	Receiver coil
l_o	Length of two adjacent core poles
L_{ia}	Primary resonant inductor of phase i
L_{1s}	Secondary resonant inductor
M_{is}	Mutual inductance between transmitter i and receiver
M_o	Maximum value of M_{is}
M_{23}	Crossing mutual inductance between L_2 and L_3
n	Number of transmitters
	Number of phases
	Number of Inverter's legs
N_1	Number of turns for L_1
N_2	Number of turns for L_2
N_3	Number of turns for L_3

P_o	Output power of the WDC system
PS	Phase shift angle
Q_2	Secondary loaded quality factor
R_o	Equivalent impedance of output battery
S_{ia}	Gate signal for the upper switch of leg i
S_{ib}	Gate signal for the lower switch of leg i
T	Period of PWM signal
V_{DC}	DC Voltage
V_{in}	DC input voltage of the WPT system
V_s	Receiver induced voltage
$V_{i(i+1)}$	Inverter output voltage between leg i and leg $i+1$
V_{bat}	DC charging voltage of output battery
V_{T1}	Induced voltage on L_1 caused by the crossing mutual inductances from other transmitters
V_{T2}	Induced voltage on L_2 caused by the crossing mutual inductances from other transmitters
V_{T3}	Induced voltage on L_3 caused by the crossing mutual inductances from other transmitters

W_p	Width of the transmitter's ferrite core
x	Displacement of the receiver along the driving direction
ω	Angular frequency

CHAPTER 1
Introduction

1.1 Background

Wireless Power Transfer (WPT) is a method of transferring power wirelessly without any physical contact. In the context of this thesis, the term "Wireless Power Transfer" refers to near field transmission and the work presented here is also near field transmission. A near field WPT system can be classified as either Inductive Power Transfer (IPT) or Capacitive Power Transfer (CPT). The IPT system adopts a magnetic field to collect power from the primary side (i.e. source side) to the secondary side (i.e. load side). In contrast, a CPT system uses an electric field. The principle is similar to the operation of a conventional conductive transformer; however, the IPT system normally operates with a large air-gap. For this reason, an IPT system can be described as "loosely coupled" as opposed to a "tightly coupled transformer". A wireless coupler including transmitter and receiver is normally adopted in an IPT system. For a better understanding, Fig. 1.1 (a) and (b) illustrate diagrams of a conventional transformer and a wireless coupler, respectively. In a conventional transformer, there is a very small air-gap between the primary and secondary sides, therefore, the coupling factor between two windings of two sides is close to 1. In contrast, there is always a large distance between primary and secondary sides in the IPT system, therefore, the coupling factor is always significantly lower than 1.

(a)   (b)
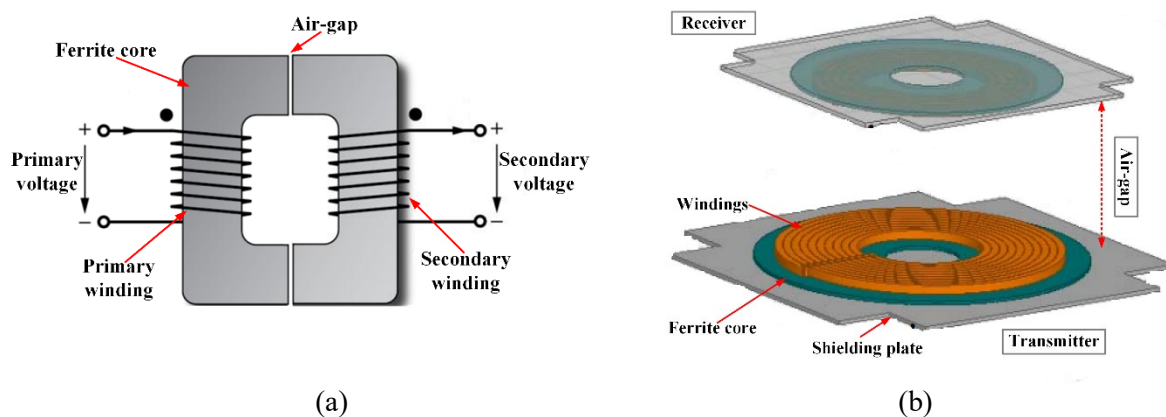
Fig. 1.1. Diagrams of (a) the conventional transformer and (b) the wireless coupler.

Compared to the conventional conductive power transfer, WPT has several benefits, such as greater convenience for users. Therefore, the concept of the WPT system was discovered a long time ago. One of the most famous pioneers, Nikola Tesla, demonstrated the first WPT experiment at Columbia University, New York, in 1891, as illustrated in Fig. 1.2 (a) and (b). In his publication after the demonstration [1-2], Tesla described the principle of WPT: "*a resonant circuit including the wireless coil combining with a capacitor to operate at the high frequency in both sides of the circuit is prerequisite condition for transferring power wirelessly*".
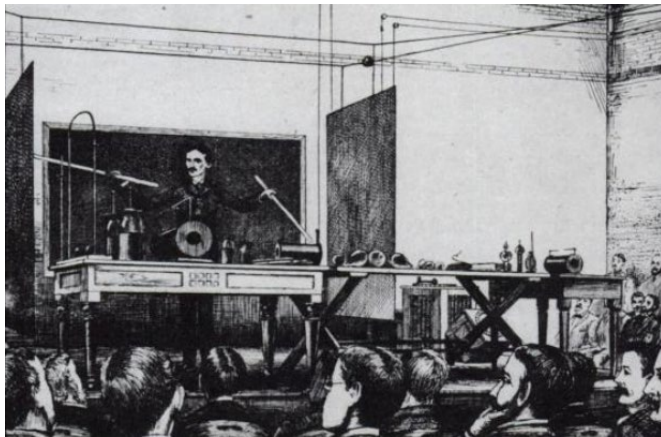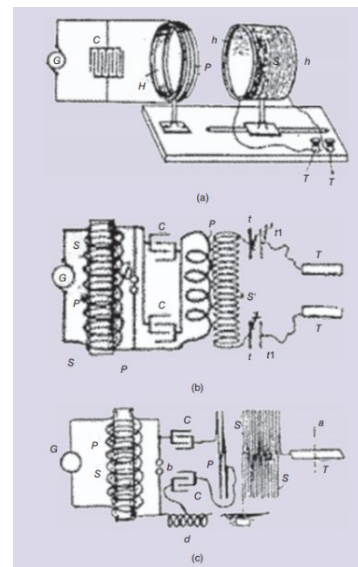
(a)   (b)

Fig. 1.2. (a) Tesla's demonstration in 1891. (b) Three methods to operate a WPT system [1].

For many decades after Tesla's demonstration, the WPT technology sank into oblivion because of several technical issues. Firstly, it is not easy to operate the WPT system at the high frequency as the switching device technology has not been developed enough yet. It leads to a bulky wireless coil and capacitor as the whole WPT system operates at a low frequency. Secondly, the low-energy conversion efficiency in a WPT was a big issue as the losses occur in two wireless coils. The main reason is that the Litz wires (i.e. copper wires with low AC resistance) were difficult to manufacture at that time, therefore a single copper wire was used, which increases the losses and reduces the total efficiency. Thirdly, battery-powered devices such as electric vehicles or mobile phones gained very little popularity at that time, therefore there is no room for WPT technology. However, the above challenges and difficulties have recently been removed with the advancements in switching devices and the introduction of high-frequency and high-power-rating semiconductor devices. Furthermore, the use of battery-

powered devices has increased significantly in recent years and the wireless charging technology has become increasingly popular with its benefits of more convenience and offering more frequent charging.

1.2 Application of WPT systems

The inherent nature of a WPT system allows the technology to offer more benefits than conventional conductive power transfer. Due to electrical isolation, WPT removes any physical contact and set users free from the annoying cables. The charging cables are removed from the WPT system, which helps to reduce any potential tripping hazards. A WPT system is normally resistant to surrounding environmental conditions such as wind, rain, ice or snow, etc. For battery-charging applications, the battery volume and weight can be reduced by up to 20% compared to conventional conductive charging, as more frequent charges are offered by a WPT system [3].
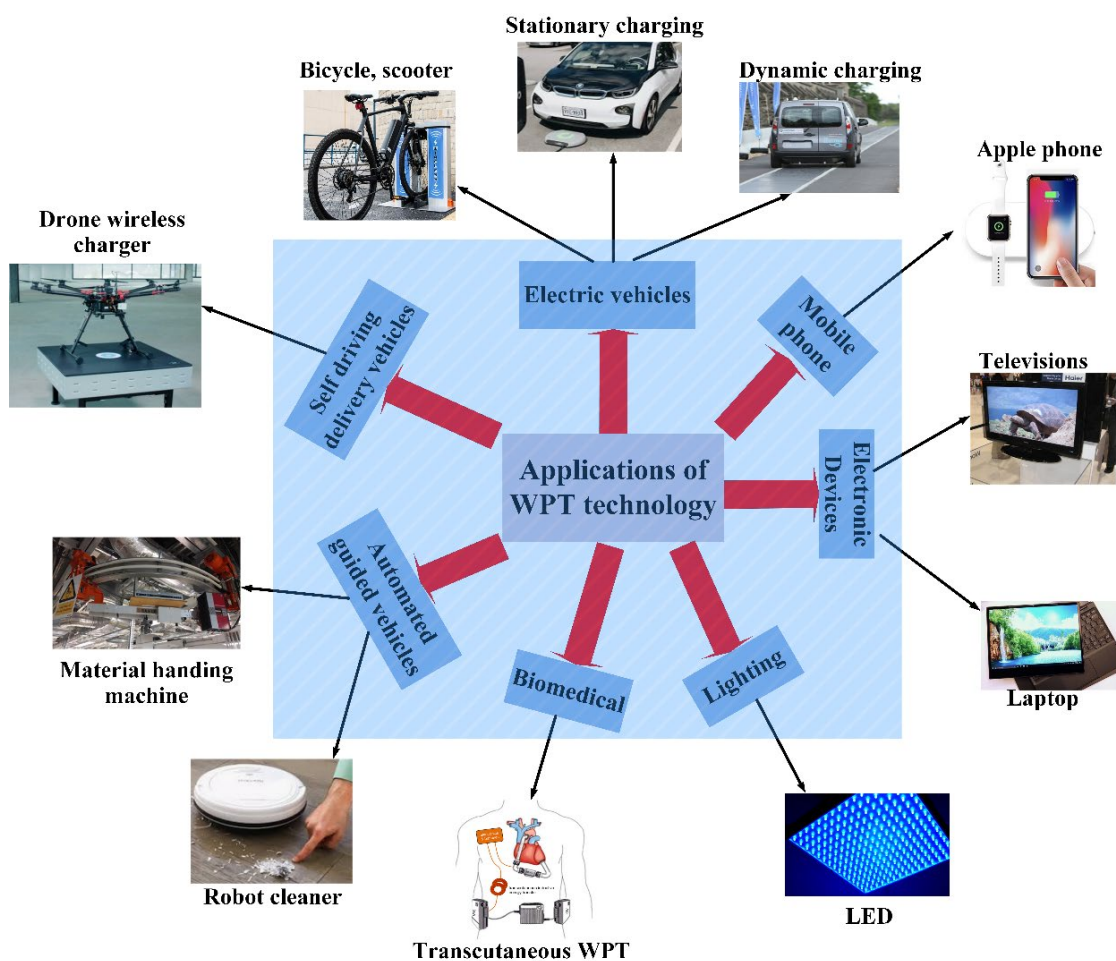
Fig. 1.3. Illustration of various applications of the WPT technology.

There are numerous applications based on WPT technology such as: bio-medical devices, automated guided vehicles, electronic battery-charging devices, electric vehicles, etc. Fig. 1.3 illustrates some WPT applications. Depending on the power level, the WPT applications can be divided as follows:

- Low power applications: biomedical, lighting, electronic devices, and mobile phones where the power level is normally lower than 100 W.
- High-power applications: electric vehicles including automated guided vehicles. The power ranges from several hundred watts for a robot cleaner and up to several hundred kilowatts for dynamic charging of an electric bus, for example.

The shape and dimension of the wireless couplers also vary according to different applications and where the installation spaces are situated. Fig. 1.4 depicts several receivers' coil topologies for various applications. The installation area of the coil can vary from mm^2 range in biomedical application to m^2 in electric vehicle charging system. The following content from Section 1.2.1 to 1.2.3 summarizes the research and development of WPT in various applications such as electronic devices and biomedical applications.

(a)   (b)   (c)
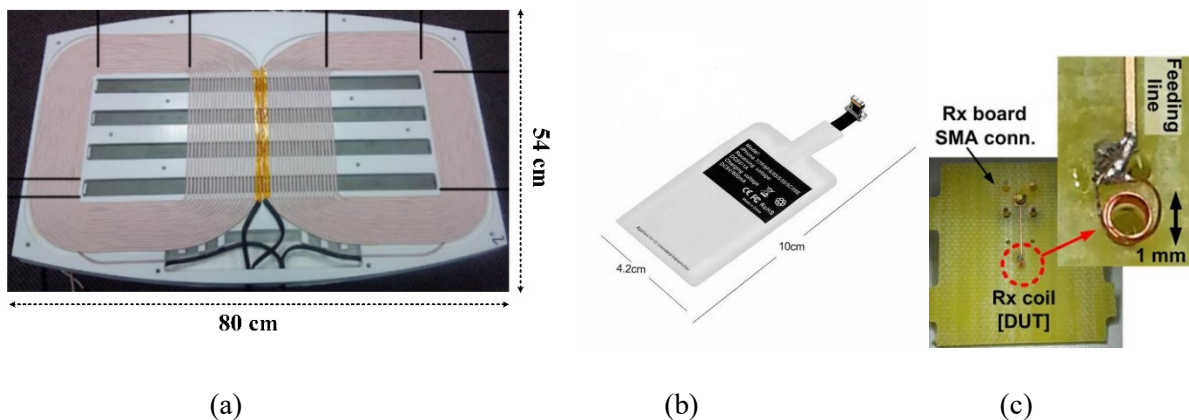
Fig. 1.4. Illustration of various receiver coil topologies for different applications. (a) Stationary electric vehicle [4]. (b) QI wireless charger receiver for Apple iPhone [5]. (c) Millimetre-sized biomedical implants for biomedical use [6].

1.2.1 Electronic devices

Wireless charging technology offers many advantages for electronic devices over the conventional conductive charging. Wire removal is the greatest benefit of the WPT system for electronic devices' battery charging, especially portable devices. For that reason, wireless charger commercial products have been released by many companies in the world including

the biggest names such as Samsung or Apple, Asus, Google, HTC, Huawei, LG Electronics, Motorola Mobility, Nokia, Samsung, BlackBerry, Xiaomi, and Sony.

Nowadays, there are two standards governing wireless charging for portable electronics devices, released by Wireless Power Consortium (i.e. QI standard) in 2008 and Air Fuel Alliance in 2015. The major difference between these two standards is the operating frequencies for the power transmission band and communication band. While the Wireless Power Consortium utilizes the same frequency band for both purposes, the standard from Air Fuel Alliance uses different bands. Moreover, the Air Fuel Alliance also supports multiple output chargers in several products with respect to different power requirements by using one single power source on the primary side. Board member companies adopted Air Fuel Alliance including Broadcom, Gill Electronics, Integrated Device Technology (IDT), Intel, Qualcomm, Samsung Electronics, Samsung Electro-Mechanics, and WiTricity. Oppositely, Apple, Asus, Google, HTC, Huawei, LG Electronics, Motorola Mobility, Nokia, Samsung, BlackBerry, Xiaomi, and Sony selected the QI standard for their products.

1.2.2 Biomedical applications

The first prototype wireless charger for biomedical applications was developed in the 1960s [6-9]. The authors concluded that batteries within heart implants could be charged painlessly with IPT, avoiding any complications or potential infections. Another demonstration was carried out to examine the power transfer capability of a WPT system with 400-kHz frequency and 1-kW power across the chest wall of an anaesthetized dog. The receiver side was placed inside the chest wall while the transmitter side of the system was put outside the chest wall. The figures of transmitter and receiver prototypes are shown in Fig. 1.5 (a) and (b) respectively.

(a)   (b)
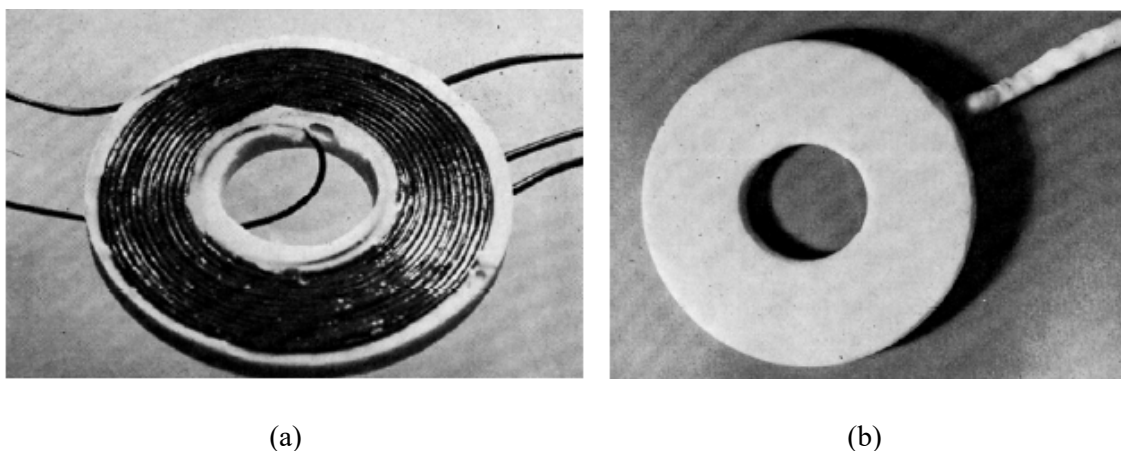
Fig. 1.5. The prototype of (a) transmitter and (b) receiver in the experiments of [7], which transferred 1-kW power across a chest wall of a dog.

Due to the advancements of semiconductor devices, a recent development allows a compact WPT system to be placed inside a living animal or a human [10-15]. The receiver size can be designed to be as small as possible while still maintaining the same power level and efficiency. The frequency range can vary from hundreds of kHz to several MHz. A recent paper by ETH Zurich [10] reported achieving an efficiency of 95 % for the transferred power of 30 W with a 20-mm air gap for implantable mechanical heart support systems (i.e. Fig. 1.6 (a)). When the operating frequency increases, the receiver size can be minimized. Georgia Tech. [11] developed a prototype implant with a receiver that had a diameter of just 1 mm and delivered a power of 224 μW at 200 MHz with a 12-mm air-gap and efficiency of 0.56 % (i.e. Fig. 1.6 (b)).

(a)   (b)
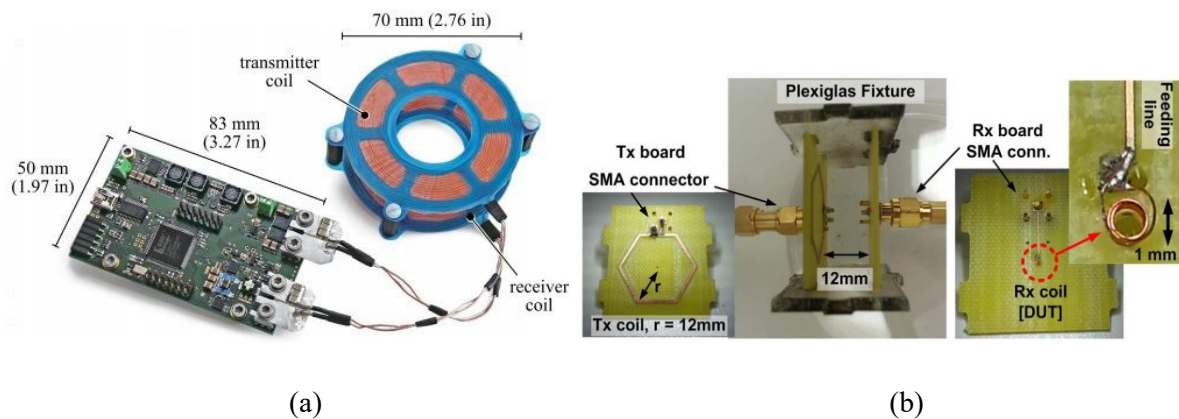
Fig. 1.6. (a) Heart implant support WPT systems [10]. (b) Millimetre-sized biomedical implants WPT system [11].

1.3 Electric vehicles wireless charging

1.3.1 Conductive charging for electric vehicles (EVs)

An Electric Vehicle (EV) adopts one or more electric motors or traction motors for propulsion. EV can be powered through a collector system by electricity from off-vehicle sources, or may be self-contained with a battery, solar panels or fuel-cell tank. Electric vehicles (EVs) can also be classified as hybrid EVs or pure battery EVs. Hybrid EVs contain an electric motor as well as a traditional internal combustion engine (ICE) while a pure battery EV contains only the electric motor. The battery pack in the hybrid EVs is much smaller than that in the pure-battery version. Compared to traditional vehicles using ICE, EVs offer several advantages such as reduction in noise and emissions, higher-efficiency conversion, and the possibility of using regenerative braking.

Presently, plug-in charging is the most common method of charging hybrid and pure-battery EVs. Plug-in charger methods can be categorized as off-board and on-board types with unidirectional or bidirectional power flow [16]. Unidirectional charging allows power transfer only from the grid to the vehicle, which limits hardware requirements and simplifies the control process. On the other hand, bidirectional charging supports battery energy injection back to the power grid. An off-board charger is normally utilized for high charging power and is less constrained by size and weight. Figure 1.7 describes the on/off-board charging system and power levels for EVs [16]. The conductive charging can be classified into three different levels according to the standard SAE J1772, with levels 1 and 2 for on-board AC charging and level 3 for off-board DC charging. Figure 1.8 illustrates the Tesla DC supercharger system, which can provide up to 150 kW power, and the corresponding charging time can reduce to 20 minutes to charge up to 50% for the original 85 kWh Model S [17].
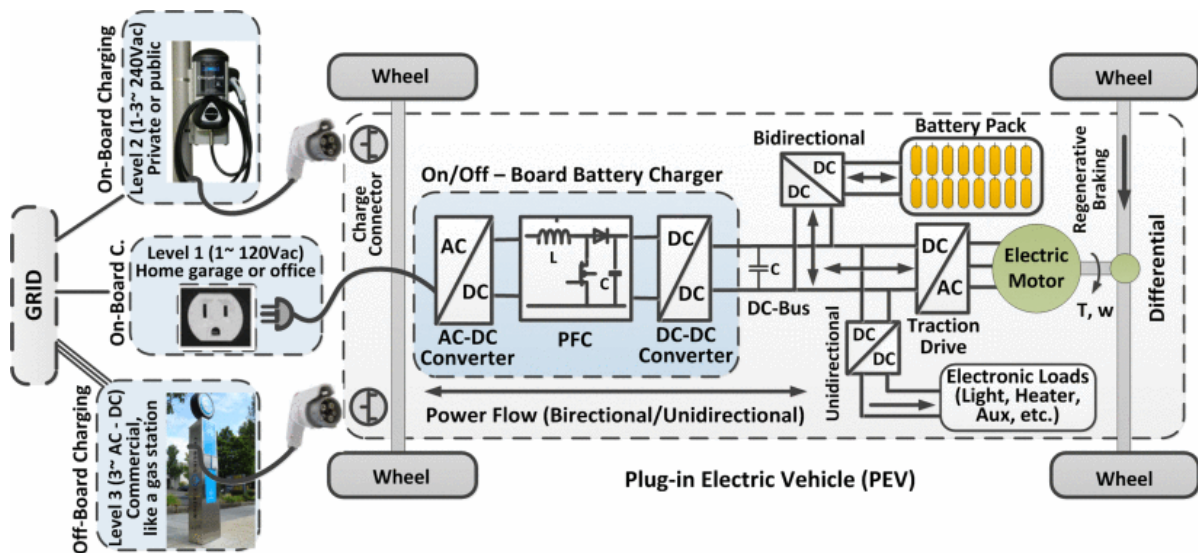
Fig. 1.7. On/off board charging systems and their power levels for EVs [16].

Fig. 1.8. Tesla supercharger systems. (a) Outlets in Europe/Worldwide (left) and North America only (right). (b) Tesla Model S charging at the supercharger station in Newark, Delaware [17].

Another EVs conductive charging method without plug is to use the overhead cable. This method is also called "conductive dynamic charging" as the vehicle is in slow motion while charging. One example is developed by Siemens for the hybrid trucks where they are connected to the overhead cable by using conductor rods [18]. The trucks are charged by a 670V DC power while moving along the electrified road segment as shown in Fig. 1.9. These systems are more suitable for heavy-duty vehicles on the motorway where more spaces for cable installation are available. In contrast, this method is not really up to the city centres environments where the space for cable installation is limited.

Fig. 1.9. Charging hybrid trucks by using overhead cable (source Siemens)

However, the high penetration of EVs is still limited at the present time due to several technological barriers, including electricity storage technology. It always requires a battery, which is unsatisfactory energy density, longer charging time and high cost. The energy density of a rechargeable battery is always much lower than that of gasoline. For example, the energy density of the commercial EV's lithium-ion battery is only 90–100 Wh/kg while the energy density for gasoline is up to about 12 000 Wh/kg [19]. Therefore, the battery packs in EVs are much larger and heavier compared to a gasoline tank to provide equivalent energy. On the other hand, the charging time of the EV's batteries would take much longer than refuelling a gasoline tank in conventional vehicles. In the current charging technology, the charging process can take tens of minutes for fast chargers and up to hours or even overnight for ac chargers, depending on the charging power level and the capacity of the batteries. Moreover, the limited range of EVs would require much more frequent charging along the journey, which causes inconvenience for drivers.

1.3.2 Wireless charging of EVs

Wireless charging is one of the potential solutions to mitigate the EV's issues, which helps to overcome the limitation of the current battery technology. WPT charging for EVs can be classified as stationary or dynamic charging based on the movement status of the vehicle. If the vehicle is wirelessly charged while not moving, then WPT stationary charging is used. Examples include charging of vehicles when waiting at traffic lights or not in use, such as at home or in public car parks. If the relevant vehicle's position changes regarding the transmitter, then dynamic charging is utilized. Most of the prototype and commercial WPT systems for EVs are stationary chargers at the moment. The power levels can vary from several kW to hundreds of kW depending on the vehicle types. Figure 1.10 (a) and (b) illustrates two stationary EVs wireless chargers developed by Fraunhofer Institute for Integrated Systems and Device Technology and WiTricity, respectively.

| (a) | (b) |
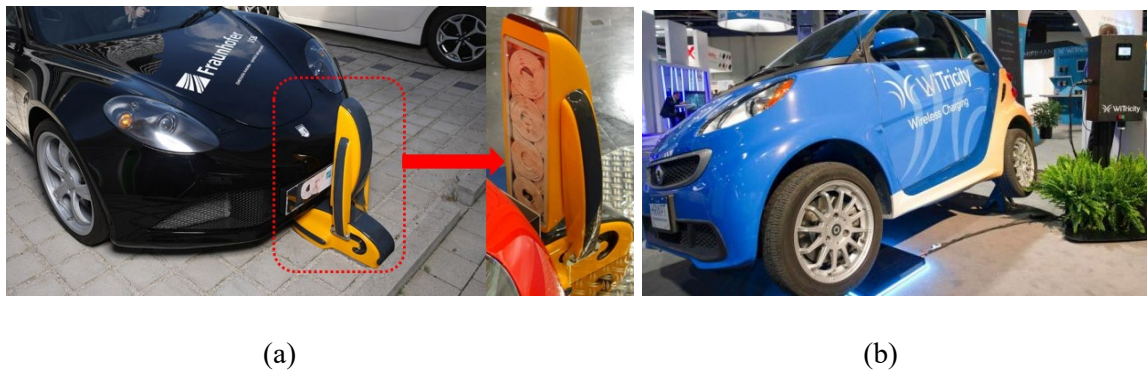
Fig. 1.10. Photos of stationary EV wireless charger. (a) Fraunhofer Institute for Integrated Systems and Device Technology (Germany). (b) Witricity (US).

Figure 1.11 shows several dynamic EV charging prototypes in South Korea and Germany. Table 1.1 provides information on the recent ongoing and finished projects of WPT charging for EVs, in both academia and industry.

(a)

(b)

Fig. 1.11. Photos of dynamic EV wireless charger systems. (a) KAIST (Korea): the bus prototype and wireless coupler structure. (b) INTIS – Integrated Infrastructure Solutions (Germany).

TABLE 1.1

SUMMARY OF SEVERAL PROJECTS OF EV WIRELESS CHARGING SYSTEMS

Project	Types	Applications	Power levels	Operating Frequencies	Air-gap/ Efficiency	Year
Fraunhofer (Germany) [20]	Stationary charging	Car	3.6 kW	<150 kHz	20 cm/ 95 %	2015
INITS (Germany) [21]	Dynamic charging	Car and Auto-tram	30 kW	35 kHz	10 cm	2016
Oak Ridge Laboratory (US) [22]	Dynamic charging	Car	20 kW	22 kHz	95%	2013-present
KAIST (Korea) [23]	Dynamic charging	Bus	100 kW	20 kHz	20 cm/ 80%	2009-present
Korea Railroad Research Institute (Korea) [24]	Dynamic charging	Train	1 MW	60 kHz	5 cm/ 82.7%	2014-2015
University of Auckland (New Zealand) [25]	Stationary and Dynamic Charging	Multiple vehicle types	6 kW	Vary	Vary	1989-present
Bombardier PRIMOVE (Germany) [26]	Stationary charging	Bus	200 kW	Not reported	>90 %	2013
BWM/Audi/ Mercedes (Germany) [27]	Stationary charging	Car	7.2 kW	85 kHz	>90%	2015-present
CONDUCTIX WAMPFLER (Italy) [28]	Stationary and Dynamic Charging	Bus	200 kW	20 kHz	95%/ 4 cm	2010
Hertogenbosh (Netherlands) [29]	Stationary and Dynamic Charging	Bus	120 kW	Not reported	Not reported	2012
Milton Keynes (UK) [30]	Stationary and Dynamic Charging	Bus	100 kW	Not reported	Not reported	2017-present
Victoria Project (Spain) [31]	Dynamic charging	Bus	50 kW	Not reported	Not reported	2013
WAVE IPT (US) [32]	Stationary charging	Bus	50 kW	20 kHz	90%	2012-present
QUALCOMM (US) [33]	Stationary and Dynamic charging	Car	20 kW	85 kHz	Not reported	2016-2019
Witricity (US) [34]	Stationary charging	Car	11 kW	85 kHz	94%	2008-present
Nissan (Japan) [35]	Stationary charging	Car	11 kW	85 kHz	Not reported	2011
TOSHIBA (Japan) [36]	Stationary charging	Car	7 kW	Not reported	Not reported	2013

1.4 Aims and objectives

Based on the considerations given above and due to the fact that there are still many issues regarding the development of the Wireless Dynamic Charging (WDC) system, the aim of this thesis is to answer questions regarding the analysis, design and implementation of the multiphase WDC system to achieve low output power pulsation, high power transfer capability, low stray fields and minimizing the implementation cost. To achieve that aim, the main objectives of the thesis are listed as follows:

- To investigate the requirements and issues associated with Wireless Dynamic Charging (WDC) for Electric Vehicles (EVs).

- To conduct a comprehensive study that satisfies the requirements of WDC for EVs applications.

- To develop a novel multiphase WDC system that can achieve constant output power while the vehicle is in motion along the driving direction. Usually, with the single-phase WDC system, high pulsation of output power occurs. Therefore, the objectives of this research focus on utilizing multiple transmitter windings that guarantee a homogeneous mutual magnetic flux for the receiver along the driving direction. This results in a constant induced voltage across the receiver and hence constant output power to charge the EV battery.

- To investigate the relationship between efficiency and associated cost in a multiphase WDC system.

- To develop a scaled-down experimental set-up system that confirms the effectiveness of the proposed multiphase WDC system.

1.5 Thesis contribution and publications

Electric vehicles (EVs) have recently received a great deal of attention because of their clean, efficient and environment-friendly features. However, the high penetration of EVs is still limited at the present time due to many technological barriers, including battery capacity. An expensive and large battery with a long charging time is normally equipped to achieve a satisfactory EV driving range. Wireless Dynamic Charging (WDC) has been proposed to overcome the limitation of current battery technology, which has been reported in [23], [25] based on inductive power transfer (IPT) technology. WDC enables EVs to be charged

wirelessly while in motion. As a result, the battery size of EVs can be greatly reduced and the driving range limitation can be completely alleviated.

Presently, there are several technical challenges which slow down the commercialization of the WDC system. Among them, the output power variation along the driving direction is one of the most serious problems. When the receiver is in motion along with the transmitter, then the coupling factor varies, which results in a variation of output power. Therefore, a number of studies attempted to realise constant output power. However, these methods have several disadvantages, such as high cost, complexity or not achieving thoroughly the constant output power. Besides output power pulsation issues, the transferred power of the conventional WDC system is also limited by the rating of the semiconductor devices, transmitter coil, and compensation circuit. In real applications, several EVs may need to be charged simultaneously; thus, the high-power demand becomes a necessity. Moreover, the power level required for public transport such as electric bus or train systems may go up to hundreds of kilowatts or even megawatts [24]. In these applications, the conventional single-phase dynamic charging system may not be able to produce such a requirement. Therefore, multiphase systems are seen as a solution to transferring higher output power [37-38].

The work in this thesis achieves for the first time constant and high output power through the utilization of a multiphase transmitter system for the EVs wireless dynamic charging. The following are the main benefits of the proposed multiphase WDC system:

(1) Achieving constant output power with a simple control requirement.
(2) Minimize the number of inverters compared to WDC systems achieving the same constant output power.
(3) Elimination of the measurement and wireless communication (between grid and vehicle sides) regarding mutual inductance and load impedance information while the EV is in motion.
(4) Attainting higher output power (i.e. 2.25 higher for the three-phase case) for the same system parameters, e.g. mutual inductance, transmitter's current, switching frequency and receiver's dimension.
(5) Unlike previous WDC systems, the proposed approach can be easily extended to multiple EVs charging without any changes to the primary side control. This will be more suitable for real scenarios.

Significant parts of the work presented in this thesis have been published in several journals and conferences as follows:

Journal papers:

[J1] **Van-Binh Vu**, Van-Tung Phan, Mohamed Dahidah and Volker Pickert, "Multiple Output Inductive Charger for Electric Vehicles," IEEE Transactions on Power Electronics, vol. 34, no. 8, pp. 7350-7368, Aug. 2019 [39].

[J2] **Van-Binh Vu**, Mohamed Dahidah, Volker Pickert and Van-Tung Phan, "A Multiphase Wireless Dynamic Charging System with low Output Power Pulsation for Electric Vehicles", IEEE Journal of Emerging and Selected Topics in Power Electronics, vol. 8, no. 4, pp. 3592-3608, Dec. 2020 [40].

[J3] **Van-Binh Vu**, Mohamed Dahidah, Volker Pickert and Van-Tung Phan, "An improved LCL-L Compensation Topology for Capacitive Power Transfer in Electric Vehicle Charging", IEEE Access, vol. 8, pp. 27757-27768, Feb. 2020 [41].

[J4] **Van-Binh Vu**, Jose Manuel Gonzalez, Volker Pickert, Mohamed Dahidah and Alicia Triviño "A hybrid charger of conductive and inductive modes for Electric Vehicles", IEEE Transactions on Industrial Electronics (early access) [42].

[J5] **Van-Binh Vu**, Mohamed Dahidah and Volker Pickert, "Efficiency-cost parametric-analysis of a three-phase Wireless Dynamic Charging System for Electric Vehicles", (manuscript preparation).

[J6] **Van-Binh Vu**, Ali Ramezani, Mohamed Dahidah, Volker Pickert and Mehdi Narimani "Operation of High-Power Inductive Power Transfer Systems in Misalignment Conditions: A Review", (manuscript preparation).

Conference papers:

[C1] **Van-Binh Vu**, Mohamed Dahidah, Volker Pickert and Van-Tung Phan "A Multi-output Capacitive Charger for Electric Vehicle" in the 26th IEEE International Symposium on Industrial Electronics (ISIE 2017), Edinburgh, UK, Jun. 2017 [43].

[C2] **Van-Binh Vu**, Mohamed Dahidah, Volker Pickert and Van-Tung Phan "A Concept of Multiphase Dynamic Charging System with Constant Output Power for Electric Vehicles" in IEEE PELS Workshop on Emerging Technologies: Wireless Power (WoW), London, UK, Jun. 2019 [44].

[C3] **Van-Binh Vu**, Mohamed Dahidah, Volker Pickert and Van-Tung Phan " Comparison of Single and Three phase Dynamic Charging Systems for Electric Vehicles" in IEEE PELS Workshop on Emerging Technologies: Wireless Power (WoW), London, UK, Jun. 2019 [45].

1.6 Thesis layout

The thesis consists of seven chapters as follows:

Chapter 2 presents the literature review of stationary and dynamic charging systems for EVs utilizing WPT technology in terms of principles, structure, and main challenges. Greater emphasis is given to up-to-date attempts to address the main challenges of this technology, such as reduction of output power and efficiency under misalignment, higher implementation cost, and safety concerns regarding pedestrians' exposure to the electromagnetic field.

Chapter 3 provides details of the concept of the proposed multiphase system for EV dynamic charging. It describes the circuit configuration, structure of primary windings layout and transmitter's current conditions for achieving a constant output power while the EV is in motion along the driving direction.

Chapter 4 presents an illustrative design example with the three-phase WDC system. The optimized design for the three-phase transmitter and receiver is conducted in FEA software to achieve the highest coupling factor by using minimum ferrite material. The crossing mutual inductances between the different phases of the transmitter are compensated by adding small capacitors in series with each transmitter winding.

In Chapter 5, an efficiency-cost parametric analysis is illustrated for the three-phase WDC system. It is indicated that the efficiency and cost are in a trade-off relationship. By varying the transmitter's width and receiver's ferrite area, different performances of efficiency and cost are achieved.

Chapter 6 provides the experiment results. A 3-kW prototype is built and tested to demonstrate the validity of the proposed method and to evaluate the performance of the proposed WDC system.

Chapter 7 demonstrates the benefits of the proposed multiphase WDC system by carrying out a comparison with other similar WDC systems that have similar advantages of low stray fields and a narrow transmitter width.

Finally, Chapter 8 concludes the work, summarises the main contributions of the study and gives several possible suggestions for future works.

1.7 References

[1] N. Tesla, "High frequency oscillators for electro-therapeutic and other purposes," The Electrical Engineer, vol. 26, no. 544, pp. 346–348, Oct. 6, 1898.

[2] https://www.alliedmarketresearch.com/wireless-charging-market

[3] S. Jeong, Y. J. Jang, and D. Kum, "Economic analysis of the dynamic charging electric vehicle," IEEE Transactions on Power Electronics, vol. 30, no. 11, pp. 6368–6377, Nov. 2015.

[4] M. Budhia, J. T. Boys, G. A. Covic, and H. Chang-Yu, "Development of a single-sided flux magnetic coupler for electric vehicle IPT charging systems," IEEE Transactions on Industrial Electronics, vol. 60, no. 1, pp. 318–328, Jan. 2013.

[5] https://www.apple.com/uk/shop/product/HL812B/A/mophie-wireless-charging-base

[6] J. C. Schuder, H. E. Stephenson, and J. F. Townsend, "High-level electromagnetic energy transfer through a closed chest wall," IRE Intl. Conv. Rec, vol. 9, pp. 119{126, 1961.

[7] J. C. Schuder, "Powering an arterial heart: Birth of the inductively coupled radio frequency system in 1960," Artif. Organs, vol. 26, no. 11, pp. 909-915, 1960.

[8] J. C. Schuder, H. E. Stephenson, and J. F. Townsend, "Energy transfer into a closed chest by means of stationary coupling coils and a portable high-power oscillator," ASAIO Trans., vol. 7, pp. 327-331, 1961.

[9] J. C. Schuder, J. H. Gold, and H. E. Stephenson, "An inductively coupled RF system for the transmission of 1 kW of power through the skin," IEEE Transactions on Biomedical Engineering, vol. BME-18, no. 4, pp. 265-273, July, 1971.

[10] O. Knecht, R. Bosshard, J. W. Kolar, "High efficiency transcutaneous energy transfer for implantable mechanical heart support systems", IEEE Transactions on Power Electronics, vol. 30, no. 11, pp. 6221-6236, Nov. 2015.

[11] D. Ahn and M. Ghovanloo, "Optimal design of wireless power transmission links for millimeter-sized biomedical implants," IEEE Transactions on Biomedical Circuits and Systems, vol. 10, no. 1, pp. 125–137, Feb. 2016.

[12] A. Ma and A. S. Y. Poon, "Midfield wireless power transfer for bioelectronics," IEEE Circuits and Systems Magazine, vol. 15, no. 2, pp. 54-60, Second quarter, 2015.

[13] A. K. RamRakhyani, S. Mirabbasi and M. Chiao, "Design and Optimization of Resonance-Based Efficient Wireless Power Delivery Systems for Biomedical Implants," in IEEE Transactions on Biomedical Circuits and Systems, vol. 5, no. 1, pp. 48-63, Feb. 2011.

[14] Q. Xu, Z. Gao, H.Wang, J. He, Z. H. Mao, and M. Sun, "Batteries not included: A mat-based wireless power transfer system for implantable medical devices as a moving target," IEEE Microwave Magazine, vol. 14, no. 2, pp. 63-72, March 2013.

[15] U. M. Jow and M. Ghovanloo, "Design and optimization of printed spiral coils for efficient transcutaneous inductive power transmission," IEEE Transactions on Biomedical Circuits and Systems, vol. 1, no. 3, pp. 193-202, Sept 2007.

[16] M. Yilmaz and P. T. Krein, "Review of battery charger topologies, charging power levels, and infrastructure for plug-in electric and hybrid vehicles," IEEE Transactions on Power Electronics, vol. 28, no. 5, pp. 2151–2169, May 2013.

[17] Available online at: https://www.tesla.com/en_GB/supercharger

[18] Available online at
https://www.mobility.siemens.com/global/en/portfolio/road/ehighway.html

[19] S. Li and C. Mi, "Wireless power transfer for electric vehicle applications," IEEE Journal of Emerging and Selected Topics in Power Electronics, vol. 3, no. 1, pp. 4–17, Mar. 2015.

[20] Available at: https://www.fraunhofer.de/en/press/research-news/2015/august/Wireless-charging-and-discharging-for-electric-vehicles.html

[21] Available online at: http://www.intis.de/intis/mobility.html

[22] J. M. Miller, P. T. Jones, J. Li, and O. C. Onar, "ORNL experience and challenges facing dynamic wireless power charging of EV's," IEEE Circuits and Systems Magazine, vol. 15, no. 2, pp. 40–53, May 2015.

[23] S. Y. Choi, B. W. Gu, S. Y. Jeong, and C. T. Rim, "Advances in wireless power transfer systems for roadway-powered electric vehicles," IEEE Journal of Emerging and Selected Topics in Power Electronics, vol. 3, no. 1, pp. 18–36, Mar. 2015.

[24] J. H. Kim, B. S. Lee, J. H. Lee, and J. H. Baek, "Development of 1MW inductive power transfer system for a high speed train," IEEE Transactions on Industrial Electronics, vol. 62, no. 10, pp. 6242–6250, Oct. 2015.

[25] G. A. Covic and J. T. Boys, "Modern trends in inductive power transfer for transportation applications," IEEE Journal of Emerging and Selected Topics in Power Electronics, vol. 1, no. 1, pp. 28–41, Jul. 2013.

[26] Available online at: http://primove.bombardier.com/products/charging.html

[27] Available online at: https://www.autoevolution.com

[28] Available online at: http://www.conductix.com

[29] Available online at: http://www.automotiveworld.com

[30] Available online at: https://www.eltis.org/discover/news/wirelessly-charged-electric-buses-operating-milton-keynes-uk

[31] General Concepts of VICTORIA Project in Endesa Website. (2013). [Online]. Available: http://www.endesa.com/en/saladeprensa/noticias/ wireless-en-route-charging-electric-buses

[32] Available online at: http://wave-ipt.com

[33] Available online at: https://www.qualcomm.com/news/onq/2017/05/18/wireless-dynamic-ev-charging-evolution-qualcomm-halo

[34] Available online at: https://witricity.com

[35] Available: https://www.nissan-global.com/EN/TECHNOLOGY/OVERVIEW/wcs.html

[36] Available online at https://www.toshiba.co.jp/rdc/rd/fields/14_e01_e.htm

[37] Y. Li, R. Mai, L. Lu, and Z. He, "Active and reactive currents decomposition based control of angle and magnitude of current for a parallel multi-inverter IPT system," IEEE Transactions on Power Electronics, vol. 32, no. 2, pp. 1602–1614, Feb. 2017.

[38] Y. Li, R. Mai, L. Lu, T. Lin, Y. Liu and Z. He, "Analysis and Transmitter Currents Decomposition Based Control for Multiple Overlapped Transmitters Based WPT Systems

Considering Cross Couplings," IEEE Transactions on Power Electronics, vol. 33, no. 2, pp. 1829 - 1842, Feb. 2018.

[39] Van-Binh Vu, Van-Tung Phan, Mohamed Dahidah and Volker Pickert, "Multiple Output Inductive Charger for Electric Vehicles", IEEE Transactions on Power Electronics vol. 34, no. 8, pp. 7350-7368, Aug. 2019.

[40] Van-Binh Vu, Mohamed Dahidah, Volker Pickert and Van-Tung Phan, "A Multiphase Wireless Dynamic Charging System with low Output Power Pulsation for Electric Vehicles", IEEE Journal of Emerging and Selected Topics in Power Electronics, vol. 8, no. 4, pp. 3592-3608, Dec. 2020.

[41] Van-Binh Vu, Mohamed Dahidah, Volker Pickert and Van-Tung Phan, "An improved LCL-L Compensation Topology for Capacitive Power Transfer in Electric Vehicle Charging", IEEE Access, vol. 8, pp. 27757-27768, Feb. 2020.

[42] Van-Binh Vu, Jose Manuel Gonzalez, Volker Pickert, Mohamed Dahidah and Alicia Triviño "A hybrid charger of conductive and inductive modes for Electric Vehicles", IEEE Transactions on Industrial Electronics (early access), Dec. 2020.

[43] Van-Binh Vu, Mohamed Dahidah, Volker Pickert and Van-Tung Phan "A Multi-output Capacitive Charger for Electric Vehicle" in the 26th IEEE International Symposium on Industrial Electronics (ISIE 2017), Edinburgh, UK, Jun.2017.

[44] Van-Binh Vu, Mohamed Dahidah, Volker Pickert and Van-Tung Phan "A Concept of Multiphase Dynamic Charging System with Constant Output Power for Electric Vehicles" in the IEEE PELS Workshop on Emerging Technologies: Wireless Power (WoW), London, UK, Jun. 2019.

[45] Van-Binh Vu, Mohamed Dahidah, Volker Pickert and Van-Tung Phan " Comparison of Single and Three phase Dynamic Charging Systems for Electric Vehicles" in the IEEE PELS Workshop on Emerging Technologies: Wireless Power (WoW), London, UK, Jun. 2019.

CHAPTER 2
Literature review

2.1 Electric Vehicles Battery Chargers

With the more stringent regulations on emissions, global warming, and constraints on energy resources, Electric Vehicles (EVs) and plug-in hybrid EVs (PHEVs) have gained more and more attention from governments, automobile manufacturers and customers [1]. Compared to conventional vehicles, EVs and PHEVs are more environmentally friendly, less noisy, and more efficient.

Power converters powered from the utility charge the batteries in these vehicles. A general configuration of an EV battery charger is presented in Fig. 2.1. Connecting the vehicle to the electric power grid, the power flow between them can be unidirectional or bidirectional. Unidirectional charging is a straightforward way of charging the vehicle's battery because it imposes minimum hardware requirements and especially simplifies interconnection problems [2-3]. One of the main advantages of the bidirectional charging system is the ability to support vehicle-to-grid connection, which helps to support the grid with peak demand.

EV battery chargers can be classified as on-board and off-board chargers, depending on where the charger is located [2-7]. The power level of on-board chargers is typically constrained by the weight, implementation space and cost, which ranges from 1.4 kW to 19.2 kW [8-9]. To overcome these limitations, the on-board charger can be integrated with the electric drive system [9-12]. Off-board chargers must communicate with the vehicle to provide the vehicle's battery with the accurate voltage and current.

Battery chargers play an important role in the development of EVs as they directly influence the charging time and the lifespan of the battery. For these reasons, an EV battery charger must be efficient and reliable, with a high-power density and low cost. EV battery charger operation depends on different power electronics components arrangement as well as control and the associated switching strategies. In addition, charging control algorithms are equally important and are implemented through analogue controllers, microcontrollers, digital signal processors, and other specific integrated circuits [2]. The selection of hardware topologies and charging control algorithms depends heavily on the power level, budget, and efficiency requirements.

As highlighted in Chapter 1, the EV battery charger can also be classified as conductive or inductive (wireless) chargers. While the conductive charging method adopts direct contact and a cable between the EV connector and charge outlet, the inductive charging system transfers power wirelessly. Wireless charging methods are further classified as stationary and dynamic wireless charging. For a stationary wireless charging system, the vehicle is parked and charged, while for a wireless dynamic charging system, the EV could be charged while driving.
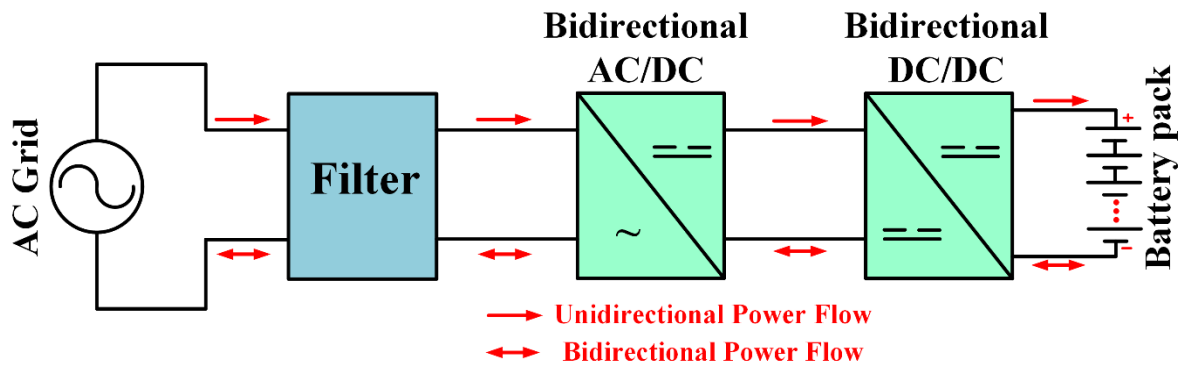
Fig. 2.1. General configuration of the battery charger for electric vehicles.

2.2 Wireless stationary charging for electric vehicles

2.2.1 The charger structure

When compared to conventional plugged-in chargers, the wireless charging method for electric vehicles (EV) has several benefits, such as greater conveniences for the users. The charging cables from the plugged-in charger on the floor may bring some unwanted tripping hazards. Moreover, users may need to handle high voltage plugs under severe weather conditions such as rain, ice, or snow which can bring the risk of an electric shock. Therefore, wireless chargers have been intensively investigated and developed by many laboratories and companies all over the world. An overall structure of the wireless charger is illustrated in Fig. 2.2 in which the system utilizes DC voltage source (i.e., V_{DC}, typically 400 V), which is normally generated using a front-end AC/DC converter with the power factor correction (PFC). On the primary side, a DC to AC converter can be used to convert the V_{DC} into a high-frequency AC voltage, feeding the primary compensation tank, which constitutes resonant inductors and capacitors. The primary compensation tank compensates the large leakage inductance of the wireless coupler. Moreover, this compensation tank can also act as a low-pass filter, which passes the fundamental-frequency signal and impedes high-frequency signals. Therefore, the

primary transmitter L_1 is supplied by a sinusoidal AC current. The output power of the wireless system is proportional with the transmitter current. To simplify the output power control procedure, the transmitter current is normally kept constant. Another compensation tank is placed at the secondary side to improve the efficiency and the power capability. This is to cancel the high leakage inductance from the coupler in the secondary side. The induced voltage at the receiver coil is rectified, and often a DC/DC converter is normally used to regulate the charging current and voltage across the battery. Unlike the conductive charger, the primary side of the wireless charger is located off-board, while the secondary side is placed on the vehicle.
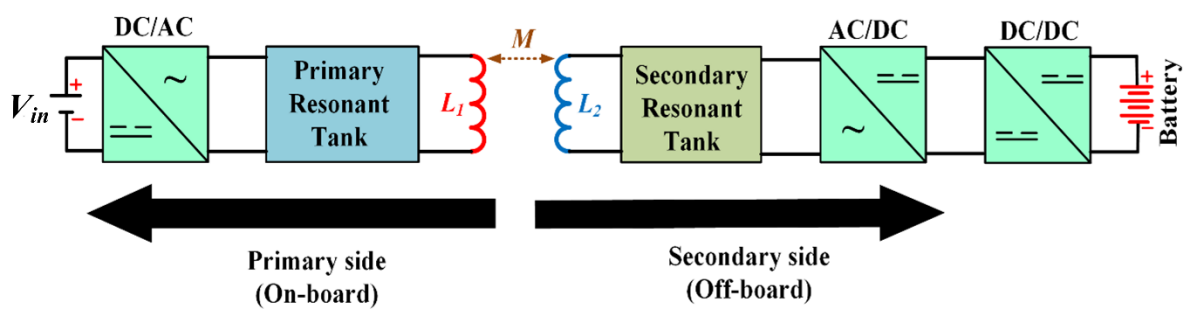
Fig. 2.2. General structure of the EV wireless charger.

2.2.2 Wireless couplers topologies

A set of loosely coupled coils instead of a conventional transformer is the major difference between a wireless charger (WC) and a conductive charger. A low coupling coefficient between the transmitter and receiver coils is one of the most serious issues in a WC system. This results in a high reactive power and reduces the power transfer efficiency. Therefore, the design and optimization of the coupler's parameters are essential to improve the coupling coefficient, extend the transfer distance, and minimize the electromagnetic field exposed to pedestrians and users/drivers. A wireless coil normally consists of copper cable, ferrite sheets, and aluminium shields as illustrated in Fig. 2.3(a) while the simplified model of a wireless coupler is shown in Fig. 2.3(b). Equation (2.1) expresses the relationship between the mutual inductance M and self-inductance of transmitter L_1 and receiver L_2. This coupling factor k indicates how strong the coupling between L_1 and L_2 is.

$$k = \frac{M}{\sqrt{L_1 L_2}} \tag{2.1}$$

(a)   (b)
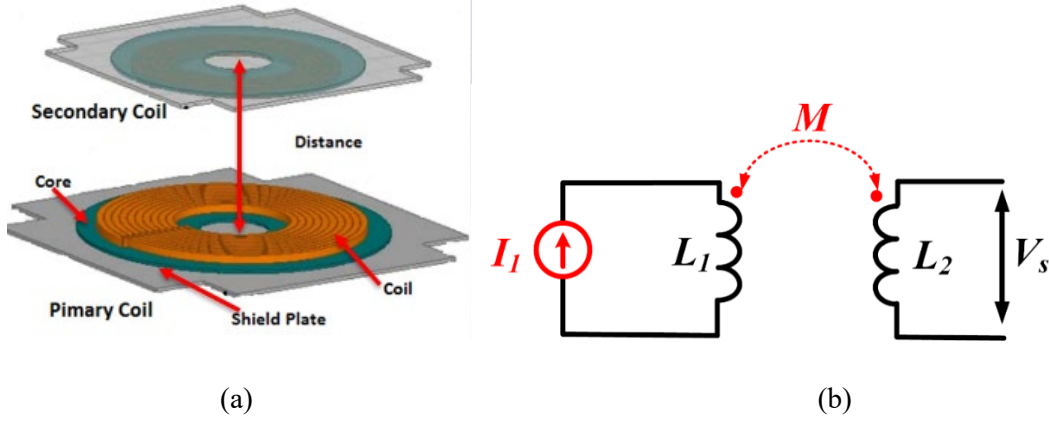
Fig. 2.3. (a) Typical structure of a wireless coupler including primary and secondary coils. (b) Simplified model of the wireless coupler.

Transmitter L_1 is normally driven by a constant current I_1, regardless of both mutual inductance and load resistance values. The transmitter current I_1 is kept constant by controlling the primary inverter or utilizing an LC circuit on the primary side. The inverter's phase shift or duty is controlled in the closed-loop controller to maintain I_1 constantly against both load and mutual inductance variations [65-66]. Another method is proposed in [18] to achieve the constant current of transmitter, which utilizes the resonance of a LC circuit at the switching frequency. The induced voltage V_s on the receiver can be expressed by:

$$V_s = j\omega M I_1 \tag{2.2}$$

where, $\omega = 2\pi f$ with f being the switching frequency of the inverter.

In the wireless power transfer system, the output power is proportional to two factors: (1) secondary uncompensated apparent power (S_U) and (2) secondary loaded quality factor (Q_2) [14].

$$P_{out} = S_U Q_2 \tag{2.3}$$

S_U is determined by the multiplication of the receiver induced voltage (V_s) and the secondary short-circuit current ($I_{SC} = \frac{V_s}{j\omega L_2}$), which is given by (2.4).

$$S_U = |V_s||I_{SC}| = \omega \frac{M^2}{L_2} I_1^2 = \omega(k^2 L_1) I_1^2 \tag{2.4}$$

From (2.3), the output power can be expressed as:

23

$$P_{out} = S_U Q_2 = \omega(k^2 L_1)I_1^2 Q_2 = \omega \frac{M^2}{L_2}I_1^2 Q_2 \qquad (2.5)$$

In (2.5) Q_2 depends on the secondary compensation circuit, which can be connected in series, parallel or with a combined connection [14]. It can be seen from (2.5) that the transferred power is influenced by the operating frequency ω, the mutual inductance M, the transmitter's current I_1 and secondary loaded quality factor Q_2. While ω and I_1 can be controlled by the primary side, and Q_2 depends on the secondary compensation circuit, M is uncontrollable within the charging process. When the relative position between the transmitter and the receiver changes, the mutual inductance M varies accordingly, resulting in a reduction of output power as well as the system's efficiency. The demonstration by the university of Auckland in [81] has shown clearly the issues of varying coupling factor where a rig including a bulb moves along the track and the bulb gets lighter and darker. Consequently, the level of stray fields increases with a potential harmfulness to the surrounding pedestrians and living animals. M can also be affected by different geometries and dimensions of the coupler pad. Therefore, the design of the wireless coupler in a wireless charger system is required for maintaining a high coupling coefficient under misalignment conditions, extending the transfer distance and minimizing the stray fields level exposed to pedestrians.

The coupling coefficient k varies significantly depending on the coil's geometries and configurations. There are two main types of wireless coupler topologies: double-sided and single-sided couplers, based on the magnetic flux distribution area [26]. Double-sided couplers generate flux paths on both sides of the coil, which results in a high stray field and a high eddy current loss in the aluminium shielding [27]. To overcome the negative effects of the double-sided coupler type, the single-sided couplers are proposed in [26], [28], and [29], where the main flux path flows through magnetic sheets installed under the winding, and the flux mainly exists in the space between the transmitter and receiver. The optimization of different coupler topologies assists with the general purposes of improving coupling coefficient, increasing misalignment tolerance, and achieving low stray fields exposed to pedestrians. Fig. 2.4 presents various single-sided coupler topologies, which are often used in the wireless stationary charger for EVs. These topologies include circular pad, rectangular pad, double D pad (DD), double DQ pad (DDQ) and bipolar pad (BP).
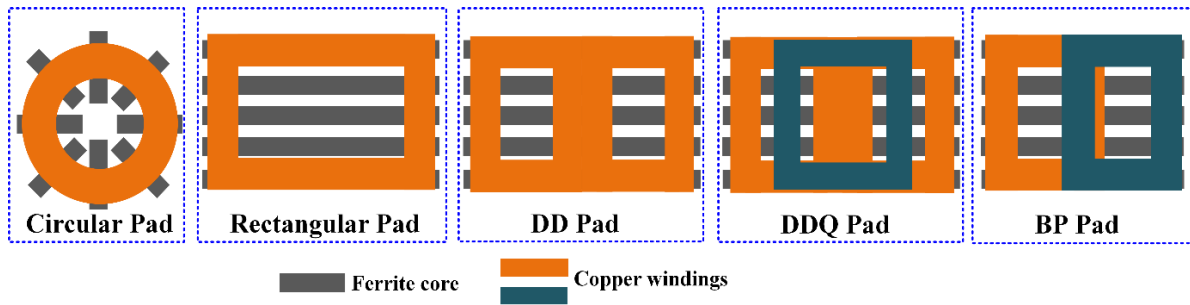
Fig. 2.4. Different wireless coupler pad topologies used in EV's wireless stationary charger.

Other ways to improve the effectiveness in the coupling coefficient and to extend the energy transfer distances are to utilize intermediate coils into the transmitter or receiver pads [30]–[33]. The principle behind this improvement is that intermediate coils and associated resonant capacitors help to boost the apparent coupling coefficient at the operating frequency while keeping the same coupling coefficient between transmitter and receiver coils. Fig. 2.5 depicts the schematic and the prototype of the four-coil WC system proposed in [33], which achieves an efficiency of 97.1% with 20 cm air-gap even without using ferrite core in the testing. However, the design guidance for this kind of system is normally more complex compared with the conventional two-coil WC system.
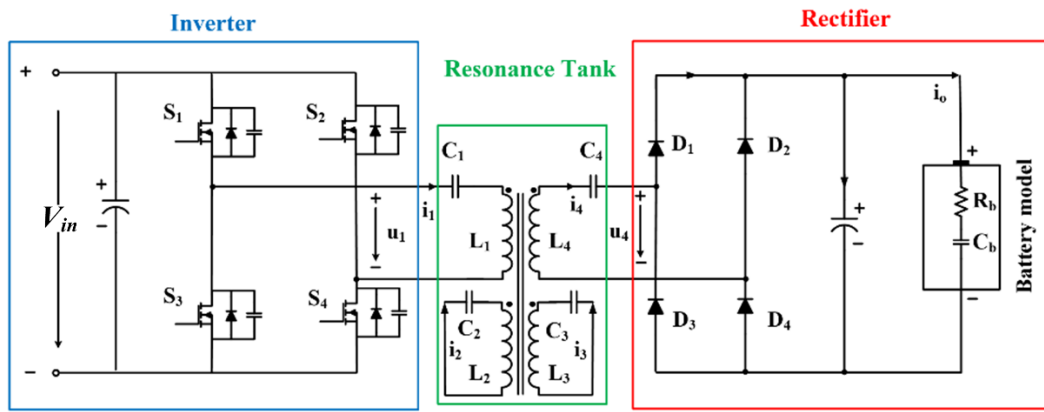
(a)
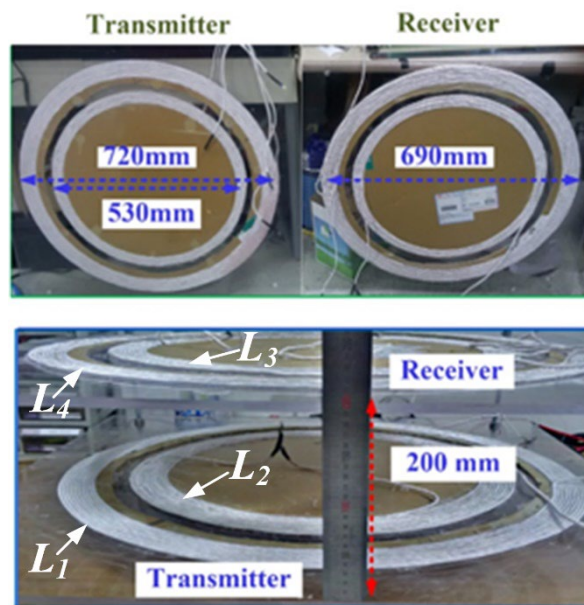
(b)

Fig. 2.5. (a) 4-coil system wireless charger [32]. (b) Prototype of the couplers.

2.2.3 Compensation circuits in wireless chargers

As mentioned in Section 2.2.2, the low coupling coefficient between the transmitter and receiver coils is always a challenge for any WC systems, which results in a higher reactive power and lower power transfer efficiency compared to the conventional conductive charger. Hence, the compensation circuit is an important part that helps to reduce the reactive power and improve the power transfer capability and overall efficiency. The principle of the compensation circuit is to cancel the high leakage inductances (resulting in high reactive powers) of the coupler coils. The compensation circuits consist of high-frequency

compensation capacitors and in some cases, inductors. Depending on how the compensation capacitors are added to the primary and secondary coils, there are four basic compensation topologies, namely series-series (SS), series-parallel (SP), parallel-series (PS), and parallel-parallel (PP) [13], [14]. In addition, there are some other topologies that have been proposed to improve the power transfer efficiency and to simplify the control of WC systems [15–19]. For instance, an inductor–capacitor–inductor (LCL) topology is introduced for the vehicle-to-grid (V2G) application in [15]. In [16], the primary compensation tank is developed by adding an LC tank between the primary side inverter and the transmitting coil. The additional LC tank helps to reduce the conduction losses of the primary switches of the inverter by reducing the primary current. Besides, the constant current (CC) control at the output can be easily achieved, using load-independent characteristics of the circuit. The unity-power-factor topology is formed in the secondary side by adding another LC circuit to the parallel compensation topology in the secondary side to minimize the circulating current in the receiver coil and to achieve a unity power factor [17]. However, on the other hand, all these topologies [15-17] require additional bulky inductors at one side or both sides, where the inductance values are normally similar to those of wireless coils. In order to reduce the size and cost of the additional inductors, the LCC-compensation topology is introduced by employing a capacitor into the LCL primary compensation tank, which is connected in series with the primary coil [18]. In [19], a double-sided LCC topology is developed in both primary and secondary sides. This topology enjoys all of the advantages of topologies presented in [15–17]. In this topology, the zero-voltage-switching (ZVS) condition for the inverter's switches can be achieved, and the resonant frequency is independent of the coupling coefficient and the load [19]. This topology has the ability to provide both the output load-independent current and voltage modes, which is an advantage for charging lithium batteries [20-21]. In order to improve the compactness of the double-sided LCC topology, the magnetic integrations of additional inductors and the wireless coupler coils are proposed and investigated in [22–24]. Several typical resonant topologies are depicted in Fig. 2.6 in which the turn ratio between the transmitter and receiver coils is assumed to be unity.
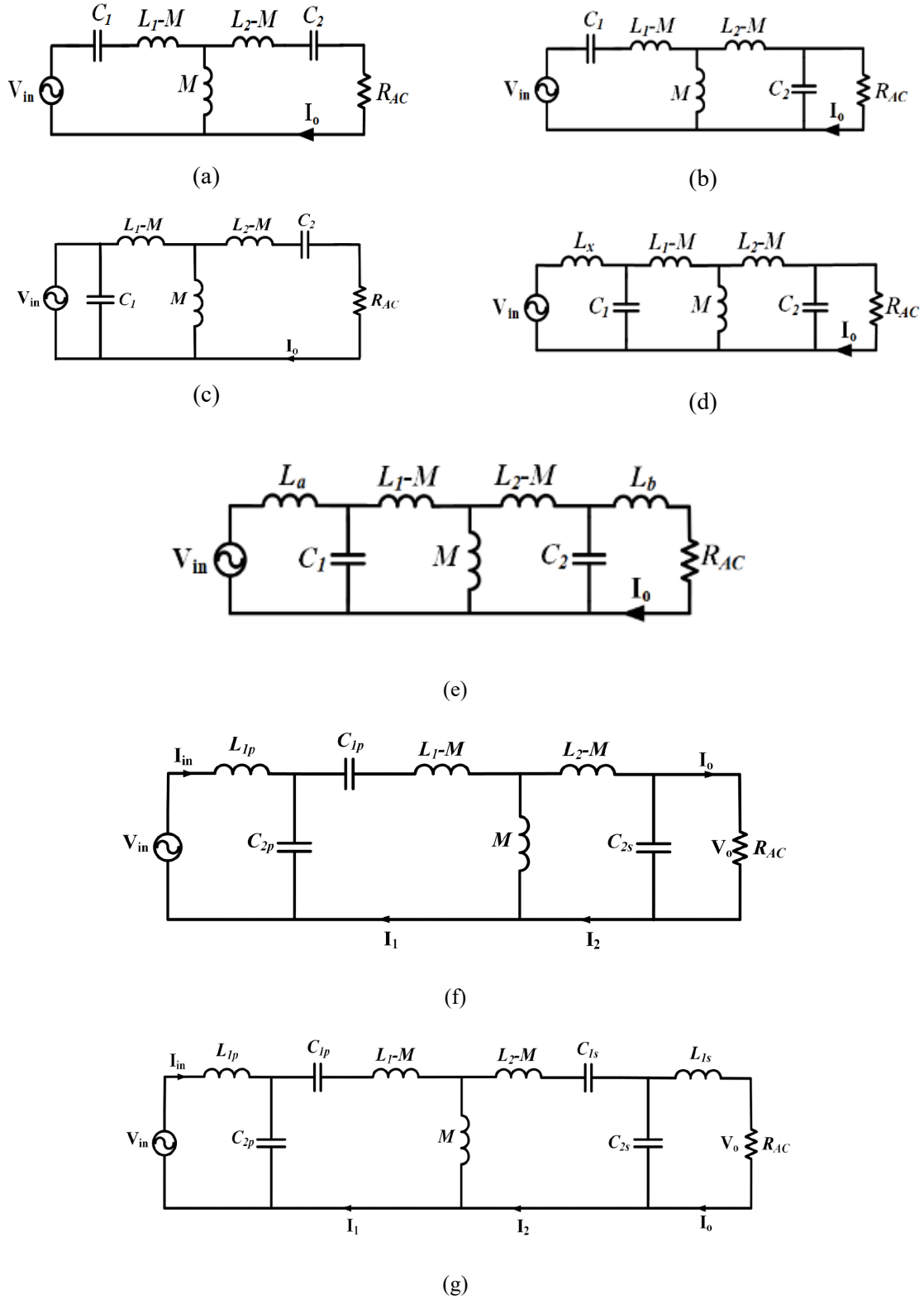
Fig. 2.6. Typical compensation circuit topologies. (a) SS. (b) SP. (c) PS. (d) PP. (e) Double-sided LCL. (f) LCC-P. (g) Double-sided LCC.

In order to compare different compensation topologies, Table 2.1 lists the main characteristics of six common output current source topologies. The same comparisons can be applied for the

output voltage source topologies as well. The first criterion mentioned in Table 2.1 is the independent resonant frequency. A wireless charger system would always prefer to operate at resonance conditions to achieve higher power transfer capability and overall efficiency. However, the resonant frequency is not always constant in some topologies consisting of SP or PP due to the variation of mutual inductance M between transmitter and receiver coils. Therefore, these two topologies are not suitable for some scenarios requiring constant operating frequency. The second criterion is the zero-phase-angle (ZPA) operation, where the inverter output current and voltage are in the same phase. This helps to minimize the reactive power in the WC system. The ZPA operation is not achievable in SP and LCC-P topologies. Furthermore, the robustness of output current I_o according to M is also vital in the WC charger. In the case of the SS topology, the output current and power are inversely proportional to the mutual inductance. In the SS topology, in order to constantly remain I_o when M reduces, the input voltage V_{in} must be decreased, resulting in an increase of I_{in}. This results in an increase in the conduction losses and the stray fields level in both the primary circuit and the transmitter coil. Moreover, the protection circuit is required to stop charging when M drops below a certain range, and the input power exceeds the maximum limit. The flexibility in the design of the resonant tank is another important criterion, where more resonant components give more flexibility to adjust the output current. In a wireless charger, the installation areas of the wireless coupler coils are normally limited, therefore, self-inductances L_1 and L_2 are limited as well. The coupling coefficient is assumed to be 0.1~0.25 with the standard distance of 15~20 cm between the transmitter and receiver coil for an EV's application [13]. Moreover, the switching frequency is also recommended to be around 85 kHz according to the standard SAE J2954 for wireless stationary charging [25]. Therefore, extra parameters to adjust the output current and power are necessary in many scenarios. Topologies LCC-P and LCC-LCC can meet these requirements, thanks to the additional two capacitors C_{2p} and C_{2s}. The next criterion is the number of resonant components in the compensation tank. The fewer the resonant components, the more advantageous it is to the design and optimization of the overall system. The last criterion is the value of additional inductors in several topologies. Both PP and LCL-LCL topologies require additional inductors at one or both sides, where the inductance values are normally similar to those of the coils and that, consequentially, makes the system becoming bulky. In contrast, additional inductors in LCC-P and LCC-LCC can be freely designed and their value can be significantly smaller than the coil's values.

TABLE 2.1

MAIN CHARACTERISTICS OF CURRENT SOURCE COMPENSATION TOPOLOGIES

Topology	Independent resonant frequency	ZPA operation	Robustness of output current	No. of parameters to adjust output current	No. of components	Additional resonant inductances
Series-series topology (Fig. 2.6.a)	Yes	Yes	No	2	4	Not applicable
Series-parallel topology (Fig. 2.6.b)	No	No	Yes	3	4	Not applicable
Parallel-parallel topology (Fig. 2.6.d)	No	Yes	NA	4	5	Large compared to main coils
LCL-LCL topology (Fig. 2.6.e)	Yes	Yes	Yes	4	6	Same as the main coils
LCC-P topology (Fig. 2.6.f)	Yes	No	Yes	4	6	Small compared to the main coil
LCC-LCC topology (Fig. 2.6.g)	Yes	Yes	Yes	4	8	Small compared to the main coil

2.2.4 Output power control in wireless chargers

In order to adjust the output power, current and voltage under the variation of load and mutual inductance, different control schemes are applied to the EV's wireless chargers. Fig. 2.7 illustrates the typical control schemes in the wireless charger for EVs. Generally, there are three control schemes: duty cycle control, phase-shift control, and frequency control. Depending on

whether the control is performed at the primary or secondary side (i.e. off-board and on-board respectively), control methods are classified as primary and secondary side control. At the primary side, all three control schemes can be applied to the inverter. However, on the secondary side, a regulator (i.e. DC/DC converter) is often used with only the duty control scheme, as illustrated in Fig. 2.8.

According to the new standard SAE J2954 [25], (i.e. Wireless Power Transfer for Light-Duty Plug-in/Electric Vehicles and Alignment Methodology), the frequency band is recommended to be between 81.38 and 90 kHz with the main operating point at 85 kHz. Therefore, the operating frequency in real scenarios is also limited within the above band (i.e. 81.38 to 90 kHz) when applying the frequency control method.
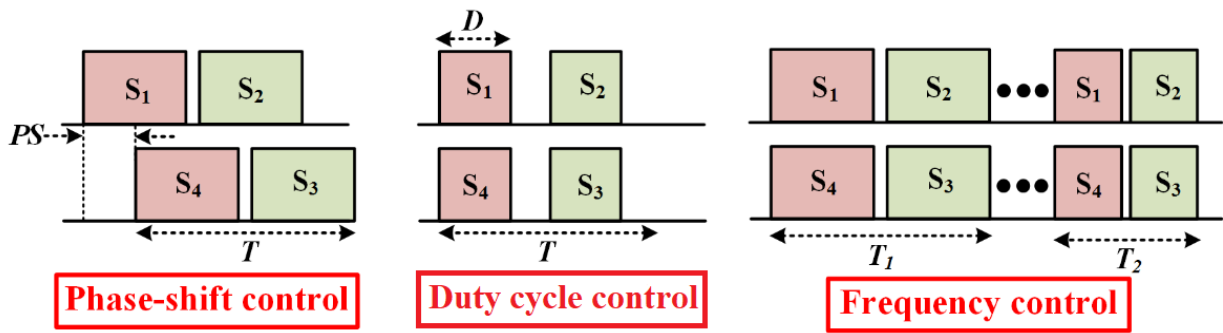
Fig. 2.7. Three typical control schemes in EVs wireless chargers.
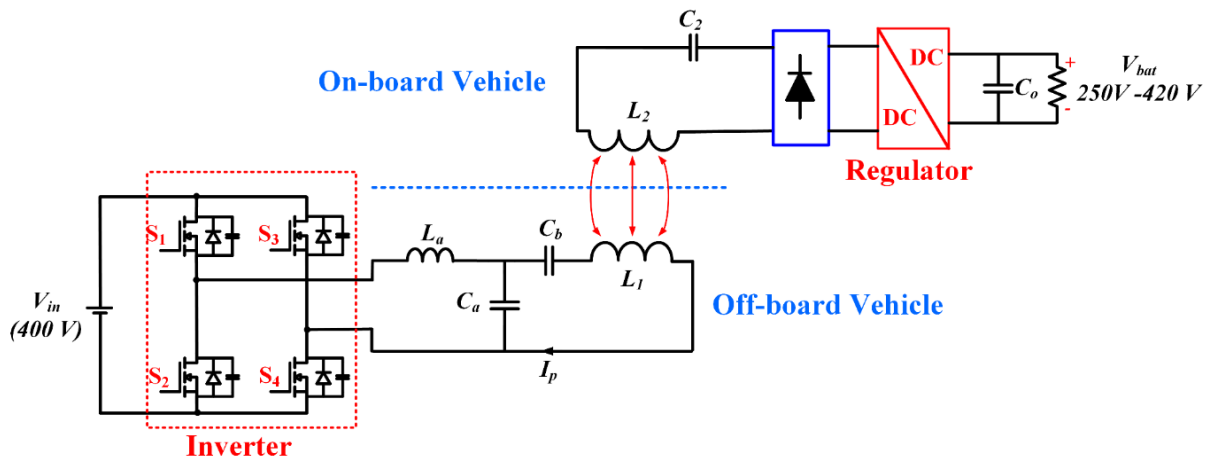
Fig. 2.8. The primary and secondary side controls.

Table 2.2 presents the comparison between three control schemes in which the Pulse Width Modulation (PWM) control constitutes both duty cycle and phase-shift controls. While the PWM control has the advantage of easy implementation, its drawbacks are that it has a high circulating current and it is difficult to achieve soft switching operation for the primary inverter

switches. In contrast, the Pulse Frequency Modulation (PFM) control offers a low circulating current and it is easy to achieve soft switching operation by changing the phase of input impedance when frequency varies. However, it suffers from complex implementation and the bifurcation phenomenon [80].

TABLE 2.2

COMPARISONS OF TWO PRIMARY CONTROL SCHEMES

	PWM control	PFM control
Advantages	- Easy implementation	- Small circulating current - Easy to achieve soft-switching (e.g. ZVS)
Disadvantages	- High circulating current - Difficult to achieve soft-switching (e.g. ZVS)	- Complex implementation - Bifurcation

Table 2.3 illustrates the voltage conversion characteristics of different control schemes. While the phase-shift and duty cycle controls can only provide the buck function, the frequency control can either increase or decrease the output voltage compared to the input voltage based on the voltage gain curve of the circuit [21].

TABLE 2.3

VOLTAGE CHARACTERISTICS OF DIFFERENT CONTROL SCHEMES

	Phase-shift	Duty cycle	Frequency
Inverter (primary)	Buck	Buck	Boost / Buck
Rectifier (secondary)	Buck	Buck	N/A
Regulator (secondary)	N/A	Boost / Buck	N/A

Moreover, in the EV system, the battery is an indispensable component, and lithium-ion batteries are identified as the most competitive candidate to be used in EVs due to their high-power density, long lifecycle, and better safety. To charge lithium-ion batteries, constant current/constant voltage (CC/CV) is often adopted for high-efficiency charging and sufficient

protection. An example charging profile for the Nissan Leaf battery can be found in Fig. 2.9 with a rated power of 6.6 kW. Initially, the charger charges a battery in CC mode and the battery voltage gradually increases. When the battery voltage reaches the maximum charge voltage, the charger changes from the CC mode to the CV mode. The charging process is completed when the battery current reaches a certain value (for example, 0.05 C) [34]. In order to extend the lifetime of the battery, it is necessary for a charger to provide accurate charge current and voltage through stable operations. Since batteries are considered to have varying loads during charging, the charger converter needs to precisely regulate its output to implement the CC/CV charging modes. Typically, PWM is used for converters operating with a fixed frequency, while PFM is used for those operating with a fixed duty cycle [35] - [36]. Sometimes hybrid techniques combining two different techniques of PWM and PFM are also used [37]. When a single resonant converter is used to implement the CC and CV charging mode, the PFM method is often adopted to cope with a wide range of load variation. Then, a wide range of variation in the operation frequency is inevitable for the operation with a varying load [35]. This results in higher circulating current in the converter and a potential loss of the zero-voltage-switching (ZVS) or zero-current-switching (ZCS) characteristics. This also leads to a significant power loss and a reduction in the power transfer capability. Furthermore, it may also result in a bifurcation phenomenon, where the controllability and stability of the system are compromised [36]. In order to avoid these disadvantages, some approaches employ a back-end DC/DC converter to control the output current or voltage, whereas the front-end converter operates at the resonant frequency to achieve the zero-phase-angle (ZPA) operation [38-39]. However, this increases the component counts, losses, and complexity. In order to simplify the control of the wireless charger system and to avoid the above drawbacks of the conventional control methods under wide variations of the load in implementing the CC/CV charging mode, some researchers have utilized the load-independent characteristics of four basic compensation topologies at their resonant frequencies [40]–[42]. It is well-known that among those topologies, the PS topology can achieve the CV charging and the PP topology can achieve the CC charging. Although the SS and SP topologies can achieve both CC and CV charging, the SS fails to achieve the ZPA condition while CV charging, and SP loses the ZPA condition when in CC mode. To achieve the ZPA condition for the entire charging process, hybrid topologies with SS and PS or SP and PP have been proposed in [43] by using additional switches and their associated driver circuits to transform the topology. In order to achieve ZPA in both CC and CV modes without using additional switches, [20-21] have utilized two

different resonant frequencies of the double-sided LCC topology for each CC and CV mode, respectively.
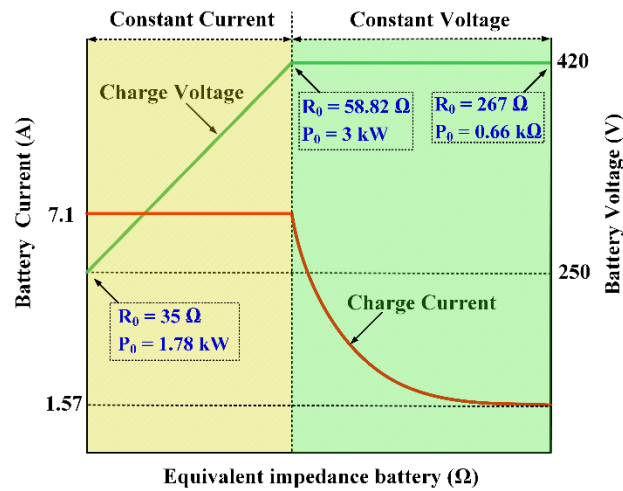
Fig. 2.9. The CC/CV charging profile of the battery and equivalent impedance of the EV battery (i.e. Nissan Leaf battery).

2.3 Wireless dynamic charger for electric vehicles

2.3.1 Motivation of wireless dynamic charging

Although EVs possess many advantages such as clean, efficient and environment-friendly features, the penetration of EVs still limited at the present time due to many technological barriers, including the high requirements of light and robust motors, efficient and compact inverters, and miscellaneous power train units [44]. However, the biggest issue is the on-board energy storage technology. An expensive and large battery with long charging time is normally equipped to achieve a satisfactory EV driving range. Because of the low energy density of these batteries, EVs should be frequently recharged after operating for a certain range. The current available quick chargers require up to 20 minutes to charge a battery fully [45-47]. Moreover, the quick chargers can potentially deteriorate the battery lifetime and always require expensive and large-size charging facilities.

Therefore, wireless dynamic charging (WDC) has been proposed to alleviate such challenges, where the EV charges while in motion. This enables the use of a smaller-sized battery and completely abolishes range anxiety. WDC is commonly developed based on inductive power transfer (IPT) technology, where a time-varying magnetic field is generated by transmitter coils, which are installed underneath a road's surface. The transmitter coils wirelessly power

receiver coils, which charge the EV's battery continuously. The typical structure for a WDC system is illustrated in Fig. 2.10. This is similar to the EVs wireless stationary charging, except that the transmitter is installed under the road surface along the driving direction of the EV. The other feature for WDC systems is that the charging controller for the on-board battery should be located in the secondary side. This is due to the fact that the transmitter may power multiple vehicles simultaneously, and each vehicle's battery specification may be different. Therefore, an independent battery charger converter must be installed on-board of each vehicle. The total length of transmitters in WDC systems is significantly longer compared to the conventional wireless stationary charger.
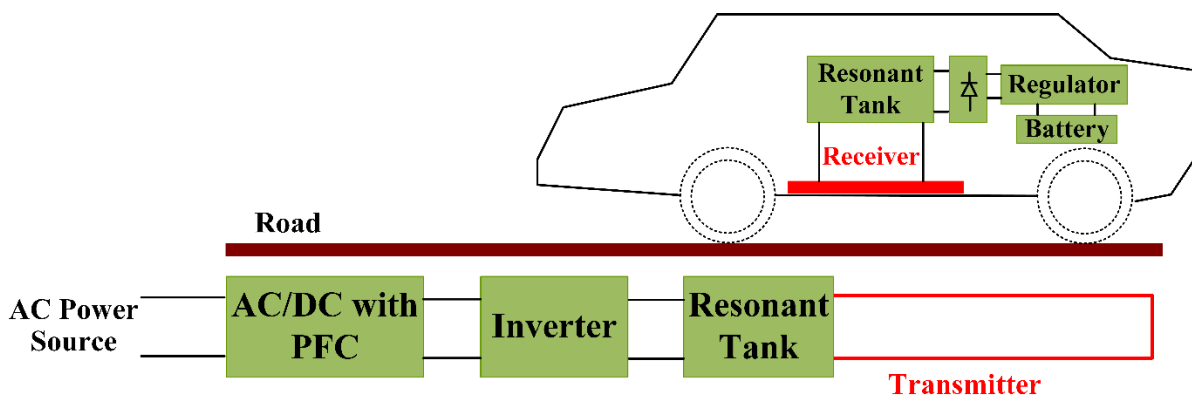
Fig. 2.10. Typical structure of the EV wireless dynamic charging system.

2.3.2 Classification of WDC systems

WDC systems are categorized into short-individual transmitters [48-50] or long-track transmitters [51-53] according to the length of transmitter coils (i.e. Fig. 2.11a and Fig. 2.11b respectively). In the short-individual transmitters, the dimension of the transmitter is same as the receiver, in which the transmitter's area is typical within $1m^2$. Furthermore, multi-transmitter coils are arranged on the primary side to alternatively transfer power to the secondary side. Additionally, each transmitter is connected to an independent compensation circuit, which can be switched ON or OFF depending on the EV's position. When the EV's receiver is aligned with a specific transmitter, then the power switch (or contactor) connects the associated inverter. In order to switch a specific transmitter, position sensors and associated electronic circuits are required. Therefore, the effect of the electromagnetic field to the surrounding environment is minimized and total conduction losses on transmitters are reduced. Moreover, higher efficiency can be achieved, thanks to the higher values of the coupling

coefficient between transmitter and receiver coil and lower conduction losses compared to the long-track transmitter. In the short-individual case, the receiver covers entirely one transmitter coil's area. This results in a higher coupling value compared to the long-track transmitter, where the receiver only covers a small portion of the transmitter's length. However, the short-individual transmitters require more inverters, position sensors and other control circuitries that make the system more complicated and costly. More importantly, when the EV moves between two adjacent transmitters, the coupling coefficients between two adjacent transmitters and receiver reduce significantly, and this results in a pulsating output power. At the position of several receivers, the received power can even reach zero.
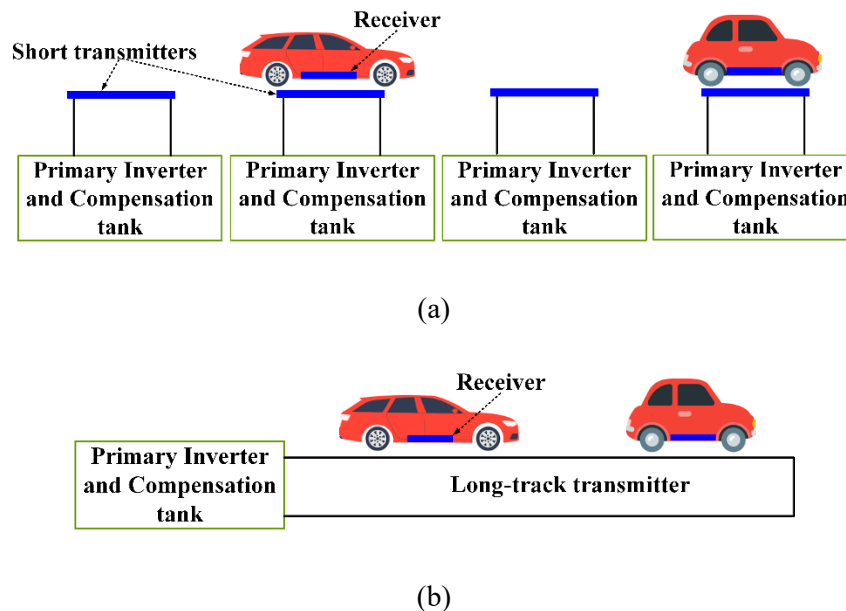
Fig. 2.11. Two types of WDC systems. (a) Short-individual transmitters. (b) Long track transmitter.

On the other hand, the long-track transmitters [51-53] are much longer than the EV's length and only require a single power inverter with one compensation tank, making the system simpler and cheaper, compared to the former structure. However, the low coupling coefficient is recognized as the main drawback of this system as the receiver coil covers only a small portion of the long transmitter coil. This results in lower efficiency and higher stray fields. Several studies were conducted to address the high stray fields problem and also to simplify the structure of the system [54-56]. For example, in [54] and [55], I-type and S-type transmitters were proposed with a width of 10 cm and 4 cm respectively to further reduce the transmitter's

width. Furthermore, stray fields can be substantially reduced if the magnetic polarity of adjacent poles is alternated. The N-type was proposed in [56] to further reduce the volume of ferrite core while maintaining the advantages of the I-type structure. However, the studies also pointed out that the magnetic flux density generated by I-type, S-type or N-type transmitters on a single receiver varies in a nearly sinusoidal function, depending on the receiver's position along the driving direction. According to [54], magnetic flux density reaches its maximum at the centre of each ferrite pole and reduces to nearly zero at the centre between two adjacent poles. Consequently, the induced voltage and received power are significantly varied depending on the EV's position. The received power even reaches nearly zero at some specific positions of the EV while moving along the transmitter. Table 2.4 summarizes the main features of long-track and short-individual transmitters.

TABLE 2.4

COMPARISONS BETWEEN LONG-TRACK AND SHORT-TRACK TRANSMITTER TYPES IN WDC SYSTEMS

	Features	Advantages	Disadvantages
Long-track transmitter	- Between 10's to 100's of meters long (transmitter) - Support multiple vehicles simultaneously	- Simple and requires a minimal number of circuit components - Narrow transmitter width - Lower cost	- Lower efficiency - Higher magnetic field emissions
Short-individual transmitter	- Similar size as the stationary system. - Multiple short transmitters form a tracking lane.	- More flexible to design the total length of the powered roadway - Higher efficiency - Lower magnetic field emissions.	- Complexity (more compensation tanks, converters, sensors, control circuits, etc.) - Higher initial cost

2.4 Challenges of EVs wireless dynamic charging

There are several technical challenges to designing an effective wireless dynamic charging for Electric Vehicles applications. Based on the literature review, the three following issues are the most serious:

(1) Output power variation

(2) Requirement of the high-power capability

(3) High cost and complexity

This section is devoted to analysing these issues and reviews the proposed solutions discussed in the open literature.

2.4.1 Minimizing the output power variation

As the receiver is always in motion, the coupling coefficient between transmitter and receiver coils varies continuously. This leads to a reduction in the output power and efficiency under misalignment scenarios, which occurs during the movement process of the vehicle. This issue happens in both short-track and long-track WDC systems. The output power pulsation shortens the battery life compared with constant power charging [34]. In the short-track system, when the EV moves between two adjacent transmitter windings, the output power becomes pulsating and significantly reduced. In order to demonstrate this issue, some simulations are conducted using Finite Element Analysis (FEA) software, Maxwell 3D. Fig. 2.12 portrays the simulation model and associated results of the short-track WDC system including five transmitter windings (namely L_1, L_2, L_3, L_4 and L_5) and one receiver, L_r. According to that, the coupling factor k_{ir} is at its maximum when the transmitter $L_i (i = 1,2,3,4,5)$ is aligned with the receiver. Otherwise, k_{ir} is almost zero. The effective coupling k_r is under variation as shown in Fig. 2.12(b), which results in a variation of output power. It is assumed that all the transmitter windings are constantly turned ON in the simulation. In the real scenario, when $L_i (i = 1,2,3,4,5)$ are turned ON and OFF alternately, then effective coupling k_r could even reach to zero.
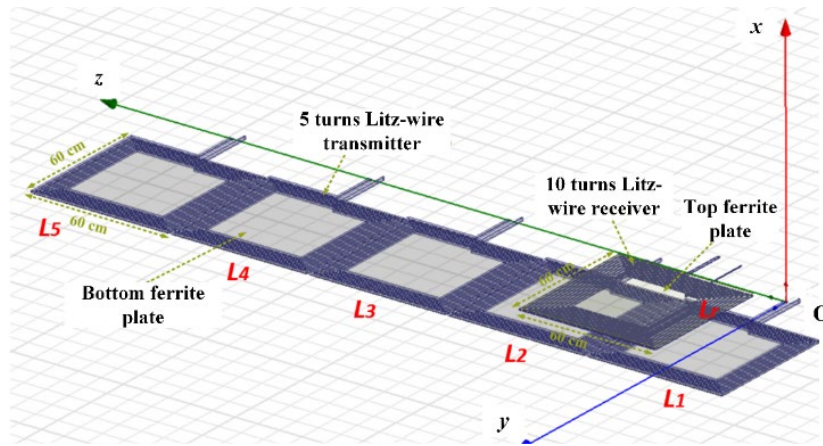
(a)
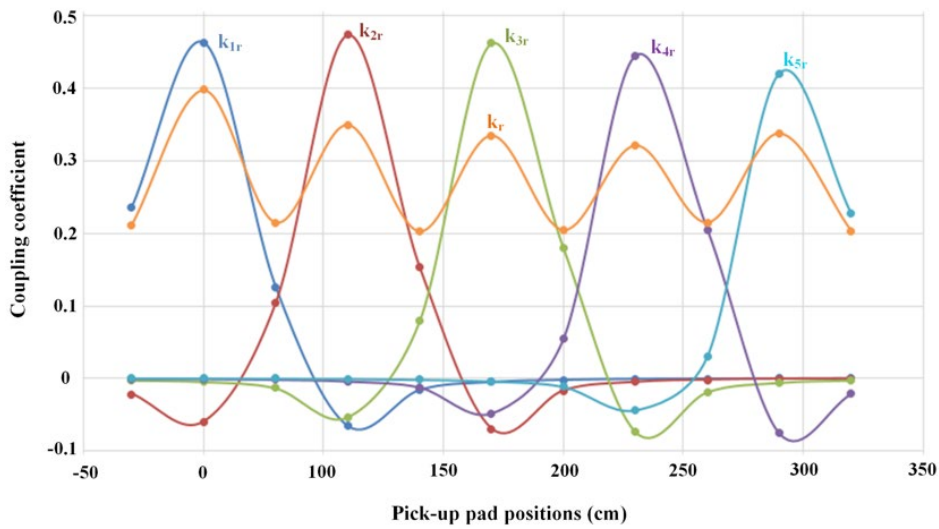
(b)

Fig. 2.12. Simulation verification of the short-track transmitter. (a) Simulation model in the Maxwell 3D. (b) Results of coupling factors.

In the long-track transmitter type, several popular structures of I-type, S-type and N-type are presented in Fig. 2.13 (a), (b) and (c) respectively. In these structures, the transmitter utilizes different alternating magnetic polarities for adjacent ferrite poles to reduce the surrounding stray fields. However, the magnetic flux density generated by these structures on a single receiver varies in a nearly sinusoidal function, depending on the receiver's position along the driving direction. Therefore, the mutual inductance between the transmitter and receiver's windings is depicted in Fig. 2.13 (d), in which l_o is the length of two adjacent poles. Therefore, the induced voltage and received power are significantly varied depending on the EV's position while moving along the transmitter and even reaches to nearly zero at several particular positions of the EV.
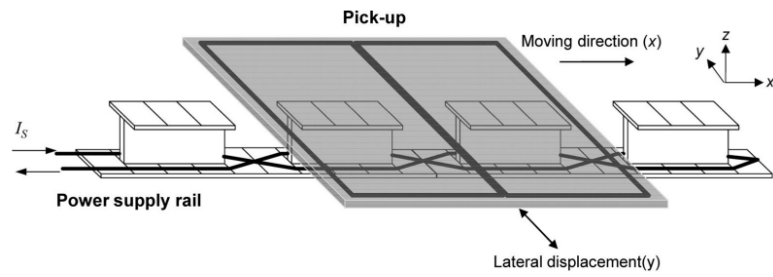
(a)
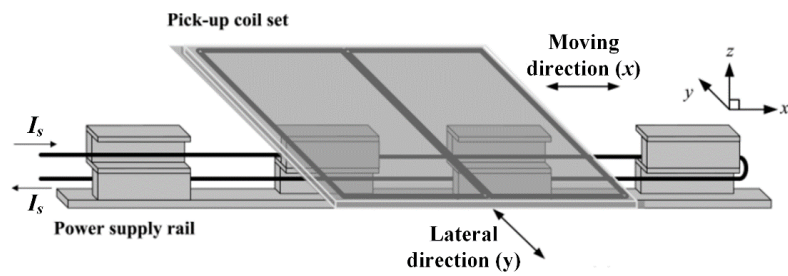
(b)
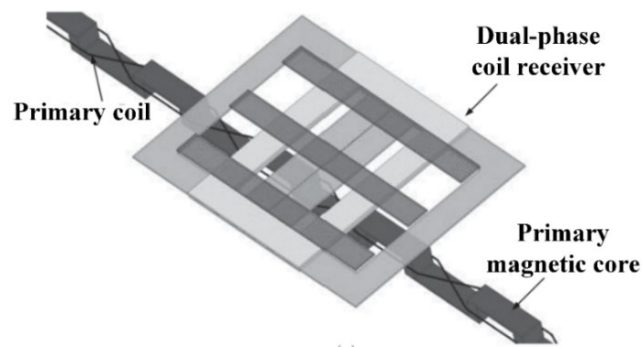
(c)
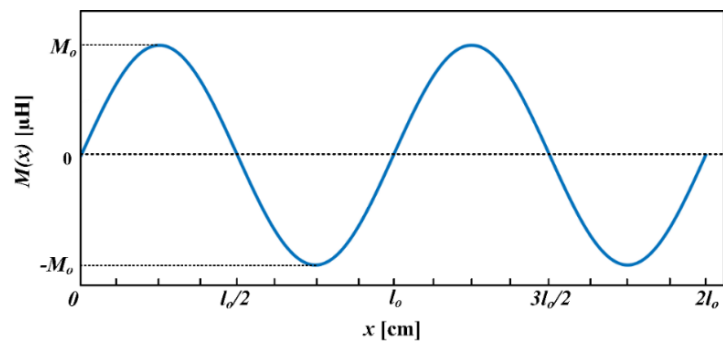
(d)

Fig. 2.13. Different transmitter structures in the long-track type. (a) I-shape transmitter [54]. (b) S-shape transmitter [55]. (c) N-shape transmitter [56]. (d) Mutual inductance variation while the receiver is in motion for all three kinds above.

In order to address the pulsating output power, a number of studies attempted to realise constant output power in both transmitter structures. Starting with the short-track type, the stable output power is achieved by proper design of various compensation tanks (i.e. discussed in Section 2.2.3) to compensate for misalignment [57-62]. In this section, more analyses are provided under the high variation of coupling coefficient scenarios. In [57], a generalized design method of the primary compensation tank is presented, in which a new T-type tank (i.e. Fig. 2.14(a)) is analysed. The design of the primary LCC compensation tank is optimized in [58] while the S/CLC topology (series in primary and CLC in the secondary side) is presented in [61]. The main objective of these methods [57-61] is to relate the output power to the mutual inductance and resonant parameters, to optimize the resonant parameters. In [62], the output power stabilization is achieved by utilizing the double transmitter windings and the T-type compensation tank. The advantage of this method is that the power can be stable within a range of misalignment without any additional coil's winding, resonant component or control; therefore, the cost and system's complexity are minimized. However, this method is only effective with a certain range of misalignment, and the output power still significantly drops if misalignment level is out of the above certain range. As illustrated in Fig. 2.14(b) (i.e. extracted from [57]), the output power varies between 300 and 400W when the coupling k changes from 0.13 to 0.25. However, with large misalignment (k varies from 0.02 to 0.13), the output power drops from 300W to 20W and no further improvement is made compared to the conventional topologies (i.e. SS).

(a)   (b)
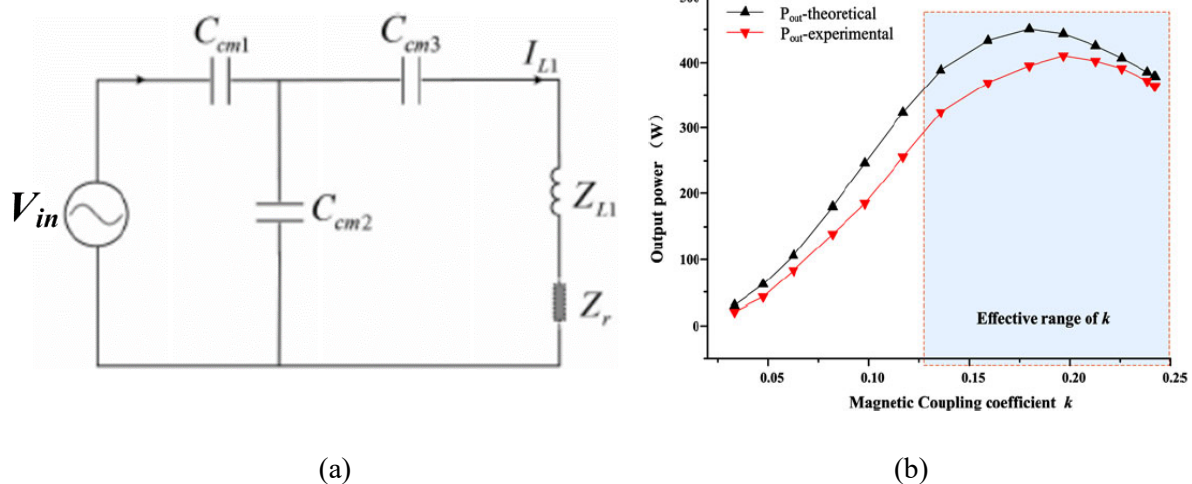
Fig. 2.14. (a) T-type primary compensation in [57]. (b) Output power versus the coupling coefficient by using optimized T-type topology [57].

Alternatively, in [63], the variation of the output power is reduced by arranging the transmitter segments closer to each other. However, this method is only effective with specific dimensions of the transmitter and receiver. In [64], the low output power variation is attained by employing three parallel-connected half-bridge inverters and optimized receiver length. However, constant power is only achieved if the ratio of the receiver's length over the transmitter's length is 1.5, which may not be suitable in real applications where receivers with different dimensions exist. Furthermore, other methods that adjust the transmitter current under misalignment are also reported in the literature [65-66]. Transmitter current is controlled by a primary inverter and/or a primary DC/DC converter to increase its amplitude when the coupling coefficient is reduced. However, this comes at the expense of reduced efficiency due to the increased losses at the primary side.

Similarly, several attempts have been reported in the literature aiming at reducing the output pulsation of the long-track systems. For instance, the authors in [78] added additional receiver windings to create a multiphase receiver system with a single primary transmitter. The coil's dimensions on both sides are optimized to achieve constant output power. Another solution was suggested by [79], where two long-track primary transmitter coils with two independently controlled inverters are arranged. The constant output power is attained by controlling the amplitude and phase of the inverters' outputs. However, this requires information from the secondary side such as load resistance and mutual inductances, which results in a complicated measurement and communication, especially when the EV is in motion. Furthermore, the control method presented in [79] becomes even more complicated when multiple loads (EVs) are considered.

Alternatively, the power can be regulated by using an external on-board source as illustrated in Fig. 2.15. Authors in [50] and [67] used the passive and active parallel lithium-capacitor (LiC) unit to smooth both grid-side and vehicle side powers in an EV's dynamic charging system. Depending on the coupling variation between the transmitter and the receiver, different power levels are required to flat powers in both the grid and vehicle side. One DC/DC converter is utilized to conduct this task. The results showed that a reduction of 81% and 84% power pulsation was achieved at the grid and vehicle sides respectively. Although the capital cost is relatively high due to the need for LiC modules, it features simplicity, robustness and easy implementation.
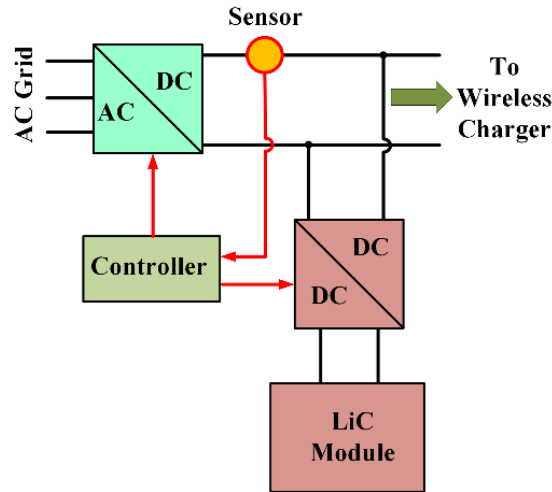
Fig. 2.15. The configuration of using external sources (in Grid side) in [50], [67].

2.4.2 The need of high-power capability

In addition to the output power pulsation challenge, the transferred power of a single-phase WDC system is limited by voltage and current ratings of semiconductor devices, transmitter coil and compensation circuits. In real applications, several EVs may need to be charged simultaneously; thus the high-power demand becomes a necessity. It is also important to note that different vehicles may require different power levels. Therefore, the primary side of the WDC system must be able to provide the highest power demand to meet these requirements.

Moreover, the power level required for public transport such as electric bus, truck, and train systems may go up to hundreds of kilowatts or even megawatts scale [68-71]. In such applications, the single-phase system may not be the right option. Therefore, multi-phase systems are recognized as an alternative to transfer higher output power. In [68], a 1-MW wireless dynamic charger system for the high-speed train is developed using multi-phase receivers as shown in Fig. 2.16. Four receivers with a maximum power of 200kW each are utilized in the secondary side.

The multi-phase WDC system can be modelled as in Fig. 2.17, where at the primary side, a number of transmitters $\left(L_{pi}, i = 1, n\right)$ are utilized to supply power to multiple vehicles at the same time. In the secondary side, several receivers $(L_{si}, i = 1, n)$ are installed to collect the power from primary transmitters. Multi-phase WDC has the advantages of providing higher output power levels; however, it comes at the expense of higher cost and larger space requirement.
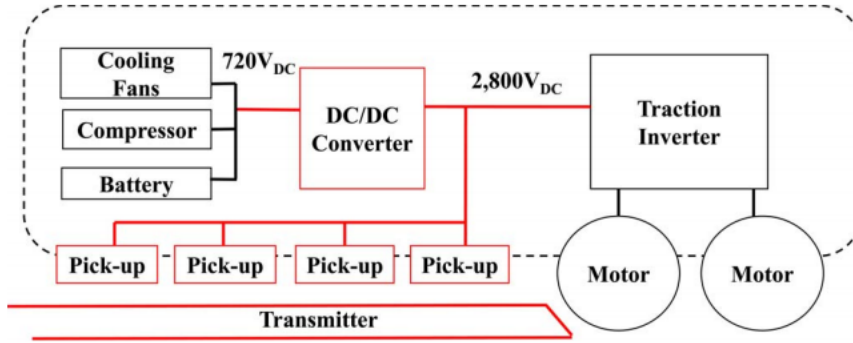
(a)
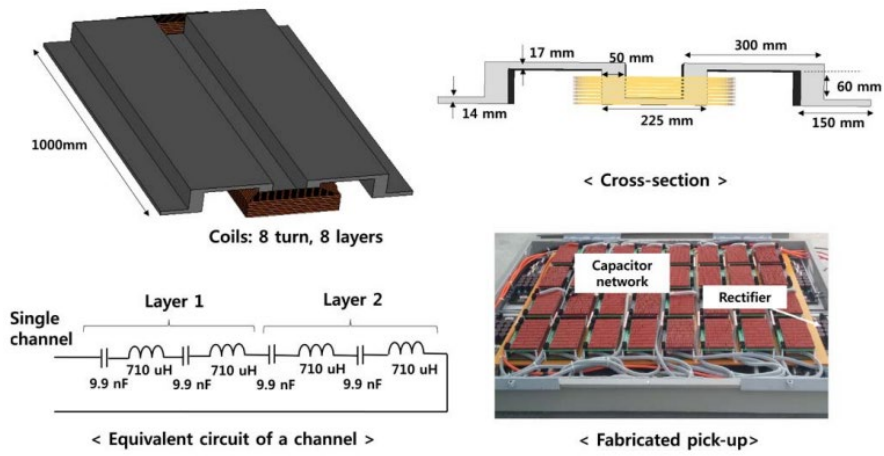
(b)

Fig. 2.16. (a) Electric block diagram of the train using the WPT system. (b) Photograph's prototype of one receiver pad.
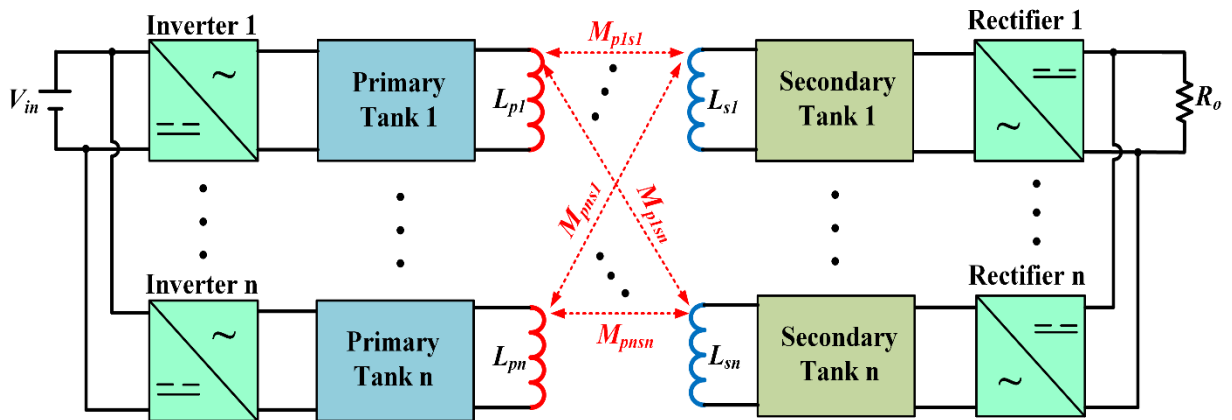
Fig. 2.17. The structure of the multiphase WDC system.

2.4.3 Implementation cost and complexity challenges

Another important factor to be considered in designing a WDC system is the implementation cost [72-74]. The initial cost of the WDC system for EVs is significantly higher than its stationary counterpart as well as the conventional conductive charger. This is obviously due to the higher cost of the charging infrastructure on the primary side, which consists of power inverters, transmitter coils and the associated capacitor bank. Moreover, the roads may need to be redesigned, which contributes to the higher cost. The associated cost of several WDC projects is reported. For example, there is the PATH (Partners for Advanced Transit and Highways) project (i.e. Fig. 2.18), which started in 1992 to determine the technical viability of WDC for electric buses at the University of California, Berkeley [72, 73]. The system achieved 60% efficiency at 60kW output power and 7.6 cm air-gap. The total construction cost of the prototype was reported to be around 1 million $ per km, resulting in the system not being successfully commercialized. Moreover, operating at a low frequency of 400 Hz, it required a bulky and heavy transmitter as well as a large current through the transmitter winding.
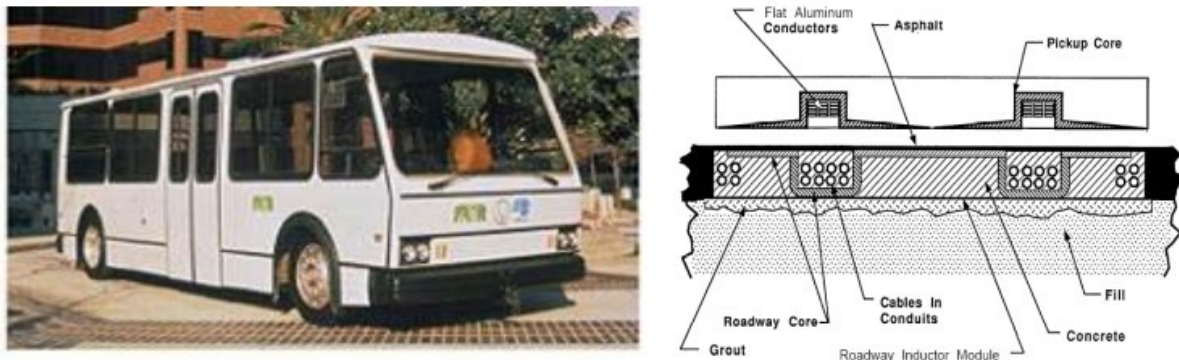
Fig. 2.18. The first operational prototype WDC in the PATH project [73]. Left: appearance of the developed RPEV bus. Right: prototype coils of the WDC system.

The advancements in semiconductor power devices enable WDC systems to operate at several to hundred kHz frequency. This significantly reduces the size and volume of the transmitter coil as well as the transmitter's current. Not only can the power level and efficiency be improved, but the associated cost with the transmitter can also be reduced significantly. Another example is the OLEV project, which was led by KAIST, Korea, where an efficiency of 83% was achieved at an output power of 60kW and an air gap of 20 cm [55]. Furthermore, the coupler coil cost contributes to more than 80% of the total deployment cost of the WDC system [44]. Therefore, if the coupler's parameters are under variation, the total system cost would vary as well. For recent WDC projects, researchers tried to narrow the width of the

transmitter module as much as possible to minimize the implementation cost and the stray fields level when operating at high power levels. Specifically, an S-type transmitter with the smallest width of only 4 cm reduces the associated cost to around $850k per km, which can be potentially further reduced to two to four times with mass production. [74]. A detailed cost breakdown of the KAIST project is presented in Table 2.5.

 In summary, the transmitter dominates the total system cost and should be appropriately designed with the aim of reduced width and less copper and ferrite material but keeping the requirement of stray fields and higher output power and efficiency in mind.

TABLE 2.5

THE COST BREAKDOWN EXAMPLE OF WDC INFRASTRUCTURE (DEVELOPMENT COST ONLY) [74]

Unit price (breakdown)			Dual-type rail		I-type rail		Remark
Level 1	Level 2	Cost [$/No]	No / km	Sum [$/km]	No / km	Sum [$/km]	
Inverter	100kW	55,000	4	220,000	4	220,000	
Cable	Supply cable	54,000	2	108,000	4.4	237,600	250A
	Common cable	54,000	2	108,000	2	108,000	250A
Cable protector	FRP pipe	15,000	4	60,000	0	0	
	FRP package	26,000	0	0	1	25,920	
Core	Rib type	250,000	1	250,000	0	0	20 EA cost
	Square type	96,000	0	0	1	96,000	
Capacitor	Cap. box	5,000	40	200,000	0	0	
	Module type	300	0	0	500	150,000	
Road construction	Concrete	60,000	1	60,000	0	0	
	Asphalt uncover	2,000	1	2,000	0.5	1,000	
	Asphalt cover	11,000	1	11,000	0	0	3.5m width, 5cm thickness
Misc.	Others	50,000	1	50,000	0.2	10,000	
Total				1,069,000		848,520	I-type is about 80% of Dual-type

 In addition to the implementation cost, other technical issues should be considered in the design of the WDC system. The first issue is communication between the primary and the secondary sides, which is required for control and protection purposes. In a stationary charging system, a communication link normally exchanges the data (voltage, current, state of charge, etc.) between the primary and the secondary (EV) sides [75]. However, this is apparently not possible in WDC, and these signals must be sent wirelessly. Therefore, a wireless communication system needs to be considered (i.e. NRF24L01 in [75] as shown in Fig. 2.19). Moreover, these wirelessly transmitted signals are subjected to delay, inaccuracy or misleading that may affect the operation of the WDC. Furthermore, in real scenarios, there are multiple vehicles involved simultaneously, requiring the primary controller to deal with multiple signals at a time. This therefore imposes another challenge in the design of a robust and accurate WDC system. As a result, wireless communication is avoided in most EV dynamic charging projects.

Control is applied independently in each primary and secondary side to avoid wireless communication.
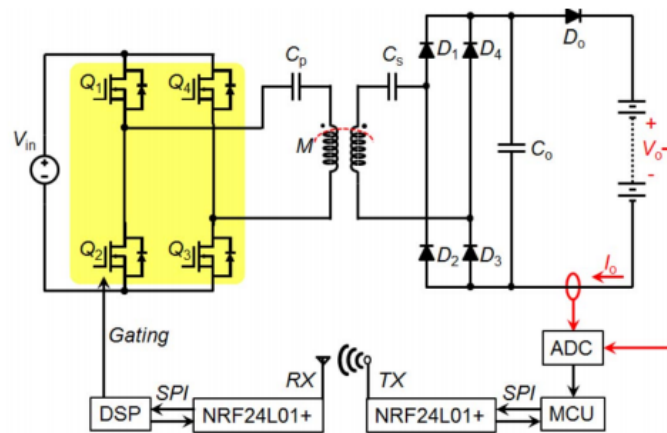
Fig. 2.19. Wireless signal communication used in an EV wireless stationary charger [75].

The potential harm of a WDC system to pedestrians and living animals is of a prime concern as well. The electromagnetic field generated by the wireless coupler coils may induce high field strength in the body tissue of humans and living animals nearby. This causes the issues of the whole-body heat stress, excessive localized tissue heating and adverse health effects [29]. Therefore, an organization providing international safety guidance, namely the International Commission on Non-Ionizing Radiation Protection (ICNIRP), has been established to limit human exposure to the stray fields, aiming at preventing adverse health effects [76]. The reference safety restrictions of both electric field and magnetic field are mentioned in the ICNIRP standard. In detail, the limitations of the average RMS flux densities should not be greater than 27 µT, and occupational exposure is 100 µT in the frequency range of 1 Hz to 100 kHz for the general public [76]. On the other hand, the electric field limitations for the general public is 83 V/m, for 170 V/m [76]. The magnetic field depends heavily on the power level of the wireless charger, the coupler shape and dimension as well as the misalignment level. The coupler design needs to guarantee that the magnetic field exposure is less than 27 µT at a specific distance from the transmitter centre. In contrast with for the stationary charging system, a pedestrian can easily incidentally access the charging zone (i.e. charging station areas). However, it is not easy for pedestrians to enter near the charging zone in the dynamic charging system. The reason is that the transmitters are normally installed on a road where only vehicles are allowed to enter. Therefore, the ICNIRP standard should only apply at a certain distance from transmitters, for example 1 or 2 metres from the transmitter. Even that, the magnetic coupler should be designed to minimize the stray fields level as much as possible

because the WDC system typically operates at a high-power level. If the magnetic field at a certain distance is still larger than 27 µT, shielding or stray fields cancel coils must be included for safety [77]. One stray field cancel method is presented in [77] for dynamic charging and depicted in Fig. 2.20.
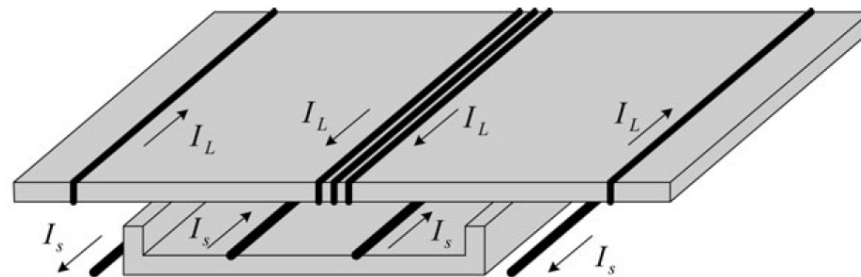
(a)
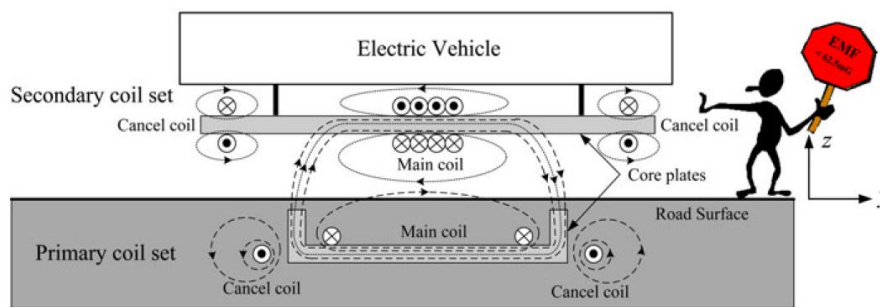
(b)

Fig. 2.20. Configuration of U-type primary main coil and cancel coils for WDC system [77]. (a) Bird's view. (b) Cross-section view.

2.5 Chapter summary

This chapter reviews different aspects of a wireless dynamic charging for Electric Vehicles. Starting from the principle of a wireless power transfer system, it illustrates how output power is related to other factors of the WPT system such as operating frequency, mutual inductance and quality factor of the coils. It is apparent that the output power and system efficiency are very sensitive to the air-gap and misalignment levels between the couplers.

Next, different aspects of the EV wireless stationary charger, including compensation tank, coupler topologies and control schemes, are analysed. In each section, different topologies and

methods are extensively compared. It also states how the wireless charger should be designed to be more suitable with the Li-Ion battery (the most popular battery type in the current EV technology).

To address the inherent downside of using a heavy, bulky and expensive on-board battery, the concept of wireless dynamic charging (WDC) is presented. WDC allows EVs to be charged wirelessly while in motion. As a result, the on-board battery size and weight of EVs can be greatly reduced, and the driving range limitation can be completely alleviated. Based on inductive power transfer technology, WDC has a similar circuit configuration with stationary charging. However, the design of the transmitter in the WDC system is significantly different. It is because the total length of the transmitter must be dramatically longer than in the case of the stationary system. Based on the length of each transmitter module, WDC can be classified into long-track and short-individual types. Each type owns different advantages and disadvantages regarding efficiency, stray fields level, associated cost and complexity, etc. However, both systems reveal several similar technical challenges. They include high output power pulsation while the EV is in motion, requiring high-power level, higher implemented cost and a communication link between two sides, as well as concerns about electromagnetic field exposure.

2.6 References

[1] M. Yilmaz and P. T. Krein, "Review of battery charger topologies, charging power levels, and infrastructure for plug-in electric and hybrid vehicles," IEEE Transactions on Power Electronics, vol. 28, no. 5, pp. 2151–2169, May 2013.

[2] B. Singh, B. N. Singh, A. Chandra, K. Al-Haddad, A. Pandey, and D. P. Kothari, "A review of three-phase improved power quality ac–dc converters," IEEE Transactions on Industrial Electronics, vol. 51, no. 3, pp. 641–660, Jun. 2004.

[3] M. A. Fasugba and P. T. Krein, "Gaining vehicle-to-grid benefits with unidirectional electric and plug-in hybrid vehicle chargers," in IEEE Vehicle Power and Propulsion Conference, Sep. 2011, pp. 1–6.

[4] Y. Lee, A. Khaligh, and A. Emadi, "Advanced integrated bi-directional AC/DC and DC/DC converter for plug-in hybrid electric vehicles," IEEE Transactions on Vehicular Technology, vol. 58, no. 3, pp. 3970–3980, Oct. 2009.

[5] Y. Du, S. Lukic, B. Jacobson, and A. Huang, "Review of high power isolated bi-directional DC-DC converters for PHEV/EV DC charging infrastructure," 2011 IEEE Energy Conversion Congress and Exposition, Phoenix, Sep. 2011, pp. 553–560.

[6] X. Zhou, S. Lukic, S. Bhattacharya, and A. Huang, "2009 IEEE Vehicle Power and Propulsion Conference, Dearborn, MI," in Proc. IEEE Veh. Power and Propulsion Conf., Sep. 2009, pp. 1716–1721.

[7] X. Zhou, G. Wang, S. Lukic, S. Bhattacharya, and A. Huang, "Multifunction bi-directional battery charger for plug-in hybrid electric vehicle application," 2009 IEEE Energy Conversion Congress and Exposition, San Jose, CA, Sep. 2009, pp. 3930–3936.

[8] S. Haghbin, K. Khan, S. Lundmark, M. Alakula, O. Carlson, M. Leksell, ¨ and O. Wallmark, "Integrated chargers for EV's and PHEV's: Examples and new solutions," ICEM 2010, Rome, 2010, pp. 1–6.

[9] V. Doan, V. Vu, H. Vu, D. Tran and W. Choi, "Intelligent charger with online battery diagnosis function," in the 9th International Conference on Power Electronics and ECCE Asia (ICPE-ECCE Asia), Seoul, 2015, pp. 1644-1649.

[10] D. Thimmesch, "An SCR inverter with an integral battery charger for electric vehicles," IEEE Transactions on Industry Applications, vol. 21, no. 4, pp. 1023–1029, Aug. 1985.

[11] W. E. Rippel, "Integrated traction inverter and battery charger apparatus," U.S. Patent 4 920 475, Apr. 1990.

[12] H. C. Chang and C. M. Liaw, "Development of a compact switched reluctance motor drive for EV propulsion with voltage-boosting and PFC charging capabilities," IEEE Transactions on Vehicular Technology, vol. 58, no. 7, pp. 3198–3215, Sep. 2009.

[13] S. Li and C. C. Mi, "Wireless power transfer for electric vehicle applications," IEEE Journal of Emerging and Selected Topics in Power Electronics, vol. 3, no. 1, pp. 4–17, Mar. 2015.

[14] C. W. Wang, O. H. Stielau, and G. A. Covic, "Design considerations for a contactless electric vehicle battery," IEEE Transactions on Power Electronics, vol. 52, no. 5, pp. 1308–1314, Oct. 2005.

[15] U. K. Madawala and D. J. Thrimawithana, "A bidirectional inductive power interface for electric vehicles in V2G systems," IEEE Transactions on Industrial Electronics, vol. 58, no. 10, pp. 4789–4796, Oct. 2011.

[16] H. H. Wu, A. Gilchrist, K. D. Sealy, and D. Bronson, "A high efficiency 5 kW inductive charger for EVs using dual side control," IEEE Transactions on Industrial Informatics, vol. 8, no. 3, pp. 585–595, Aug. 2012.

[17] N. A. Keeling, G. A. Covic, and J. T. Boys, "A unity-power-factor IPT pickup for high-power applications," IEEE Transactions on Industrial Electronics, vol. 57, no. 2, pp. 744–751, Feb. 2010.

[18] Z. Pantic, B. Sanzhong, and S. Lukic, "ZCS LCC-compensated resonant inverter for inductive-power-transfer application," IEEE Transactions on Industrial Electronics, vol. 58, no. 8, pp. 3500–3510, Aug. 2011.

[19] S. Li, W. Li, J. Deng, T. D. Nguyen, and C. C. Mi, "A double-sided LCC compensation network and its tuning method for wireless power transfer," IEEE Transactions on Vehicular Technology, vol. 64, no. 6, pp. 2261–2273, Jun. 2015.

[20] V. B. Vu, V. T. Doan, V. L. Pham, and W. J. Choi, "A new method to implement the constant current- constant voltage charge of the inductive power transfer system for electric vehicle applications," in Proc. IEEE Transp. Electrification Conf. Expo., Asia-Pac., Busan, South Korea, 2016, pp. 449–453.

[21] V. B. Vu, D. H. Tran, and W. Choi, ''Implementation of the constant current and constant voltage charge of inductive power transfer systems with the double-sided LCC compensation topology for electric vehicle battery charge applications,'' IEEE Transactions on Power Electronics, vol. 33, no. 9, pp. 7398–7410, Sep. 2018.

[22] W. Li, H. Zhao, S. Li, J. Deng, T. Kan, and C. C. Mi, "Integrated LCC compensation topology for wireless charger in electric and plug-in electric vehicles," IEEE Transactions on Industrial Electronics, vol. 62, no. 7, pp. 4215–4225, Jul. 2015.

[23] J. Deng, W. Li, T. D. Nguyen, S. Li, and C. C. Mi, "Compact and efficient bipolar coupler for wireless power chargers: Design and analysis," IEEE Transactions on Power Electronics, vol. 30, no. 11, pp. 4215–4225, Nov. 2015.

[24] T. Kan, T. D. Nguyen, J. C. Wjite, R. K. Malhan, and C. C. Mi, "A new integration method for an electric vehicle wireless charging system using LCC compensation topology," IEEE Transactions on Power Electronics, vol. 32, no. 2, pp. 1638–1650, Feb. 2017.

[25] SAE J2954 - Wireless Power Transfer for Light-Duty Plug-in/Electric Vehicles and Alignment Methodology, published by SAE International, Oct. 2020.

[26] M. Budhia, J. Boy, G. Covic, and C. Y. Huang, "Development of a singleside flux magnetic coupler for electric vehicle IPT charging systems," IEEE Transactions on Industrial Electronics, vol. 60, no. 1, pp. 318–328, Jan. 2013.

[27] Y. Nagatsuka, N. Ehara, Y. Kaneko, S. Abe, and T. Yasuda, "Compact contactless power transfer system for electric vehicles," the 2010 International Power Electronics Conference - ECCE ASIA -, Sapporo, 2010, pp. 807–813.

[28] M. Budhia, J. Boy, and G. Covic, "Design and optimization of circular magnetic structures for lumped inductive power transfer systems," IEEE Transactions on Power Electronics, vol. 26, no. 11, pp. 3096–3108, Nov. 2011.

[29] W. Zhang, J. White, R. Malhan, and C. C. Mi, "Loosely coupled transformer coil design to minimize EMF radiation in concerned areas," IEEE Transactions on Vehicular Technology, vol. 65, no. 6, pp. 4779–4789, Jun. 2016.

[30] W. X. Zhong, C. Zhang, X. Liu, and S. Y. R. Hui, "A methodology for making a three-coil wireless power transfer system more energy efficient than a two-coil counterpart for extended transfer distance," IEEE Transactions on Power Electronics, vol. 30, no. 2, pp. 933–942, Feb. 2015.

[31] S. Moon, B. C. Kim, S. Y. Cho, C. H. Ahn, and G. W. Moon, "Analysis and design of a wireless power transfer system with an intermediate coil for high efficiency," IEEE Transactions on Industrial Electronics, vol. 61, no. 11, pp. 5861– 5870, Nov. 2014.

[32] D. H. Tran, V. B. Vu, V. L. Pham, and W. Choi, "Design and implementation of high efficiency wireless power transfer system for on-board charger of electric vehicle," 2016 IEEE 8th International Power Electronics and Motion Control Conference (IPEMC-ECCE Asia), Hefei, May 2016, pp. 2466–2469.

[33] D. H. Tran, V. B. Vu, and W. J. Choi, "Design of a high efficiency wireless power transfer system with intermediate coils for the on-board chargers of electric vehicles," IEEE Transactions on Power Electronics, vol. 33, no. 1, pp. 175– 187, Jan. 2018.

[34] D. Andrea, Battery Management Systems for Large Lithium-Ion Battery Packs, 1st ed. Boston, MA, USA: Artech House, 2010.

[35] C. Zheng et al., "High efficiency contactless power transfer system for electric vehicle battery charging application," IEEE Journal of Emerging and Selected Topics in Power Electronics, vol. 3, no. 1, pp. 65–74, Mar. 2015.

[36] C. W. Wang, G. A. Covic, and O. H. Stielau, "Power transfer capability and bifurcation phenomena of loosely coupled inductive power transfer systems," IEEE Transactions on Industrial Electronics, vol. 51, no. 1, pp. 148–157, Feb. 2004.

[37] R. Bosshard, J. W. Kolar, and B. Wunsch, "Control method for inductive power transfer with high partial-load efficiency and resonance tracking," 2014 International Power Electronics Conference (IPEC-Hiroshima 2014 - ECCE ASIA), Hiroshima, May 2014, pp. 2167–2174.

[38] J. Shin et al., "Design and implementation of shaped magnetic-resonance based wireless power transfer system for roadway-powered moving electric vehicles," IEEE Transactions on Industrial Electronics, vol. 61, no. 3, pp. 1179–1192, Mar. 2014.

[39] V. Vu, V. Phan, D. Nguyen, T. Logenthiran and R. T. Naayagi, "Design and implementation of a multi-output inductive charger for electric vehicles," 2016 IEEE International Conference on Sustainable Energy Technologies (ICSET), Hanoi, 2016, pp. 414-419.

[40] W. Zhang, S. C. Wong, C. K. Tse, and Q. Chen, "Design for efficiency optimization and voltage controllability of series–series compensated inductive power transfer systems," IEEE Transactions on Power Electronics, vol. 29, no. 1, pp. 191–200, Jan. 2014.

[41] W. Zhang, S. C. Wong, and C. K. Tse, "Analysis and comparison of secondary series- and parallel-compensated inductive power transfer systems operating for optimal efficiency and load-independent voltage-transfer ratio," IEEE Transactions on Power Electronics, vol. 29, no. 6, pp. 2979–2990, Jun. 2014.

[42] C. Auvigne, P. Germano, D. Ladas, and Y. Perriard, "A dual-topology ICPT applied to an electric vehicle battery charger," 2012 XXth International Conference on Electrical Machines, Marseille, Mach., 2012, pp. 2287–2292.

[43] X. Qu, H. Han, S. C. Wong, C. K. Tse, and W. Chen, "Hybrid IPT topologies with constant-current or constant-voltage output for battery charging applications," IEEE Transactions on Power Electronics, vol. 1, no. 1, pp. 6329–6337, Jan. 2015.

[44] S. Y. Choi, B. W. Gu, S. Y. Jeong, and C. T. Rim, "Advances in wireless power transfer systems for roadway-powered electric vehicles," IEEE Journal of Emerging and Selected Topics in Power Electronics, vol. 3, no. 1, pp. 18–36, Mar. 2015.

[45] N. H. Kutkut, D. M. Divan, D. W. Novotny, and R. H. Marion, "Design considerations and topology selection for a 120-kW IGBT converter for EV fast charging," IEEE Transactions on Power Electronics, vol. 13, no. 1, pp. 169–178, Jan. 1998.

[46] J. D. Marus and V. L. Newhouse, "Method for charging a plug-in electric vehicle," U.S. Patent 20 130 234 664, Sep. 12, 2013.

[47] C. Praisuwanna and S. Khomfoi, "A quick charger station for EVs using a pulse frequency technique," 2013 IEEE Energy Conversion Congress and Exposition, Denver, CO, Sep. 2013, pp. 3595–3599.

[48] G. A. Covic and J. T. Boys, "Modern trends in inductive power transfer for transportation applications," IEEE Journal of Emerging and Selected Topics in Power Electronics, vol. 1, no. 1, pp. 28–41, Mar. 2013.

[49] Q. Zhu, L. Wang, Y. Guo, C. Liao, and F. Li, "Applying LCC compensation network to dynamic wireless EV charging system," IEEE Transactions on Industrial Electronics, vol. 63, no. 10, pp. 6557–6567, Oct. 2016.

[50] J. M. Miller, O. C. Onar, C. P. White, and S. Campbell, "Demonstrating dynamic wireless charging of an electric vehicle: The benefit of electrochemical capacitor smoothing," IEEE Power Electronics Magazine, vol. 1, no. 1, pp. 12–24, Mar. 2014.

[51] J. Shin et al., "Design and implementation of shaped magnetic resonance based wireless power transfer system for roadway powered moving electric vehicles," IEEE Transactions on Industrial Electronics, vol. 61, no. 3, pp. 1179–1192, Mar. 2014.

[52] B.-M. Song, R. Kratz, and S. Gurol, "Contactless inductive power pickup system for Maglev applications," the 37th IEEE IAS Annual Meeting, Pittsburgh, PA, Oct. 13–18, 2002, vol. 3, pp. 1586–1591.

[53] W. Y. Lee et al., "Finite-width magnetic mirror models of mono and dual coils for wireless electric vehicles," IEEE Transactions on Power Electronics, vol. 28, no. 3, pp. 1413–1428, Mar. 2013.

[54] J. Huh, S. W. Lee, W. Y. Lee, G. H. Cho, and C. T. Rim, "Narrow-width inductive power transfer system for online electrical vehicles," IEEE Transactions on Power Electronics, vol. 26, no. 12, pp. 3666–3679, Dec. 2011.

[55] S. Y. Choi, S. Y. Jeong, B. W. Gu, G. C. Lim, and C. T. Rim, "Ultraslim S-type power supply rails for roadway-powered electric vehicles," IEEE Transactions on Power Electronics, vol. 30, no. 11, pp. 6456–6468, Nov. 2015.

[56] Z. Wang, S. Cui, S. Han, K. Song, C. Zhu, M. I. Matveevich and O. S. Yurievich, "A Novel Magnetic Coupling Mechanism for Dynamic Wireless Charging System for Electric Vehicles", IEEE Transactions on Vehicular Technology, vol. 67, no. 1, pp. 124-133, 2018.

[57] J. Zhao, T. Cai, S. Duan, H. Feng, C. Chen, and X. Zhang, "A General Design Method of Primary Compensation Network for Dynamic WPT System Maintaining Stable Transmission Power," IEEE Transactions on Power Electronics, vol. 31, no. 12, pp. 8343-8358, Dec. 2016.

[58] H. Feng, T. Cai, S. Duan, J. Zhao, X. Zhang, and C. Chen, "An LCC-compensated resonant converter optimized for robust reaction to large coupling variation in dynamic wireless power transfer," IEEE Transactions on Industrial Electronics, vol. 63, no. 10, pp. 6591–6601, Oct. 2016.

[59] H. Feng, T. Cai, S. Duan, X. Zhang, H. Hu, and J. Niu, "A dual-side-detuned series–series compensated resonant converter for wide charging region in a wireless power transfer system," IEEE Transactions on Industrial Electronics, vol. 65, no. 3, pp. 2177–2188, Mar. 2018.

[60] Q. Zhu, Y. Guo, L. Wang, C. Liao, and F. Li, "Improving the misalignment tolerance of wireless charging system by optimizing the compensate capacitor," IEEE Transactions on Industrial Electronics, vol. 62, no. 8, pp. 4832–4836, Aug. 2015.

[61] Y. Yao, Y. Wang, X. Liu, Y. Pei, D. Xu and X. Liu, "Particle Swarm Optimization-Based Parameter Design Method for S/CLC-Compensated IPT Systems Featuring High Tolerance to Misalignment and Load Variation," IEEE Transactions on Power Electronics, vol. 34, no. 6, pp. 5268-5282, Jun. 2019.

[62] S. Li, L. Wang, Y. Guo, C. Tao and L. Ji, "Power Stabilization with Double Transmitting Coils and T-type Compensation Network for Dynamic Wireless Charging of EV", IEEE Journal of Emerging and Selected Topics in Power Electronics, vol. 8, no. 2, pp. 1801-1812, Jun. 2020.

[63] F. Lu, H. Zhang, H. Hofmann, and C. C. Mi, "A dynamic charging system with reduced output power pulsation for electric vehicles," IEEE Transactions on Industrial Electronics, vol. 63, no. 10, pp. 6580–6590, Oct. 2016.

[64] H. Li, Y. Liu, K. Zhou, Z. He, W. Li, R. Mai, "Uniform Power IPT System with Three-Phase Transmitter and Bipolar Receiver for Dynamic Charging," IEEE Transactions on Power Electronics, vol. 34, no. 3, pp. 2013–2017, 2019.

[65] C.-Y. Huang, J. E. James, and G. A. Covic, "Design considerations for variable coupling lumped coil systems," IEEE Transactions on Power Electronics, vol. 30, no. 2, pp. 680–689, Feb. 2015.

[66] M. Kim, D.-M. Joo, and B. K. Lee, "Design and control of inductively power transfer system for electric vehicles considering wide variation of output voltage and coupling coefficient," IEEE Transactions on Power Electronics, vol. 34, no. 2, pp. 1197–1208, Feb. 2019.

[67] J. M. Miller, P. T. Jones, J. Li, and O. C. Onar, "ORNL experience and challenges facing dynamic wireless power charging of EV's," IEEE Circuits and Systems Magazine, vol. 15, no. 2, pp. 40-53, Second-quarter 2015.

[68] J. Kim, B. Lee, J. Lee, S. Lee, C. Park, S. Jung, S. Lee, K. Yi, and J. Baek, "Development of 1MW Inductive Power Transfer System for a High Speed Train," IEEE Transactions on Industrial Electronics, vol. 62, no. 10, pp. 6242–6250, Oct. 2015.

[69] Available online at: http://primove.bombardier.com/products/charging.html

[70] Available online at: http://www.conductix.com

[70] Y. Li, R. Mai, L. Lu, and Z. He, "Active and reactive currents decomposition based control of angle and magnitude of current for a parallel multi-inverter IPT system," Transactions on Power Electronics, vol. 32, no. 2, pp. 1602–1614, Feb. 2017.

[71] Y. Li, R. Mai, L. Lu, T. Lin, Y. Liu and Z. He, "Analysis and Transmitter Currents Decomposition Based Control for Multiple Overlapped Transmitters Based WPT Systems Considering Cross Couplings," Transactions on Power Electronics, vol. 33, no. 2, pp. 1829 - 1842, Feb. 2018.

[72] J. G. Bolger, "Urban electric transportation systems: The role of magnetic power transfer Proceedings of WESCON '94, Anaheim, CA, Sep. 1994, pp. 41–45.

[73] California PATH Program, "Roadway powered electric vehicle project: Track construction and testing program, phase 3D," California Partner for Advanced Transportation Technology (PATH), USA, California PATH Res. Rep., Mar. 1994.

[74] C. T. Rim, "Design of Wireless Electric Vehicles Dynamic & Stationary Charging Technologies", 2016 IEEE 8th International Power Electronics and Motion Control Conference (IPEMC-ECCE Asia), Hefei, May 2016.

[75] C. Zheng et al., "High efficiency contactless power transfer system for electric vehicle battery charging application," IEEE Journal of Emerging and Selected Topics in Power Electronics, vol. 3, no. 1, pp. 65–74, Mar. 2015.

[76] "ICNIRP guidelines for limiting exposure to time-varying electric, magnetic and electromagnetic fields (1 Hz to 100 kHz)," Health Phys., vol. 99, pp. 818–836, 2010.

[77] S. Y. Choi, B. W. Gu, S. W. Lee, W. Y. Lee, J. Huh, and C. T. Rim, "Generalized active EMF cancel methods for wireless electric vehicles," Transactions on Power Electronics, vol. 29, no. 11, pp. 5770–5783, Nov. 2014.

[78] S. Cui, Z. Wang, S. Han, C. Zhu and C. C. Chan, "Analysis and Design of Multiphase Receiver with Reduction of Output Fluctuation for EV Dynamic Wireless Charging System Transactions on Power Electronics, vol. 34, no. 5, pp. 4112–4124, May. 2019.

[79] C. Park, S. Lee, S. Jeong, G.-H. Cho, and C. Rim, "Uniform power I-type inductive power transfer system with DQ-power supply rails for on-line electric vehicles Transactions on Power Electronics, vol. 30, no. 11, pp. 6446– 6455, Nov. 2015.

[80] K. Aditya and S. S. Williamson, "Design guidelines to avoid bifurcation in a series-series compensated inductive power transfer system," IEEE Transactions on Industrial Electronics, vol. 66, no. 5, pp. 3973-3982, Jul. 2018.

[81] "Innovation at the University of Auckland: Wireless power". Available online at:
https://www.youtube.com/watch?v=G1q1HZLQ528

CHAPTER 3

The proposed multiphase WDC system

This chapter presents the proposed multiphase EVs Wireless Dynamic Charging aiming to simultaneously achieve the constant and high output power level. The concept of the multiphase WDC system is analysed in detail. Starting from the motivation of the proposed system in Section 3.1, where the disadvantages of the single phase WDC system are highlighted. Next, the overall system configuration is presented in Section 3.2. Detailed design of the improved layout for multiple transmitters is given in Section 3.3. To minimize the length of coupler wires, Section 3.4 presents and compares two proposed winding methods. Finally, the conditions of transmitters' currents for achieving constant output power is provided in Section 3.5.

3.1 Motivation of the proposed method

As highlighted in Section 2.4, there are some technical challenges in implementing WDC that need to be addressed; therefore, the design of WDC should aim to:

(1) Deliver a constant output power to each individual vehicle.
(2) Provide high output power level to one or multiple vehicles simultaneously.
(3) Minimize the implementation cost and system complexity.
(4) Achieve high efficiency and low stray fields level.

While not all above objectives are easy to achieve, this thesis attempts to focus on the transmitter design, which plays an essential role in the WDC system.

As highlighted in the literature section, there are pros and cons with regards to using either long-track or short-track transmitter, which can be compromised through a hybrid configuration. In this work, the hybrid configuration is utilized. The length of each transmitter module of the hybrid configuration is selected as similar as the vehicle's length (i.e. 240 cm in this work). This results in reducing the number of inverters and the associated compensation

tanks as compared to the short-track transmitter type. Moreover, when compared to the long-track type, then the stray fields level can be reduced significantly as the transmitter module will be inactive if it is not in use.

To further reduce the cost and stray fields level, then the transmitter width should be as narrow as possible. Chapter 5 will point out how the efficiency and cost are in the trade-off relationship against the transmitter width. Moreover, the transmitter structure with the alternating magnetic polarity for adjacent poles is adopted to minimize the stray fields level surrounding.

To address the most serious problems of the conventional single-phase WDC system, the concept of the multiphase transmitters is proposed in this Thesis. Utilizing multiple windings in primary side, that guarantees a homogeneous mutual magnetic flux for the receiver along the driving direction. This results in a constant induced voltage across the receiver and hence constant output power to charge the EV battery. High output power is realised by using multiple transmitter windings which have been arranged in a novel winding method. The structure layout of the proposed WDC, including ferrite cores, windings and resonant tanks is presented. Furthermore, a theoretical analysis is conducted to determine conditions of each winding's current phase and amplitude for achieving constant output power. One of the issues of the multiphase transmitter system is that system performances can be affected by the crossing mutual inductances between transmitter's windings. They increase the losses in primary circuit and reduces efficiency. To compensate for these negative effects, a small capacitor is added in series with each transmitter coil.

Efficiency in a WDC system highly depends on the coupling factor between transmitters and receiver. Therefore, the parametric-analysis using Maxwell 3D simulation for both, transmitter and receiver is carried out to achieve the highest coupling factor by using minimum ferrite material. The tolerance of couplers against misalignment condition is also considered.

Communications between primary and secondary side are often required to control the vehicle's battery in the EV's wireless stationary charging. However, this may not be straightforward in WDC systems. Therefore, in this work the parameters at the primary side (e.g. transmitter current, operating frequency, etc.) are fixed and an on-board DC/DC regulator is assumed to regulate the voltage and current of the battery.

To summarise, the work in this Thesis attained a constant and high output power for the first time by proposing multiphase transmitter system. The transmitter constitutes of multiple windings and multiple magnetic poles with different polarities. It should be noted that the

proposed system retains the same features of [1-3], but it delivers higher and constant power. A multiphase inverter is considered to produce the required currents (i.e. amplitude and phase) for each transmitter's winding. Modified primary LCC compensation circuit is proposed to compensate for the crossing coupling between transmitter windings in which value of the series capacitor is modified as compared to the one in the original topology [7]. A generalized multiphase system is presented; however, the number of phases is selected based on the required output power. Maxwell 3D simulations is carried out to design and optimize the magnetic components for attaining the highest value of coupling factor with a minimum ferrite core under various misalignment conditions. The proposed concept is validated through an illustrative example based on a three-phase system. A scale down laboratory prototype of 3-kW is developed to experimentally verify the feasibility and effectiveness of the proposed system. Furthermore, in order to show the superiority of the proposed system, a comparison with similar systems [1-3], [4-5] is also carried out.

3.2 The proposed circuit configuration

Fig. 3.1 illustrates the proposed multiple transmitters aiming to achieve constant output power for an EV's dynamic charging system. The primary side consists of n transmitters, L_i $(i = 1, 2, ..., n)$ energizing one receiver coil, L_s. As these transmitters are physically placed closed to each other, crossing couplings between them naturally exist as depicted in Fig. 3.2. The mutual inductances between transmitter L_i and the receiver is denoted by M_{is} $(i = 1, 2, ..., n)$. Each transmitter is driven by a constant current source regardless of load and coupling coefficient conditions. Detailed structures of transmitter and receiver are described in the next Section. A multi-phase DC/AC inverter is adopted at the primary side to produce a high frequency AC voltage for each transmitter. The inverter consists of n legs, namely leg *1*, leg *2*,..., leg *i*,…, leg *n*. Please note that the number of inverter's legs is equal to the number of transmitter windings. Each leg has two switches that operate complementarily with a small deadtime to ensure save commutation without short circuiting the DC supply. The operating waveforms of the multi-phase inverter is depicted in Fig. 3.2 which includes the gate signals of the semiconductor switches and the resultant inverter's output voltages. The phase-shift between two adjacent legs' output voltages (i.e. $V_{(i-1)i}$ and $V_{i(i+1)}$) is set at $2\pi/n$. The switching frequency of the inverter is chosen to be 85 kHz according to SAE J2954 standard [6] and the period of gate signal is *T = 1/f*.

A modified LCC resonant circuit based on [7], which consists of L_{ia}, C_{ia} and $C_{ib}(i = 1,2, \ldots, n)$, is used in the primary side. In order to produce constant transmitter currents, I_i $(i = 1,2, \ldots, n)$, the resonance between L_{ia} and C_{ia} is set at the switching frequency of the inverter. The series capacitors $C_{ib}(i = 1,2, \ldots, n)$ are used here for two purposes: (1) to resonate with the transmitter's inductance L_i and (2) to suppress the induced voltages caused by the crossing couplings from other transmitters. Please note that the phase of the transmitter current I_i is always leading 90 degrees as compared to the phase of the inverter's output voltage $V_{i(i+1)}$ because of the resonance of LCC tank. At the secondary side, another LCC resonant tank is connected to the full-bridge rectifier to provide DC power to the output load. There should be another DC/DC regulator after the rectifier for battery charging purposes. However, for simplicity, only resistive load is used to investigate the feasibility of the proposed system. The proposed layout of primary transmitters and conditions of currents I_i $(i = 1, 2, \ldots, n)$ are further detailed in the following subsections. It is worth noting that the configuration in Fig. 3.1 is only applicable with a minimum number of phases (n) of three. However, when n equals to 1 or 2, the primary inverter connection needs to be modified as shown in Fig. 3.3(a) and (b).
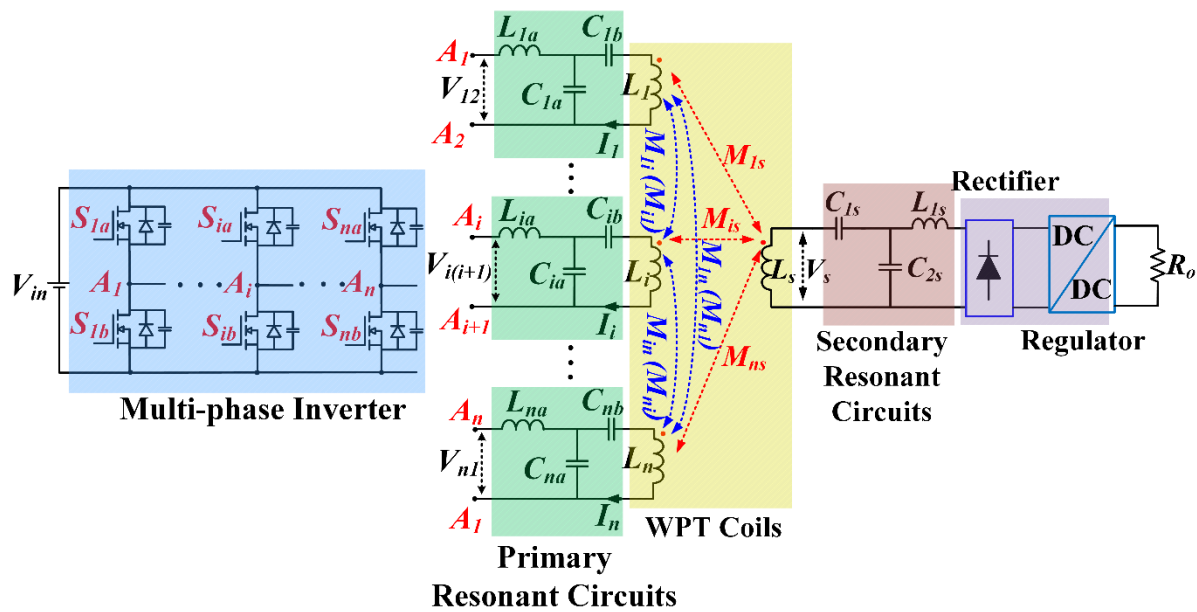
Fig. 3.1. The configuration of the proposed WDC circuit with multiple transmitter coils (n ≥ 3).
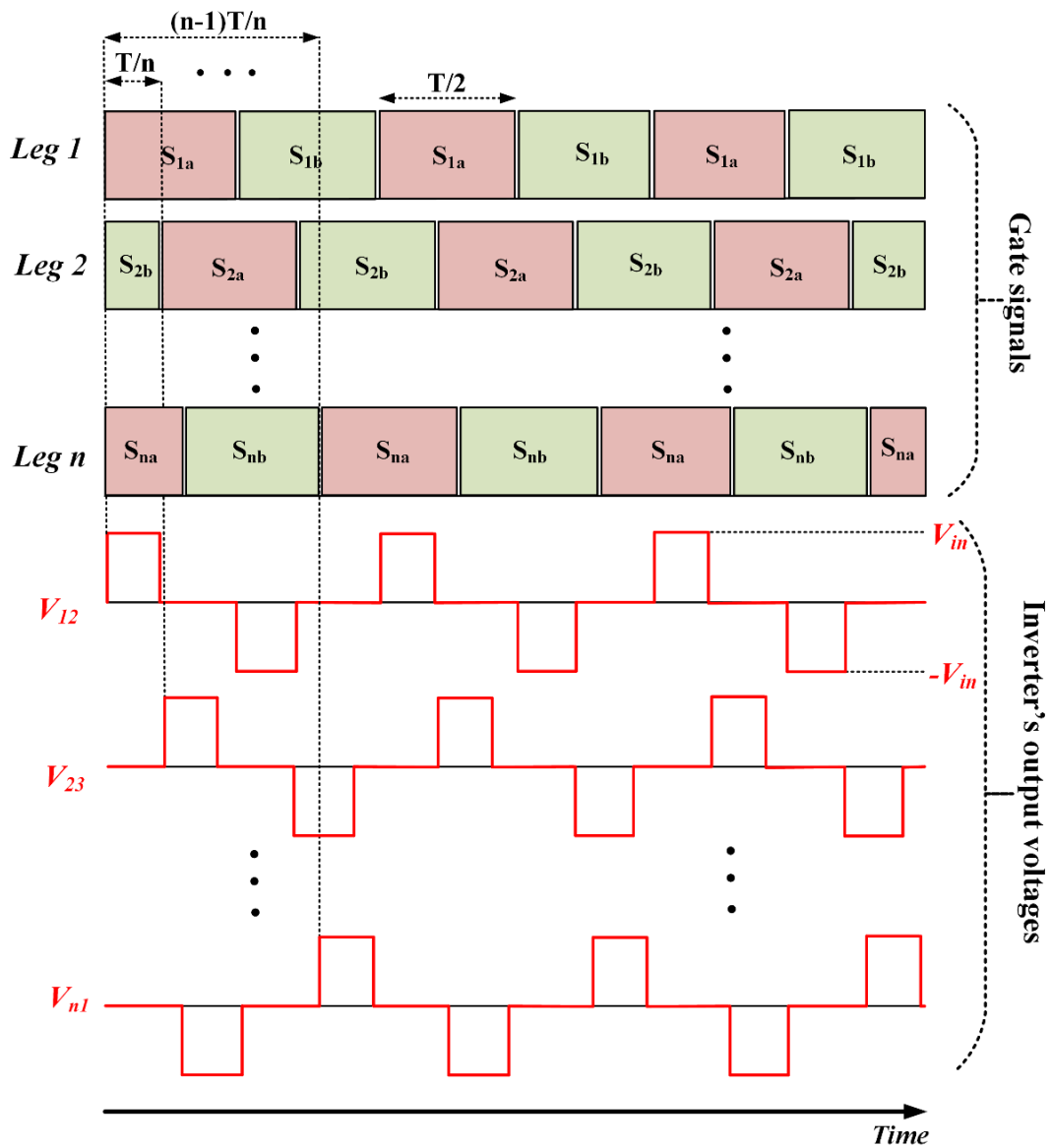
Fig. 3.2. The operating waveforms of the multiphase inverter.
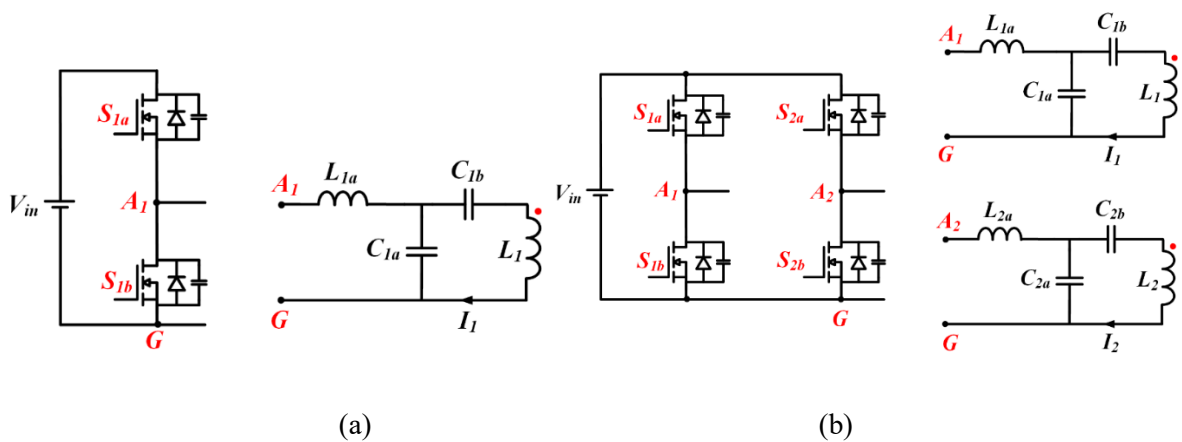
Fig. 3.3. Modification of inverter connection. (a) n = 1. (b) n = 2.

3.3 The layout of the proposed multiple transmitter

The derivation of the proposed system is inspired by the limitations of a single transmitter system. Fig. 3.4 illustrates WDC that consists of multiple alternating magnetic I-pole core, where the receiver is covering one magnetic pole. When the receiver is perfectly aligned with center of each magnetic pole, i.e. completely covers the winding loop, then the mutual inductance will reach its maximum value. On the other hand, the mutual inductance drops to zero when the receiver centers at the middle point between each adjacent pole, where the magnetic fluxes cancel each other (i.e. same magnitude but opposite directions), resulting in no induced voltage. Therefore, as the receiver (i.e. EV) moves along the transmitter, spatial periodic induced voltage and power (P_o) is obtained, which is proportional with mutual inductance value. Consequently, as the vehicle travels along, the battery will not receive any power at the points of zero-mutual-inductance (i.e. *pulsating power*). The spatial distribution of mutual inductance between a single transmitter and receiver $M_{1s}(x)$ can be approximately expressed by Eq. (3.1), where M_o and l_o are the maximum mutual inductance and the length of two adjacent poles, respectively. The mutual inductance $M_{1s}(x)$ for single transmitter system are portrayed in Fig 3.5 in which $M_{1s}(x)$ is under sinusoidal form.

 It is noted that Eq (3.1) is only valid under no lateral misalignment. The variation of the coupling coefficient k caused by the lateral misalignment is also important, not just the peak value M_o. This generally gives challenges to the whole design process where suitable control needs to be utilized.

$$M_{1s}(x) = M_o \sin\left(\frac{2\pi x}{l_o}\right) \qquad (3.1)$$
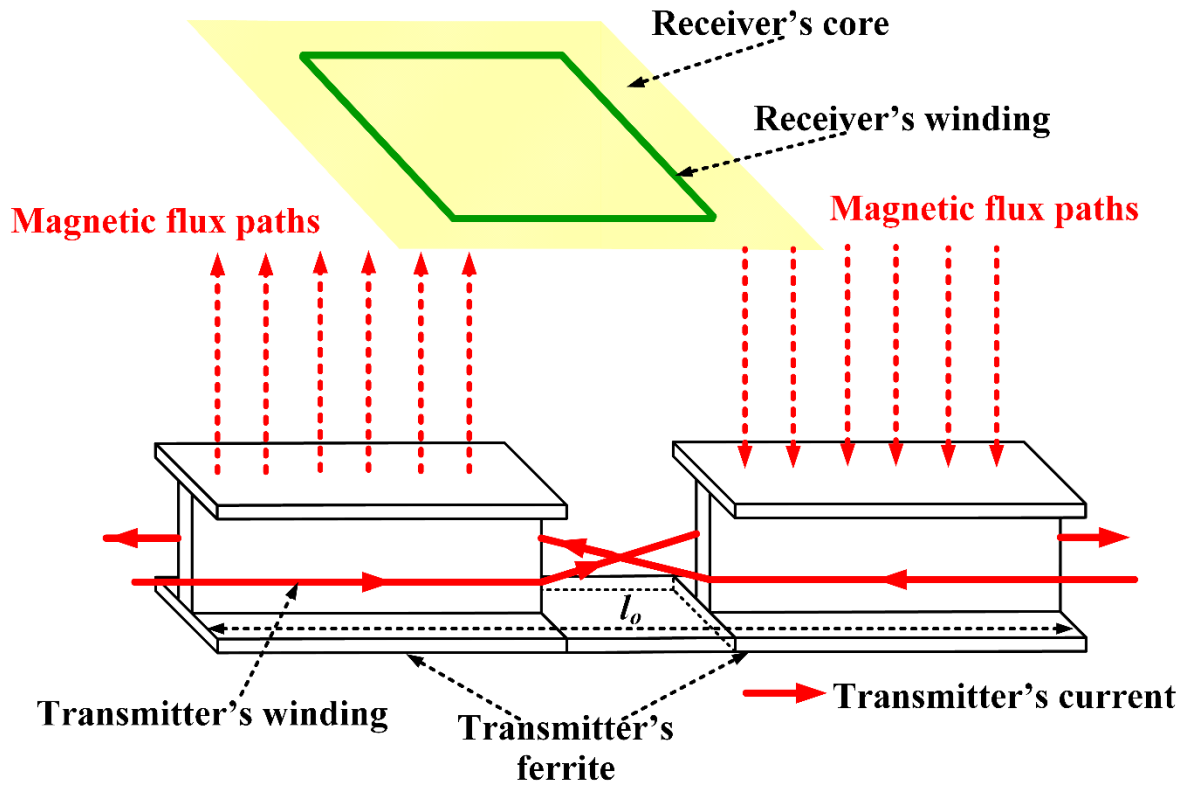
Fig. 3.4. Side view of the single transmitter system when the receiver positions in the lowest mutual inductance point.
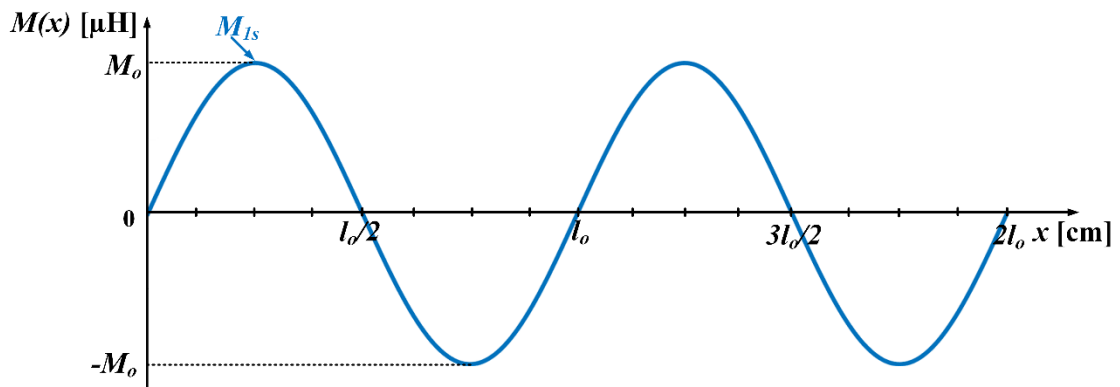
Fig. 3.5. Spatial distribution of mutual inductance of the single transmitter system.

In order to solve abovementioned problem, additional transmitters can be added into the original system to nullify the zero mutual inductance points. The number of additional transmitters is determined by the output power requirement (i.e. volt-ampere capability) of the system components such as power switches, transmitter coils and resonant capacitors.

However, increasing the number of transmitters results in higher implementation cost, therefore the selection of number of transmitters is a trade-off between cost and efficiency. To attain a constant output power, it is essential to ensure that all mutual inductances $M_{is}(x)$ $(i = 2,3, \ldots, n)$ are evenly distributed over the transmitter length to avoid any zero mutual inductance points. It refers that between any two adjacent null points of $M_{1s}(x)$, there are new $(n-1)$ null points from added $M_{is}(x)$ $(i = 2,3, \ldots, n)$. In other words, the phase difference between any two adjacent mutual inductances $M_{is}(x)$ and $M_{(i+1)s}(x)$ should be equal each other as illustrated in Fig. 3.6. The phase-shift difference between any two adjacent mutual inductance curves $M_{is}(x)$ and $M_{(i+1)s}(x)$ is set at $2\pi/n$. It is also avoided to add new null points of all added $M_{is}(x)$ $(i = 2,3, \ldots, n)$ into the same positions with the existing one of $M_{1s}(x)$, otherwise, added $M_{is}(x)$ does not contribute to compensate the null-point of $M_{1s}(x)$. In other words, $M_{is}(x)$ $(i = 2,3, \ldots, n)$ should be not identical with $M_{1s}(x)$. Equation (3.2) expresses all (n) mutual inductances (i.e. $M_{is}(x)$ $(i = 1,2, \ldots, n)$) including the original $M_{1s}(x)$. It is worth mentioning that $M_{(i+1)s}(x)$ can be either leading or lagging with a phase angle of $2\pi/n$ with respect to $M_{is}(x)$. Although in Fig. 3.6, $M_{(i+1)s}(x)$ is lagging $M_{is}(x)$, either way (lagging or leading) will result in compensating the zero mutual inductance points. The way of leading or lagging depends on the direction of vehicle. Equation (3.2) satisfies with any number of phases. There is only one exception if $n = 2$ where the phase-shift between two adjacent phases is $\pi/2$ instead of π. This is to guarantee that the null points of $M_{1s}(x)$ and $M_{2s}(x)$ do not overlap.

$$
\begin{cases}
M_{1s}(x) = M_o \sin\left(\dfrac{2\pi x}{l_o}\right) \\[2ex]
M_{2s}(x) = M_o \sin\left(\dfrac{2\pi x}{l_o} - \dfrac{2\pi}{n}\right) \\[2ex]
\vdots \\[1ex]
M_{is}(x) = M_o \sin\left[\dfrac{2\pi x}{l_o} - (i-1)\dfrac{2\pi}{n}\right] \\[2ex]
\vdots \\[1ex]
M_{ns}(x) = M_o \sin\left[\dfrac{2\pi x}{l_o} - (n-1)\dfrac{2\pi}{n}\right]
\end{cases}
\tag{3.2}
$$
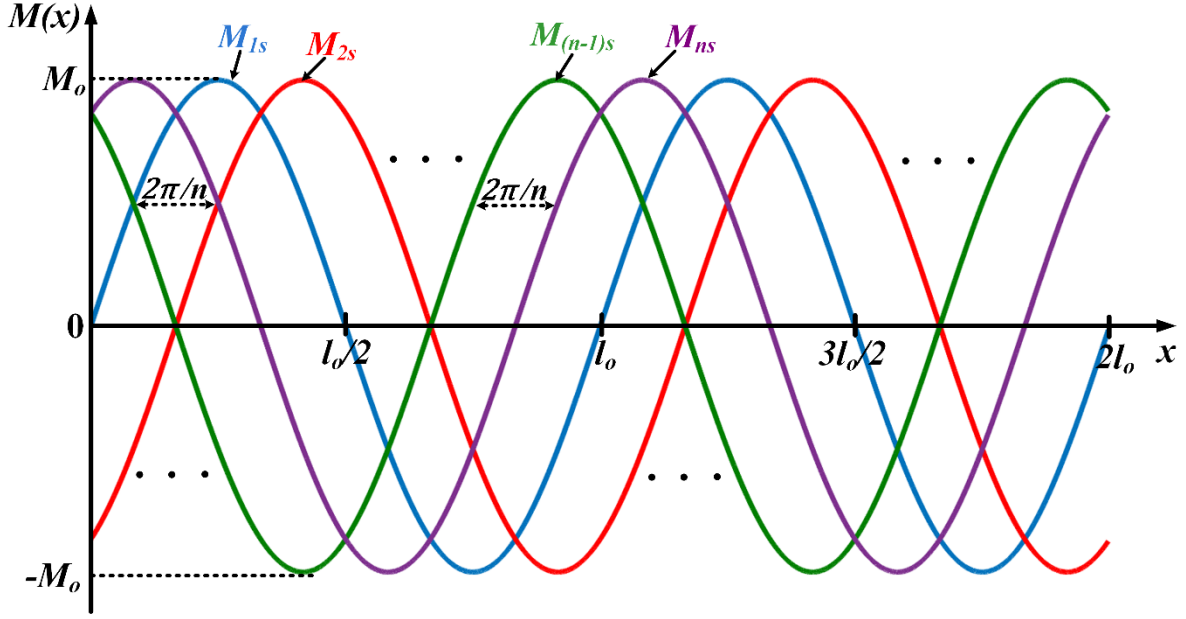
Fig. 3.6. Expected spatial distribution of mutual inductances for the proposed multiple transmitters.

In order to obtain evenly distributed $M_{is}(x)$ as shown in Eq. (3.2), the proposed transmitter of n windings are structured as depicted in Fig. 3.8. The proposed transmitter system is based on the I-type ferrite shape as presented in [1]. As discussed above, $(n-1)$ additional mutual inductances are evenly distributed over the length of l_o. This could be illustrated that between any two maximum points of $M_{1s}(x)$ (positive values), there are $(n-1)$ maximum points of additional mutual inductances (positive points). It can be imagined that each original core of the conventional single transmitter (i.e. Fig. 3.7) is divided into n small cores (Fig. 3.8a) so that the additional windings can be included on. These small cores dimensions are adjustable and determined by the requirements of coupling factor and tolerance to misalignment. It is worth noting that the maximum point of any two adjacent mutual inductances (M_o) occur at $l_o/2n$ (i.e., both, positive and negative).

In addition, as the multiple transmitter windings of the proposed system are placed close to each other, there will be crossing mutual inductances between them. This causes higher current through the inverter switches as well as the resonant tank components of L_{ia} and C_{ia} , which have destructive effects on the inverter switches [8]. To alleviate this effect, a small capacitor is connected in series with each transmitter to cancel the induced voltages caused by the crossing coupling (as discussed in Chapter 4).
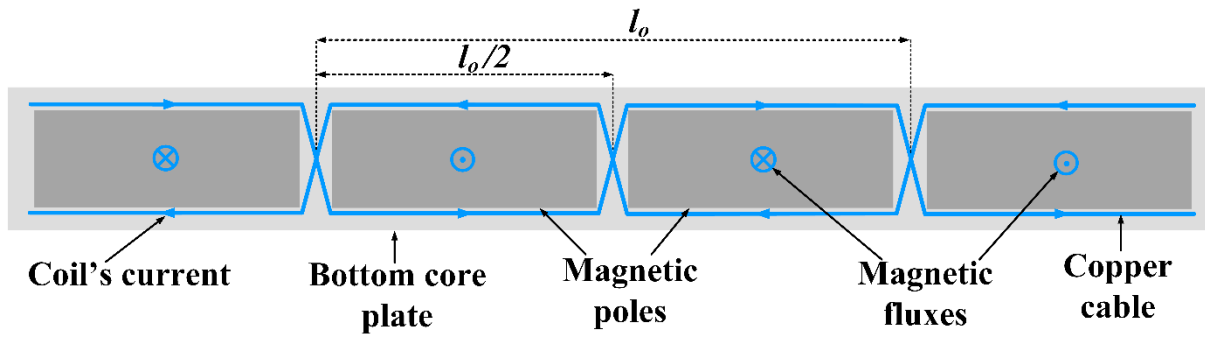
Fig. 3.7. Layout configuration of the conventional single transmitter [1].
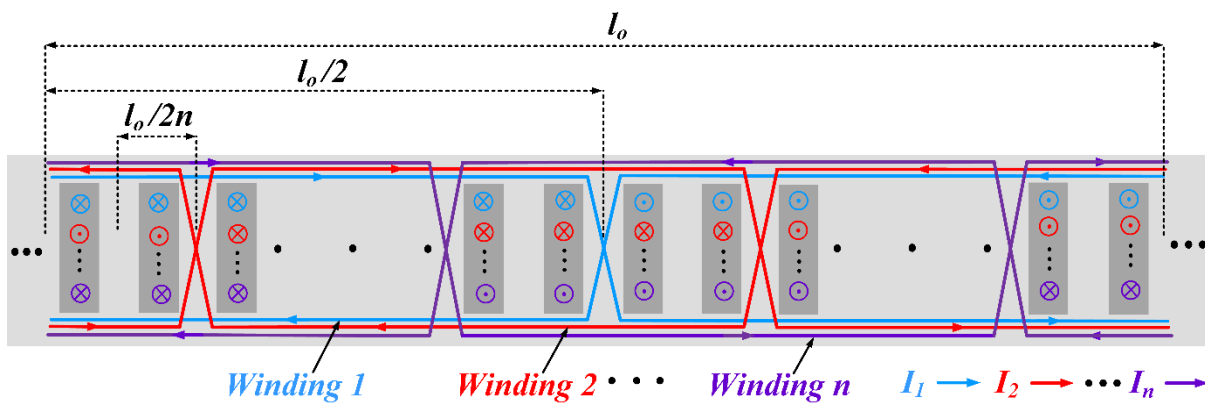
(a)
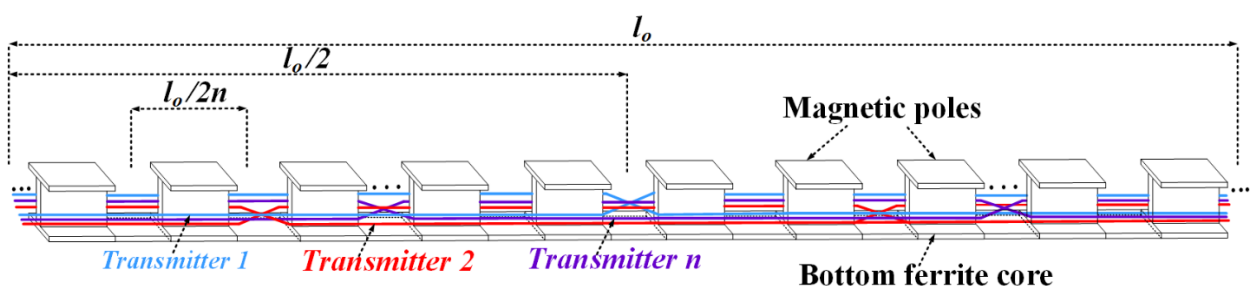
(b)

Fig. 3.8. Layout configuration of the proposed multiple transmitters. (a) Top view. (b) Side view.

3.4 Winding layout of the transmitter

In order to reduce the implementation cost of the system as well as the associated losses, the transmitter can be configured in different layouts to reduce the required copper. As an example, this section presents two different winding layout methods for the proposed multiphase transmitters. The first winding method shown in Fig. 3.9 is to wind the copper wire from the first to the end of the pole segments while the second method is to wind the copper wire around individual pole segments as depicted in Fig. 3.10. Although the proposed transmitter system in this thesis includes three wingdings, however, for simplicity only one winding is illustrated in this section. The total length would be simply 3 times. The pole's length in this Section is of $\left(\frac{l_o}{2} - d_p\right)$ which consists of three smaller poles.
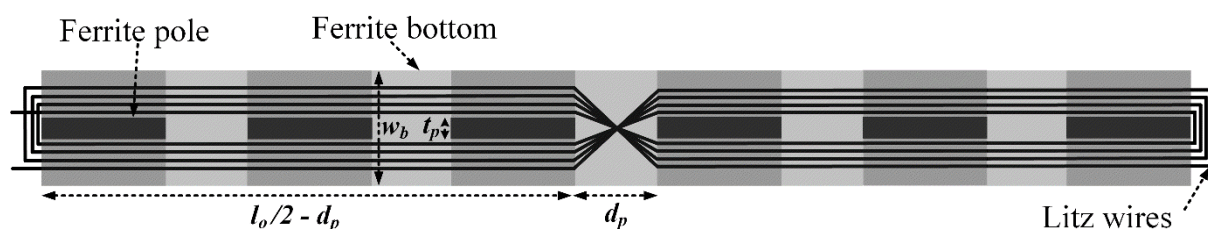
Fig. 3.9. Configuration of method 1 winding.
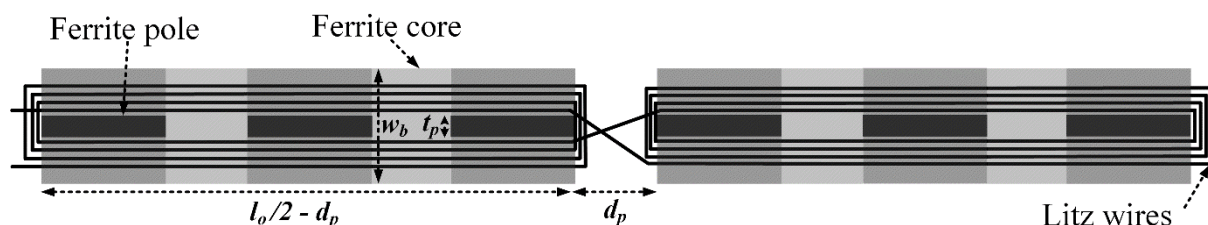
Fig. 3.10. Configuration of method 2 winding.

For the first and second winding methods, the total length of copper wire l_1 and l_2 is approximately given in (3.3) and (3.4) respectively:

$$l_1 \approx \left(l_o - 2d_p\right)N_{tu}N_{po} + 2N_{tu}\left(N_{po} - 1\right)\sqrt{d_p^2 + \frac{w_p^2}{4}} \tag{3.3}$$

$$l_2 \approx \left(l_o - 2d_p\right)N_{tu}N_{po} + t_p(N_{tu} - 1)N_{po} + 2\left(N_{po} - 1\right)\sqrt{d_p^2 + \frac{w_p^2}{4}} \tag{3.4}$$

where N_{po} is number of poles and N_{tu} is number of turns.

Therefore, the required copper for the proposed transmitter is calculated using (3.3) and (3.4) and presented in Fig. 3.11 and Fig. 3.12, respectively. Even though the difference is not considerable if N_{po} and N_{tu} are of small values, however the second methods saves up to 10% as compared to the first arrangement when $N_{po} = N_{tu} = 8$. Hence, second method has be chosen to implement the proposed transmitter.
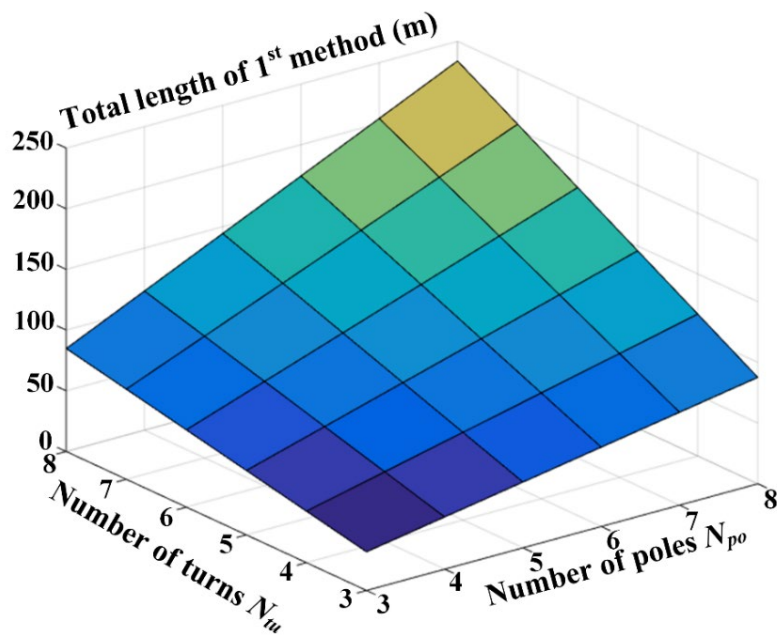
Fig. 3.11. The total copper wire length in the first winding method.
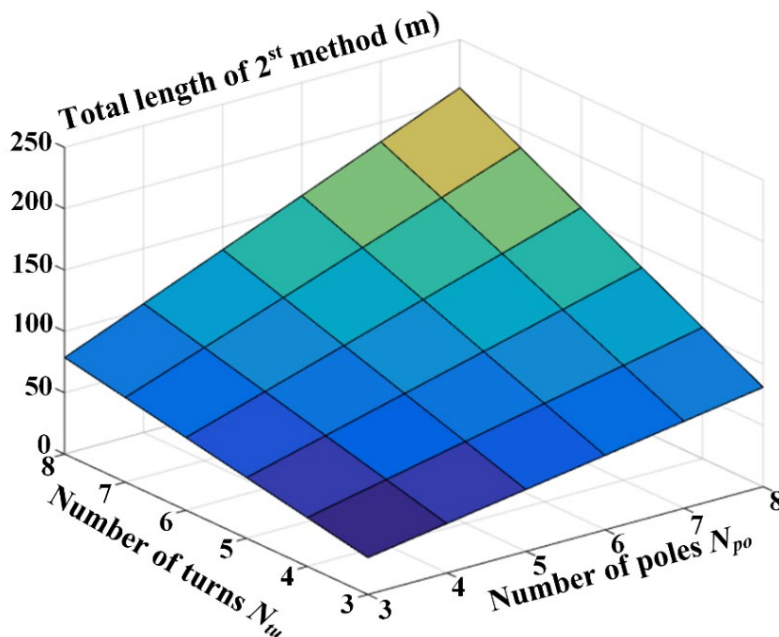
Fig. 3.12. The total copper wire length in the second winding method.

3.5 Relationship between transmitters' currents and constant output power

This section analyses the conditions of transmitter's currents in order to achieve a constant output power. Firstly, the open-circuit induced voltage V_s on the receiver can be expressed by:

$$V_s = j\omega \sum_{i=1}^{n} M_{is}(x)I_i \tag{3.5}$$

where I_i is the current through i^{th} transmitter and $M_{is}(x)$ is the mutual inductance between i^{th} transmitter and the receiver.

Assuming the inverter produces equal voltages (i.e. with phase shift of $\frac{2\pi}{n}$) across each resonant tank, therefore, the currents through each transmitter windings can be expressed by:

$$\begin{cases} I_1 = I_o e^{j0} \\ I_2 = I_o e^{j\frac{-2\pi}{n}} \\ \vdots \\ I_i = I_o e^{j(i-1)\frac{-2\pi}{n}} \\ \vdots \\ I_n = I_o e^{j(n-1)\frac{-2\pi}{n}} \end{cases} \tag{3.6}$$

Consequently, V_s can be further expressed as follows:

$$|V_s| = \omega \left| \sum_{i=1}^{n} M_o \sin\left(\frac{2\pi x}{l_o} - (i-1)\frac{2\pi}{n}\right) I_o \, e^{j(i-1)\left(\frac{-2\pi}{n}\right)} \right| \tag{3.7}$$

$$|V_s| = \omega M_o I_o \left| \sum_{i=1}^{n} \left\{ \frac{e^{j\left[\frac{2\pi x}{l_o} - (i-1)\frac{2\pi}{n}\right]} - e^{-j\left[\frac{2\pi x}{l_o} - (i-1)\frac{2\pi}{n}\right]}}{2j} \right\} e^{j(i-1)\left(\frac{-2\pi}{n}\right)} \right|$$

$$|V_s| = \frac{\omega M_o I_o}{2} \left| \sum_{i=1}^{n} \left[e^{j\frac{2\pi x}{l_o} - j(i-1)\frac{4\pi}{n}} - e^{-j\frac{2\pi x}{l_o}} \right] \right| \tag{3.8}$$

$$|V_s| = \frac{\omega M_o I_o}{2} \left| e^{j\frac{2\pi x}{l_o}} \sum_{i=1}^{n} e^{-(i-1)\frac{4\pi}{n}} - e^{-j\frac{2\pi x}{l_o}} \right|$$

where:

$$\sum_{i=1}^{n} e^{-j(i-1)\frac{4\pi}{n}} = e^{0j} + e^{-j\frac{4\pi}{n}} + e^{-j\frac{8\pi}{n}} + e^{-j\frac{12\pi}{n}} + \cdots + e^{-j\frac{(n-1)4\pi}{n}}$$

(3.9)

$$= 1 + Z_1 + Z_2 + Z_3 + \cdots + Z_{n-1}$$

In which:
$$\begin{cases} Z_1 = e^{-j\frac{4\pi}{n}} \\ Z_2 = e^{-j\frac{8\pi}{n}} = Z_1^2 \\ Z_3 = e^{-j\frac{12\pi}{n}} = Z_1^3 \\ \vdots \\ Z_{n-1} = e^{-j\frac{(n-1)4\pi}{n}} = Z_1^{n-1} \end{cases}$$

Therefore, the sum in (3.8) is rewritten as (3.10) with attenuation that $Z_1^n =$

$$e^{-j\frac{4\pi}{n}n} = \cos(-4\pi) + j\sin(-4\pi) = 1$$

$$\sum_{i=1}^{n} e^{-j(i-1)\frac{4\pi}{n}} = 1 + Z_1 + Z_2 + Z_3 + \cdots + Z_{n-1} = 1 + Z_1 + Z_1^2 + Z_1^3 + \cdots + Z_1^{n-1}$$

(3.10)

$$= \frac{1 - Z_1^n}{1 - Z_1} = 0$$

Letting $\left| e^{-j\frac{2\pi x}{l_o}} \right| = 1$, the final expression of $|V_s|$ is given as:

$$|V_s| = \frac{\omega M_o I_o}{2} \left| 0 - ne^{-j\frac{2\pi x}{l_o}} \right| = \frac{n\omega M_o I_o}{2} \left| e^{-j\frac{2\pi x}{l_o}} \right| = \frac{n\omega M_o I_o}{2}$$

(3.11)

At this point, the proposed system consisting of multiple transmitter windings can be equivalently simplified as only one transmitter coupled with receiver as showed in Fig. 3.13(b). In the simplified model, M can be seen as the equivalent mutual inductance between the primary and the secondary sides, which is defined as a half of multiplication between the number of transmitters n and amplitude of each mutual inductance M_o. It is also assumed that self-inductance of each transmitter is the same so that the equivalent transmitter has its inductance value of L_p, i.e. $L_p = L_1 = L_2 = \cdots = L_n$. Finally, the equivalent transmitter current amplitude I_p is equal to I_o so that V_s can be expressed by Eq. (3.11). It is worth noting that constant $|V_s|$ can be attained with any phase value of I_p. The equivalent model helps to simplify required calculation and design procedure. According to (3.11), by adopting the transmitter's layout with expression of mutual inductances in (3.2) and condition for transmitter's current is shown in (3.6), then the induced voltage is constant regardless of

receiver's position. Higher value of $|V_s|$ and corresponding power are realised with increase in the number of phases, n.
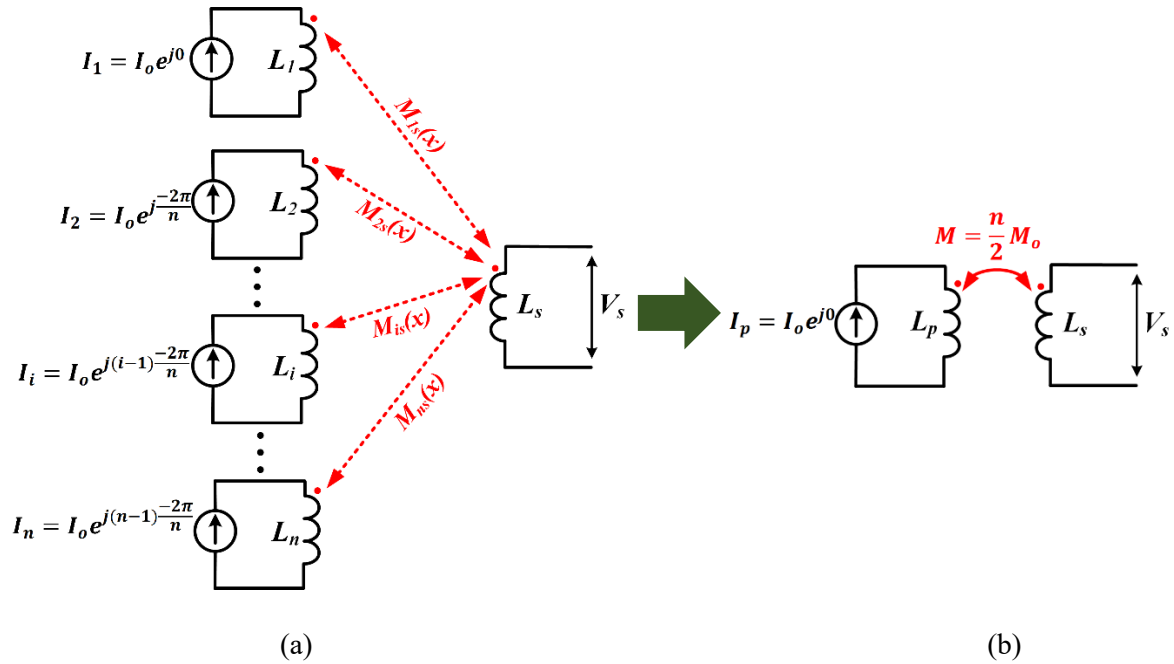
Fig. 3.13. (a) Equivalent model of the multiphase transmitter system. (b) Simplified form of the model in Fig. 3.13(a).

3.6 Chapter summary

 This chapter firstly gave the motivation of =this work, in which all main disadvantages of the conventional WDC systems have been analysed. Based on that, the proposed WDC system has presented to overcome all mentioned drawbacks of the conventional WDC systems.

 The proposed multiphase WDC system consists of multi-winding with alternative ferrite poles in primary side to effectively produce a constant coupling magnetic flux between transmitters and receiver. The detailed layout for transmitters along with the conditions of transmitters' currents are analysed and discussed in this Chapter. The two proposed winding methods are also given to minimize the total length of copper wire for the transmitters. The following are the main benefits of the proposed WDC system:

(1) Achieving constant output power with a simple control requirement.

(2) Less number of inverters compared to [5].

(3) Elimination of measurement of mutual inductance and load impedance as well as communication between the grid and vehicle side while the EV is in motion.

(4) Attainting higher output power (i.e. 2.25 higher for the three-phase case) for the same system parameters, e.g. mutual inductance, transmitter's current, switching frequency and receiver's dimension, compared to the single-phase system.

(5) Unlike the previous systems [1], [2] and [5], the proposed approach can be easily extended to multiple EV charging without any changes to the primary side control. This will be more suitable for real scenarios.

3.7 References

[1] J. Huh, S. W. Lee, W. Y. Lee, G. H. Cho, and C. T. Rim, "Narrow-width inductive power transfer system for online electrical vehicles," IEEE Transactions on Power Electronics, vol. 26, no. 12, pp. 3666–3679, Dec. 2011.

[2] S. Y. Choi, S. Y. Jeong, B. W. Gu, G. C. Lim, and C. T. Rim, "Ultraslim S-type power supply rails for roadway-powered electric vehicles," IEEE Transactions on Power Electronics, vol. 30, no. 11, pp. 6456–6468, Nov. 2015.

[3] Zhiyuan Wang, Shumei Cui, Shouliang Han, Kai Song, Chunbo Zhu, Milyaev Igor Matveevich, Ostanin Sergei Yurievich, "A Novel Magnetic Coupling Mechanism for Dynamic Wireless Charging System for Electric Vehicles", IEEE Transactions on Vehicular Technology, vol. 67, no. 1, pp. 124-133, 2018.

[4] S. Cui, Z. Wang, S. Han, C. Zhu and C. C. Chan, "Analysis and Design of Multiphase Receiver with Reduction of Output Fluctuation for EV Dynamic Wireless Charging System," IEEE Transactions on Power Electronics, vol. 34, no. 5, pp. 4112–4124, May. 2019.

[5] C. Park, S. Lee, S. Jeong, G.-H. Cho, and C. Rim, "Uniform power I-type inductive power transfer system with DQ-power supply rails for on-line electric vehicles," IEEE Transactions on Power Electronics, vol. 30, no. 11, pp. 6446– 6455, Nov. 2015.

[6] SAE International, "Wireless power transfer for light-duty plugin/electric vehicles and alignment methodology," 2017.

[7] S. Li, W. Li, J. Deng, T. D. Nguyen, and C. C. Mi, "A double-sided LCC compensation network and its tuning method for wireless power transfer," IEEE Transactions on Vehicular Technology, vol. 64, no. 6, pp. 2261–2273, Jun. 2015.

[8] M. L. G. Kissin, J. T. Boys, and G. A. Covic, "Interphase mutual inductance in poly-phase inductive power transfer systems," IEEE Transactions on Industrial Electronics, vol. 56, no. 7, pp. 2393–2400, Jul. 2009.

CHAPTER 4

Design consideration for the multiphase WDC system

4.1 Selection of the number of phases (*n* = 3)

The proposed multiphase dynamic charging system in Chapter 3 is illustrated by the design example of a three-phase system in this chapter. The selection of the number of phases (*n*) is a trade-off relationship. Higher number of phases results in higher efficiency and higher power capability. If the same amount of power is transferred, then the higher number of phases results in a lower current through each transmitter winding and, therefore the total conduction losses can be reduced. On the other hand, if the same amount of current is applied through each transmitter, the system with a higher number of phases will provide a higher amount of the induced receiver's voltage and hence, output power as a result (i.e. based on Eq. (3.11) in Chapter 3).

However, higher number of phases also brings in an increase in cost and complexity. The total cost is associated with the total number of components in the primary side, which include transmitter windings and resonant tanks. The design consideration is also made more complicated by the crossing mutual inductances between different transmitter windings. Considering this relationship, a three-phase transmitter system has been selected in this work. The aim of this chapter is to provide a detailed design procedure of the three-phase WDC system.

4.2 Circuit operation of the three-phase WDC system

The circuit configuration of the three-phase WDC system is shown in Fig. 4.1, in which a conventional three-phase inverter is adopted at the primary side. In the experiment, a 0.2-Ω resistance was measured for each transmitter coil. With the target output power of 3 kW and an RMS transmitter current of 14 A, this produces a total loss of 120 W. As such a small

percentage is caused by the coils' resistances, then their values are neglected in the analysis for simplicity.

Mutual inductances between transmitters L_1, L_2 and L_3 to the receiver L_s are defined as M_{1s}, M_{2s} and M_{3s}, respectively. The distributions of M_{1s}, M_{2s} and M_{3s} against the receiver's displacements are depicted in Fig. 4.2, in which their amplitudes are identical as M_o. The phase difference between two consecutive transmitter windings is set to $2\pi/3$. Therefore, mutual inductances equations can be expressed by:

$$\begin{cases} M_{1s}(x) = M_o \sin\left(\dfrac{2\pi x}{l_o}\right) \\ M_{2s}(x) = M_o \sin\left(\dfrac{2\pi x}{l_o} - \dfrac{2\pi}{3}\right) \\ M_{3s}(x) = M_o \sin\left(\dfrac{2\pi x}{l_o} - \dfrac{4\pi}{3}\right) \end{cases} \tag{4.1}$$
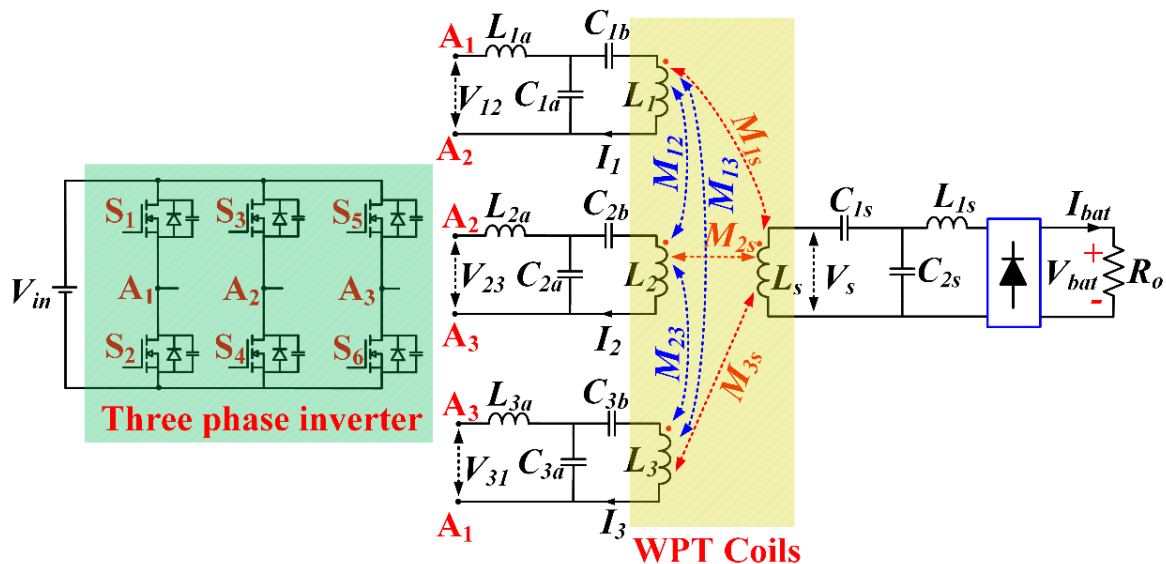
Fig. 4.1. Circuit configuration of the three-phase dynamic charging system.
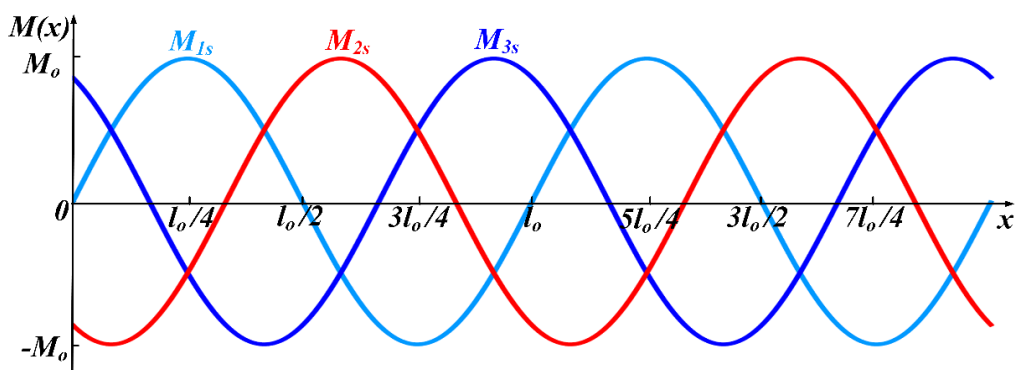
Fig. 4.2. Spatial distribution of mutual inductances of the three-phase transmitter system.

Firstly, the output voltages of a three-phase inverter can be depicted as:

$$\begin{cases} V_{12} = \dfrac{2\sqrt{3}}{\pi} V_{in} e^{j0} \\[2mm] V_{23} = \dfrac{2\sqrt{3}}{\pi} V_{in} e^{j\left(-\frac{2\pi}{3}\right)} \\[2mm] V_{31} = \dfrac{2\sqrt{3}}{\pi} V_{in} e^{j\left(-\frac{4\pi}{3}\right)} \end{cases} \tag{4.2}$$

As described in Chapter 3, the modified LCC resonant circuit is used in the primary side for each phase, which consists of L_{ia}, C_{ia} and C_{ib} $(i = 1,2,3)$. The resonance between L_{ia} and C_{ia} is set at the switching frequency of the inverter to achieve constant transmitter current, I_i $(i = 1,2,3)$. The series capacitors $C_{ib}(i = 1,2,3)$ are used here to resonate with the transmitter's inductance L_i and also to suppress the induced voltages caused by the crossing mutual inductances from other transmitters. The negative effects of crossing mutual inductances are critically analysed in this chapter. On the secondary side, another LCC resonant tank is connected to the full-bridge rectifier to provide DC power to the output load. There should be another DC/DC regulator after the rectifier for battery-charging purposes. For simplicity, only resistive load is used to investigate the feasibility of the proposed system.

The theoretical waveforms of the gate-drive signals and inverter output voltages (V_{12}, V_{23} and V_{31}) are illustrated in Fig. 4.3. The phase-shift between two consecutive inverters' output voltages is $2\pi/3$. As a result, the phase-shift between transmitter currents of two consecutive windings is also $2\pi/3$, which helps to achieve the constant induced voltage on the receiver side.
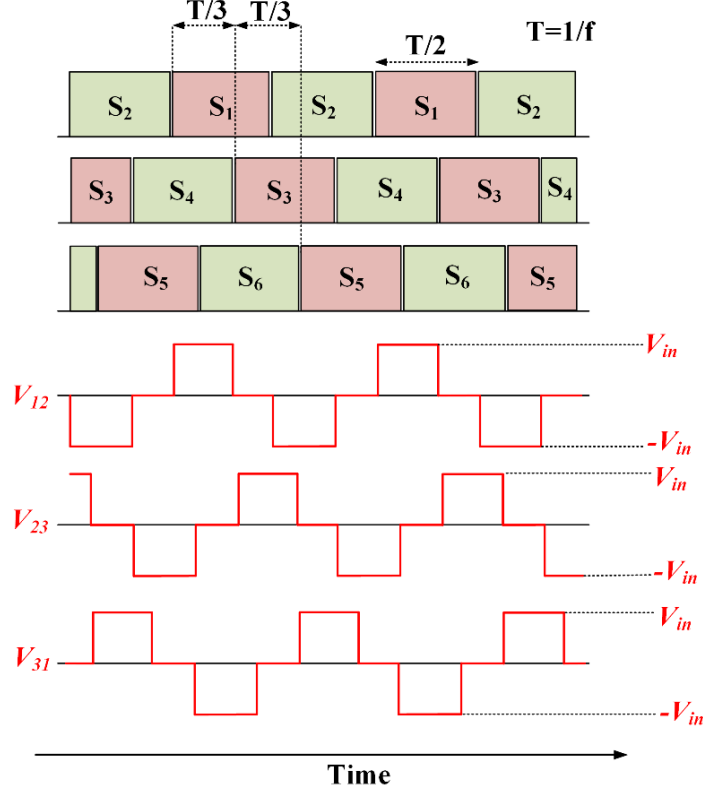
Fig. 4.3. Key operating waveforms of the three-phase inverter: gate signals and output voltages.

4.3 Design of resonant tanks

This section presents the design of resonant tanks in both primary and secondary sides, considering the crossing inductances between the primary windings. To simplify the control requirements of transmitter currents I_i ($i = 1 - 3$), a resonance of L_{ia} and C_{ia} ($i = 1,3$) is adopted at the angular frequency ω_o as shown in (4.3) to keep a constant amplitude of the transmitter's current. Therefore, I_i are expressed in (4.4).

$$\omega_o^2 = \frac{1}{L_{ia}C_{ia}} \quad (i = 1,3) \tag{4.3}$$

$$\begin{cases} I_1 = V_{12}\omega_o C_{1a} e^{j\left(\frac{-\pi}{2}\right)} = \frac{2\sqrt{3}}{\pi} V_{in}\omega_o C_{1a} e^{j\left(\frac{-\pi}{2}\right)} = I_o e^{j\left(\frac{-\pi}{2}\right)} \\[2mm] I_2 = V_{23}\omega_o C_{2a} e^{j\left(\frac{-\pi}{2}\right)} = \frac{2\sqrt{3}}{\pi} V_{in}\omega_o C_{2a} e^{j\left(\frac{-7\pi}{6}\right)} = I_o e^{j\left(\frac{-7\pi}{6}\right)} \\[2mm] I_3 = V_{31}\omega_o C_{3a} e^{j\left(\frac{-\pi}{2}\right)} = \frac{2\sqrt{3}}{\pi} V_{in}\omega_o C_{3a} e^{j\left(\frac{-11\pi}{6}\right)} = I_o e^{j\left(\frac{-11\pi}{6}\right)} \end{cases} \tag{4.4}$$

Fig. 4.4 presents the primary LCC tank considering magnetic interferences between three transmitters. The total induced voltages within transmitters 1, 2 and 3, namely V_{T1}, V_{T2} and

V_{T3}, which are caused by the crossing mutual inductances from other transmitters; are given by (4.5). It should be noted that $M_{12} = M_{21}$, $M_{13} = M_{31}$ and $M_{23} = M_{32}$. These crossing induced voltages do not affect the receiver's induced voltage V_s and output power P_o, but cause higher input current stresses on the inverter and the resonant components L_{ia} and C_{ia}. This increases conduction losses and operating temperatures on primary components. As reported in Chapter 6, the temperature on the power MOSFET reaches 123 °C with only 0.2 kW output power and 300 V input DC. Therefore, elimination of the induced voltages on transmitters is a prerequisite to achieve a higher output power level.

$$\begin{cases} V_{T1} = j\omega_o M_{12} I_2 + j\omega_o M_{13} I_3 \\ V_{T2} = j\omega_o M_{21} I_1 + j\omega_o M_{23} I_3 \\ V_{T3} = j\omega_o M_{31} I_1 + j\omega_o M_{32} I_2 \end{cases} \tag{4.5}$$

To eliminate the crossing induced voltages on each transmitter, compensation capacitors, (e.g. C_{com1}, C_{com2} and C_{com3}) are added into each transmitter, producing a reversed voltage against V_{T1}, V_{T2} and V_{T3}. From the experimental measurements, all crossing mutual inductances have the same negative value because of the transmitter's winding layout. Therefore, one can set $M_{12} = M_{21} = M_{13} = M_{31} = M_{23} = M_{32} = M_{cros}$, in which M_{cros} is a negative number. Further derivations have been applied to (4.5) and V_{T1}, V_{T2} and V_{T3} can be expressed as follows depending on M_{cros}:

$$\begin{cases} V_{T1} = j\omega_o M_{cros} I_1 e^{j\frac{2\pi}{3}} + j\omega_o M_{cros} I_1 e^{j\frac{4\pi}{3}} = -j\omega_o M_{cros} I_1 = j\omega_o |M_{cros}| I_1 \\ V_{T2} = j\omega_o M_{cros} I_2 e^{j\frac{-2\pi}{3}} + j\omega_o M_{cros} I_2 e^{j\frac{2\pi}{3}} = -j\omega_o M_{cros} I_2 = j\omega_o |M_{cros}| I_2 \\ V_{T3} = j\omega_o M_{cros} I_3 e^{j\frac{-4\pi}{3}} + j\omega_o M_{cros} I_3 e^{j\frac{-2\pi}{3}} = -j\omega_o M_{cros} I_3 = j\omega_o |M_{cros}| I_3 \end{cases} \tag{4.6}$$
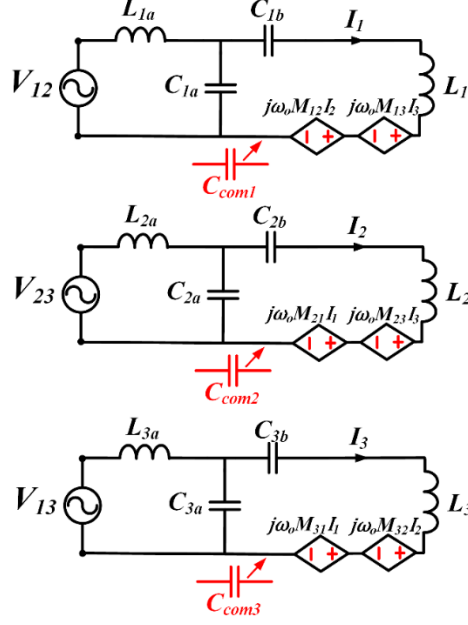
Fig. 4.4. Primary LCC tanks considering magnetic interferences.

Voltages on compensation capacitors (i.e. V_{Ccom1}, V_{Ccom2}, V_{Ccom3}) should be equal in magnitude and reversed in phase with (V_{T1}, V_{T2}, V_{T3}) to effectively cancel these above crossing induced voltages.

$$\begin{cases} V_{Ccom1} = \dfrac{1}{j\omega_o C_{com1}} I_1 = -V_{T1} \\[2mm] V_{Ccom2} = \dfrac{1}{j\omega_o C_{com2}} I_2 = -V_{T2} \\[2mm] V_{Ccom3} = \dfrac{1}{j\omega_o C_{com3}} I_3 = -V_{T3} \end{cases} \tag{4.7}$$

Therefore, three compensation capacitors can be calculated based on (4.8). These capacitors have the same value and depend only on crossing mutual inductances as well as the operating frequency.

$$\begin{cases} C_{com1} = \dfrac{1}{\omega_o^2 |M_{cros}|} \\[2mm] C_{com2} = \dfrac{1}{\omega_o^2 |M_{cros}|} \\[2mm] C_{com3} = \dfrac{1}{\omega_o^2 |M_{cros}|} \end{cases} \tag{4.8}$$

Finally, C_{com1}, C_{com2} and C_{com3} can be integrated into C_{1b}, C_{2b} and C_{3b} to form a single series capacitor for each phase, which can be calculated by (4.9). In Chapter 6, experimental results

are presented to compare two scenarios of including and not including these compensation capacitors.

$$
\begin{cases}
C_{1b} = \dfrac{1}{\omega_o^2(L_1 - L_{1a} + |M_{cros}|)} \\[2mm]
C_{2b} = \dfrac{1}{\omega_o^2(L_2 - L_{2a} + |M_{cros}|)} \\[2mm]
C_{3b} = \dfrac{1}{\omega_o^2(L_3 - L_{3a} + |M_{cros}|)}
\end{cases}
\tag{4.9}
$$

In a dynamic charging system, constant current charging is preferred over constant voltage charging because the EV battery's state of charge (SoC) unlikely reaches the point of being fully charged [1]. Therefore another LCC tank is constructed at the secondary side tank to produce the output current source, as shown in Fig. 4.5. Capacitor C_{1s} is connected in series with L_s while C_{2s} and L_{1s} are an additional parallel capacitor and inductor for the secondary tank, respectivelly. According to the equivalent circuit in Fig. 4.5, DC output current is depicted as (4.10) if the resonant tank at the secondary side is designed to follow (4.11) and (4.12).

$$
I_{bat} = \frac{2}{\pi}\omega_o^2 C_{2s}\left|\sum_{i=1}^{3} M_{is}I_i\right| = \frac{3\omega_o^2 C_{2s}M_oI_o}{\pi} = \frac{6\sqrt{3}}{\pi^2}\omega_o^3\,C_{ia}C_{2s}M_oV_{in}
\tag{4.10}
$$

$$
j\omega_o L_s + \frac{1}{j\omega_o C_{1s}} + \frac{1}{j\omega_o C_{2s}} = 0
\tag{4.11}
$$

$$
j\omega_o L_{1s} + \frac{1}{j\omega_o C_{2s}} = 0
\tag{4.12}
$$
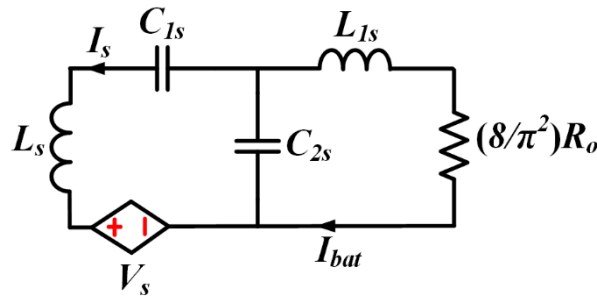
Fig. 4.5. AC equivalent circuit of the secondary circuit.

Combining (4.3), (4.9), (4.11) and (4.12), the equation of the resonant frequency ω_o can be determined as (4.13), in which ω_o is independent of both, load condition (R_o) and mutual inductances between the transmitters and the receiver (M_{1s}, M_{2s} and M_{3s}).

$$\omega_o^2 = \frac{1}{L_{ia}C_{ia}} = \frac{1}{C_{ib}}\left(\frac{1}{L_i - L_{ia}} + \frac{1}{|M_{cros}|}\right) = \frac{1}{L_{1s}C_{2s}} = \frac{1}{C_{1s}}\left(\frac{1}{L_s - L_{1s}}\right) \quad (i = \overline{1,3}) \qquad (4.13)$$

The DC output voltage and power are given by (4.14) and (4.15), adopting R_o, which is the equivalent battery's impedance. It needs to be emphasized that if the resonant frequency ω_o and the secondary side capacitor C_{2s} are assumed to be constant, then the output power depends only on the multiplication of $M_o I_o$. Obviously, it can be seen that P_o is constant irrespective of the receiver's position.

$$V_{bat} = I_{bat}R_o = \frac{6\sqrt{3}}{\pi^2}\omega_o^3\, C_{ia}C_{2s}M_oV_{in}R_o \qquad (4.14)$$

$$P_o = I_{bat}^{\;2}R_o = \left(\frac{6\sqrt{3}}{\pi^2}\omega_o^3\, C_{ia}C_{2s}M_oV_{in}\right)^2 R_o \qquad (4.15)$$

4.4 Design of magnetic couplers

4.4.1 Design of three-phase transmitters

This section presents an example of transmitters' magnetic design aiming at achieving maximum output power of 3 kW. The specified power of 3kW is selected for the demonstrator due to this being the smallest possible scale for the EV charging level 1. The maximum power is also the targeted level power of the experimental test-rig. Extensive simulations are carried out using MAXWELL 3D software to obtain the optimal parameters for transmitters, which are presented in Fig. 4.6. They constitute the ferrite pole sizes (thickness t_p, distance d_p, height h_p, length l_p and plate width w_p) and ferrite bottom dimensions (width w_b and thickness t_b), as well as the number of turns for three transmitters' windings N_1, N_2 and N_3. As the three transmitters are identical, for simplicity only one transmitter is considered in the simulation model, which is shown in Fig. 4.7. The purpose of the simulation is to determine the optimal parameters so that the maximum of magnetic flux density B can be attained at the centre of each of the three poles (as shown in Fig. 4.6). With an appropriate receiver design, maximum of B also means maximum coupling coefficient and the highest power delivery as well as efficiency. Simultaneously, it is required to minimize the ferrite core's volume and the cable length, but the system still needs to satisfy the power delivery requirement and avoid saturation of the core. In order to produce a homogeneous magnetic flux along the driving direction, an equal number of turns should be selected for three windings and all three transmitters' currents

are set at a maximum of 20 A. Please note that the value of 20 A is associated with the output power of 3 kW. In cases of a higher power level, the value of the transmitters' current will be higher as well. Furthermore, the maximum air-gap between transmitter and receiver is selected as 15 cm in this work.

Thickness and width of the pole and bottom ferrite plates are selected to prevent saturation problems. Thereout, thickness values have a very limited effect on the magnetic field level. Fig. 4.8 presents the distribution of magnetic flux on the bottom ferrite core with the bottom thickness (t_b) = pole plate thickness (t_{pp}) = 0.5 cm and pole thickness (t_p) = 1.5 cm. According to that, the maximum magnetic flux density of 0.152 T occurs around the crossing winding areas on the core's bottom. In this work, the ferrite core of PC47 by TDK Electronics is selected and its saturated magnetic flux density B_s is founded as 0.54 T at 25 °C [2]. Therefore, it can be guaranteed that no saturation for the primary core with an output power level of 3 kW and a transmitter current of 20 A. If the power level increases, then the thickness values should be larger to overcome the potential saturation. Note that it is possible to implement smaller thickness values; however, values below 0.5 cm are difficult to achieve practically due to the physical cutting process of ferrite. Moreover, the widths of the pole and bottom ferrite plates are selected to be as small as possible to reduce the width of the transmitter, so that the implementation cost and pedestrian stray fields contamination can be reduced. However, when the transmitters' width is reduced, then the coupling coefficient decreases as well. This trade-off relationship is illustrated in Chapter 5. Here, the widths of both the bottom and pole ferrite plate are selected as 12 cm for simplicity.
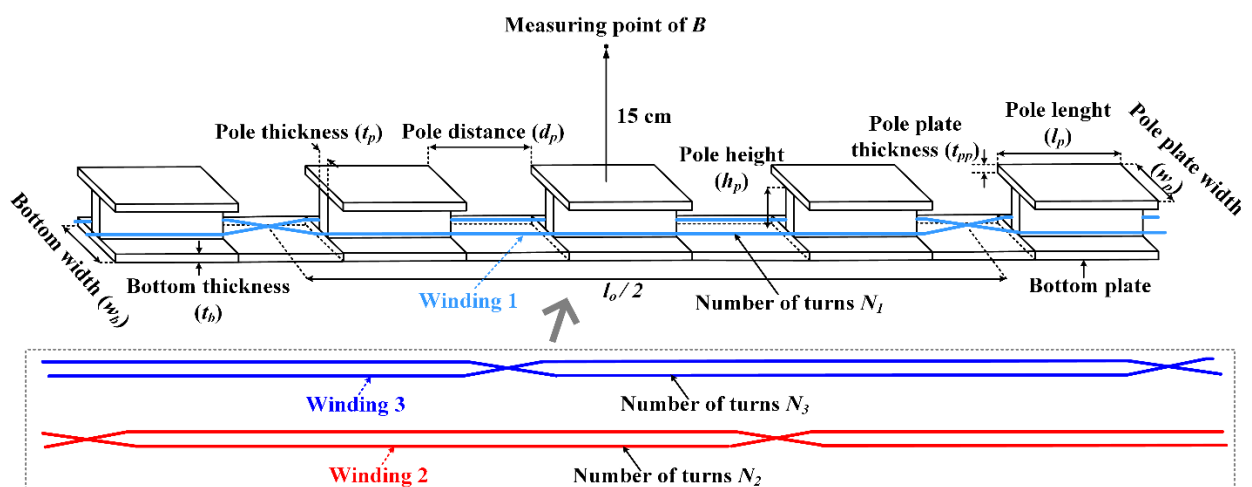
Fig. 4.6. Design parameters of three-phase primary transmitters.
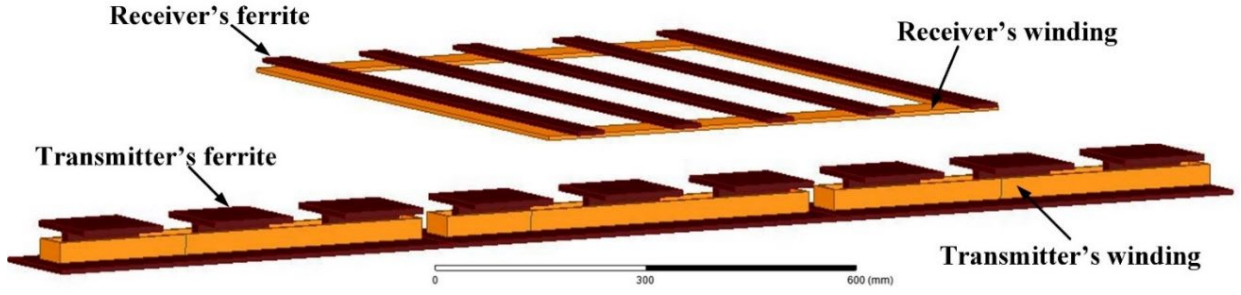
Fig. 4.7. Simulation model of the proposed transmitters with the parameters from Table 4.1 while the pole distance d_p and number of turns N_1 are varied in simulation.
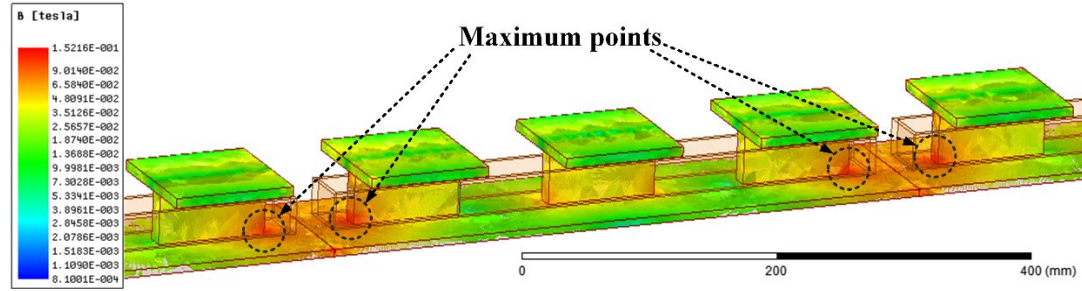
Fig. 4.8. Contribution of magnetic flux density on the transmitter's ferrite core with $N_1I_1 = 80$ A.

The remaining three design parameters are pole distance (d_p), pole length (l_p) and number of turns (N). The relationship between d_p and l_p is given by (4.16) with l_o being fixed based on the system's requirements, which is 240 cm in this work. Therefore, only d_p needs to be found and l_p will follow according to (4.16). Fig. 4.9 presents the relationship between normalized magnetic coupling and pole distance d_p. It is noted that the measurement point is located right above the centre of each group of three ferrite poles, as shown in Fig. 4.7. When d_p varies in a range from 5 to 22.5 cm, then the normalized value of magnetic flux density reduces accordingly. It can be seen that the maximum magnetic flux density value can be achieved at pole distances from 5 to 7.5 cm. This fact can be explained by deriving the magnetic flux equations depending on the winding's width and length [3]. A value of 7.5 cm for d_p is then selected in this work because a 5-cm value creates quite a small space which may not incorporate a large enough number of winding turns.

$$d_p + l_p = \frac{l_o}{6} \tag{4.16}$$

Fig. 4.10 demonstrates how magnetic flux density B_1 varies according to the number of turns N_1 for one single winding. Theoretically, B_1 becomes linear with N_1, and when the number of turns increases from two to six, B_1 rises from 31 to 93 µT as a result. A higher number of turns results in higher power delivery capability; however, it also increases the total length of the

copper wire, transmitter inductance and pedestrian stray fields contamination. A total of four turns is finally selected and Litz wire (600 strands-AWG 38) is chosen to reduce conduction losses on windings. After several iterations of parameter search in both simulations and experiments, the final parameters are selected as depicted in Table 4.1 to meet the system requirements.
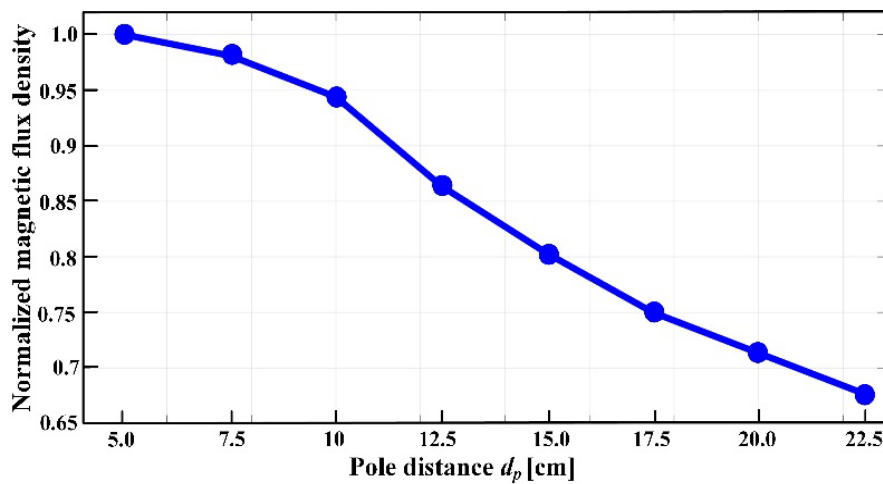
Fig. 4.9. Normalized magnetic flux density depending on the pole distance with $N_l I_l = 80$ A.
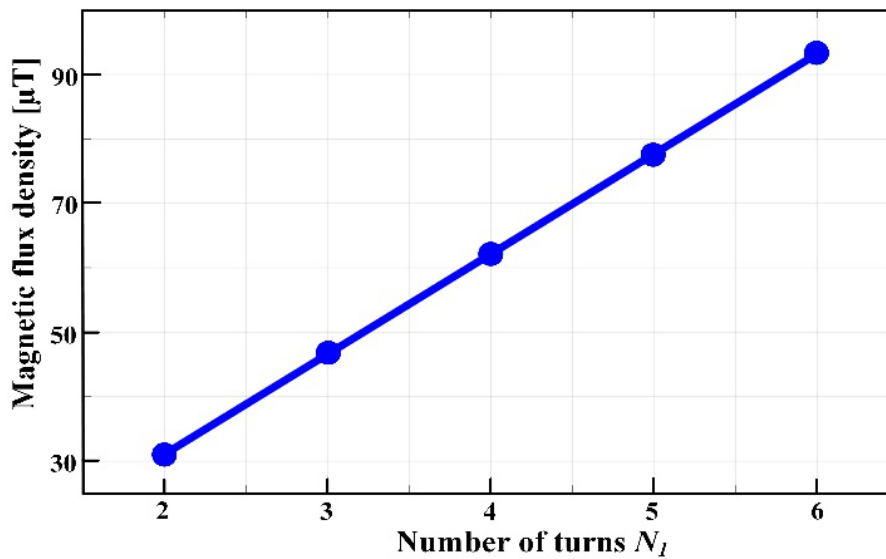
Fig. 4.10. Magnetic flux density depending on the number of turns with $d_p = 7.5$ cm.

TABLE 4.1

t_b	Bottom thickness	0.5 cm
w_b	Bottom width	12 cm
t_p	Pole thickness	1.5 cm
d_p	Pole distance	7.5 cm
h_p	Pole height	4 cm
l_p	Pole length	12 cm
w_p	Pole plate width	12 cm
t_{pp}	Pole plate thickness	0.5 cm
d	Air-gap	15 cm
	Number of ferrite poles (individual pole)	12
	Number of windings	3
N_1, N_2, N_3	Number of turns for each winding	4
$2l_o$	Total length of transmitter	240 cm
I_1, I_2, I_3	Transmitter's currents (maximum)	20 A

4.4.2 Design of the receiver

After obtaining the transmitter's parameters, this section provides the design for the receiver's parameters, which include receiver length l_r, width w_r and number of turns N_s. The most sensitive parameter that influences the coupling coefficient k is the receiver length l_r. Fig. 4.11 shows how the coupling coefficient varies against l_r with transmitter parameters listed in Table 4.1. As shown in Fig. 4.11, the normalized coupling value increases from 0.05 at $l_r = 30$ cm and reaches the highest value when $l_r = 60$ cm (equal to $l_o/2$). If l_r goes higher than 60 cm, then k drops significantly to nearly zero at 100 cm. It can be explained by the fact that when $l_r <$ 60 cm, the receiver winding cannot entirely cover the transmitter winding, therefore k is always lower than the highest value. For $l_r > 60$ cm, the receiver has also received magnetic fluxes from the other two adjacent transmitter windings which have reversed current directions and created opposite magnetic fluxes as compared to the aligned transmitter winding. In summary, there is a flux reduction on the receiver when $l_r > 60$ cm compared to the highest case. More seriously, the total flux on the receiver can be cancelled completely if the total flux coming in

is equal to the flux coming out of the receiver. It results in no coupling between the two sides and no induced voltage in the receiver winding.
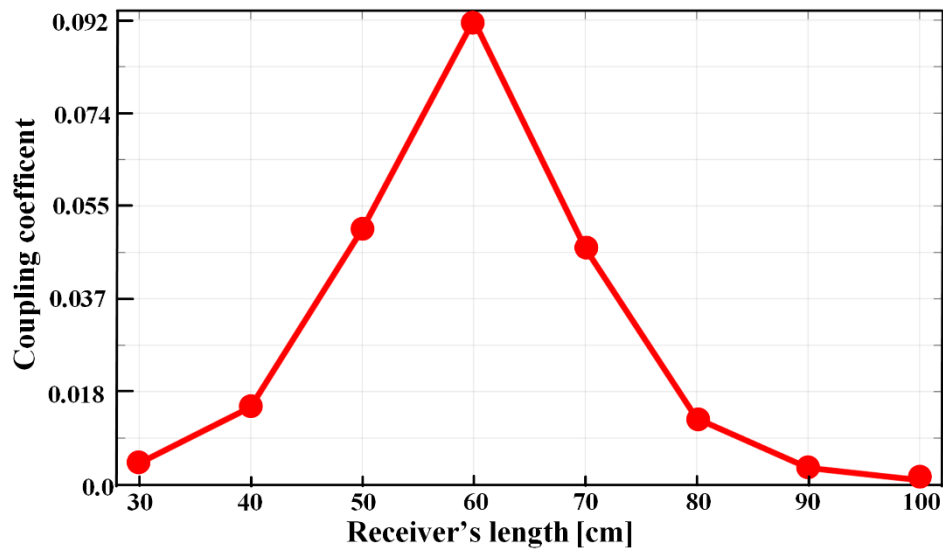
Fig. 4.11. Maxwell 3D simulation of the coupling coefficient with transmitter's parameters from Table 4.1 against different receiver's lengths.

Fig. 4.12 and 4.13 provide the simulation results of the coupling coefficient under different receiver widths and lateral misalignment values. The coupling value k needs to be as high as possible at different lateral misalignment conditions. Fig. 4.12 provides coupling values regarding different receiver widths w_r under no misalignment. It shows that k increases from 0.062 to nearly 0.1 when w_r rises from 10 to 30 cm. However, if w_r continues to increase to 70 cm, then k will slightly reduce. Under lateral misalignment conditions, it can be seen in Fig. 4.13 that how reduction of the coupling coefficient depends on w_r. If the misalignment level equals 30 cm, then k will reduce to nearly 0%, 30% and 60% associated with $w_r =$ 50, 60 and 70 cm, respectively. Fundamentally, higher w_r values enhance coupling and output power under lateral misalignment; however, the coupling coefficient is also reduced when increasing w_r at the perfect aligned condition. Moreover, w_r is also limited by the installation space at the bottom of the vehicle. Considering all of the above factors, w_r is selected as 60 cm in this work so that the output power level can remain at 30% of maximum power under 30 cm of lateral misalignment. After selecting receiver dimensions of $l_r = w_r = 60$ cm, then the number of turns N_s can be estimated as eight turns based on the required output voltage (i.e. 450 V) and operating frequency (i.e. 85 kHz).

Please note that these results do not investigate how the ferrite area affects the coupling between two couplers and only the receiver's dimensions are analysed in this chapter. The ferrite area effect is investigated in the following chapter 5. Similar to the transmitter's width, the receiver's ferrite area also affects the associated cost and efficiency in two different and opposite ways. Chapter 5 will discuss in more detail the trade-off relationship caused by the transmitter's width and receiver's ferrite area.
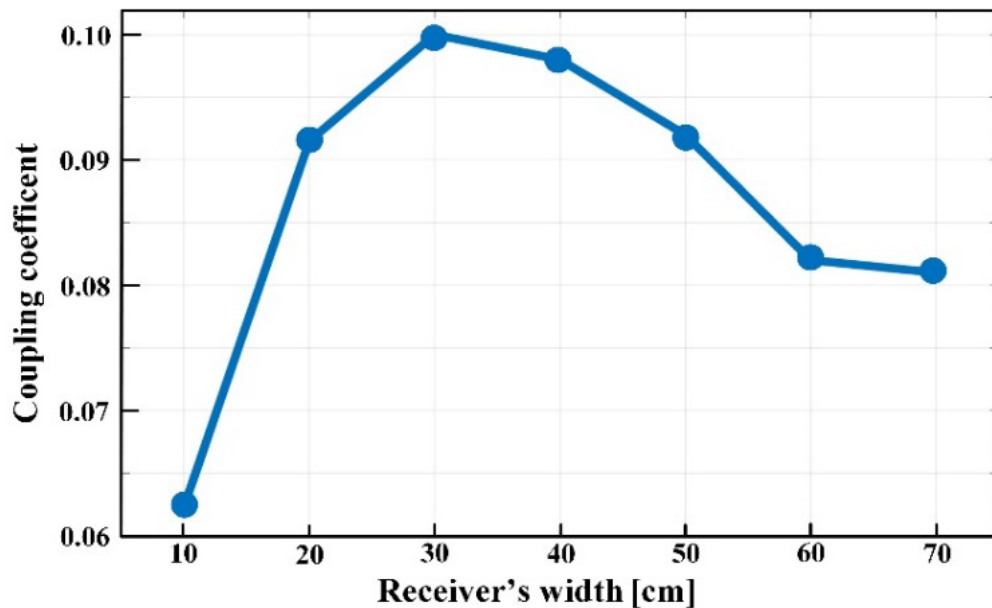
Fig. 4.12. Maxwell 3D simulation of the normalized coupling coefficient with the transmitter's parameters from Table 4.1 against different receiver's widths at no misalignment.
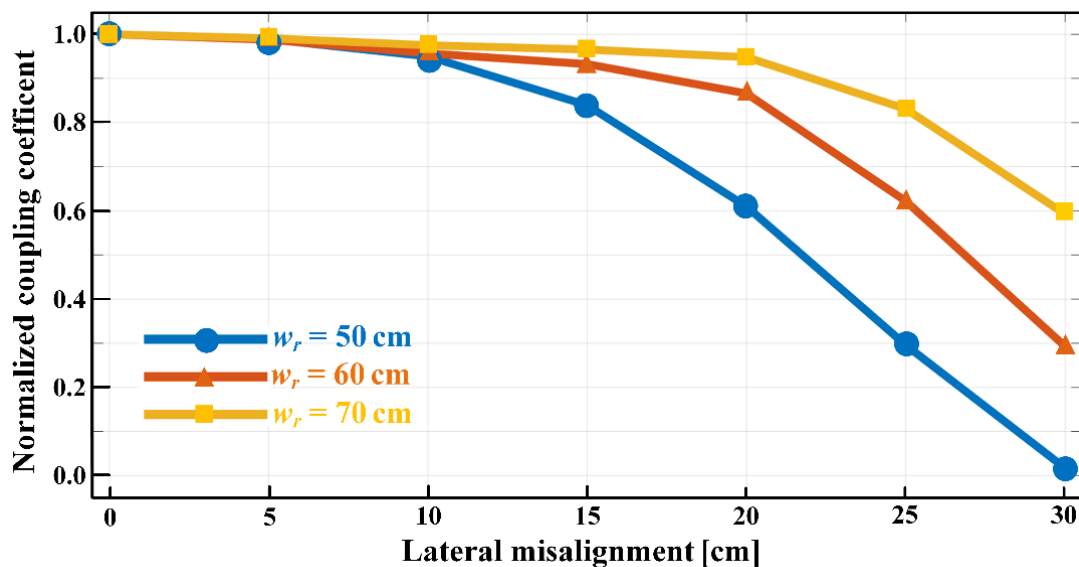
Fig. 4.13. Maxwell 3D simulation of the normalized coupling coefficient with the transmitter's parameters from Table 4.1 against different lateral misalignment conditions.

4.5 Chapter summary

 This chapter provided a detailed design procedure of the multiphase WDC system with an illustrative example of the three-phase system. Firstly, the selection of the number of phases is a trade-off between one side being efficiency and power capability and the other side being cost and system complexity. Next, the detailed parameter design of the resonant circuit considering magnetic interferences is provided. To mitigate the crossing induced voltages on each transmitter, compensation capacitors C_{com1}, C_{com2} and C_{com3} are added into each transmitter, producing a reversed voltage against the crossing induced voltages.

   After that, the optimized design of the magnetic coupler is presented. An optimization analysis using Maxwell 3D simulation for both transmitter and receiver is carried out to achieve the highest coupling factor by using minimum ferrite material and copper cable. On the transmitter side, several parameters are considered. Firstly, the thickness values of the ferrite core are considered to avoid saturation with a corresponding power level. Next, different pole distances are simulated, and the value of the coupling factor is reduced when the pole distances increase. Similarly, the dimensions of length and width for the receiver are optimized based on the fixed transmitter's parameters. In this chapter, transmitter width and the receiver's ferrite area are not included in the design process. However, these parameters will be analysed in detail in Chapter 5.

4.6 References

[1] V. B. Vu, D. H. Tran and W. J. Choi, "Implementation of the Constant Current and Constant Voltage Charge of Inductive Power Transfer Systems with the Double-Sided LCC Compensation Topology for Electric Vehicle Battery Charge Applications," IEEE Transactions on Power Electronics vol. 33, no. 9, pp. 7398 - 7410, Sep. 2018.

[2] [Online] Characteristics of Mn-Zn ferrite materials - TDK Product Center. Available: https://product.tdk.com.

[3] M. Misakian, "Equations for the magnetic field produced by one or more rectangular loops of wire in the same plane," Journal of Research-National Institute of Standards and Technology, vol. 105, no. 4, Aug. 2000.

CHAPTER 5

Efficiency-cost parametric-analysis for the WDC system

5.1 Background

A number of factors must be considered carefully when designing a multiphase WDC system. These factors are directly related to the wireless couplers, which includes: transmitter's width, receiver's area and weight, used magnetic core volume, air-gap between two coils, level of misalignment, etc. The WDC system performances significantly rely on these factors. Furthermore, the transmission efficiency depends heavily on the coupling factor k between transmitter and receiver coils as well as the quality factor Q of each coil. Both, k and Q depend on the coupler's dimensions, used materials and the air-gap of the couplers. To effectively design a wireless coupler for EVs application, the multi-objective approach has been used in [1-4] to evaluate the system performance such as efficiency, stray field exposure, power density and tolerance under misalignment conditions. Specifically, the design trade-off between efficiency (η) and power quality (α) in the forms of Pareto fonts are conducted for the circular shape coupler in [1]. A comprehensive evaluation between rectangular and double-D coupler geometries for high power wireless charger of 50 kW are also presented in [3]. The work in [4] extends the multi-objective method presented in [1-3] to compare all conflicting performances of four major coupler topologies. These include the circular, rectangular, double-D, and the double-D transmitter with double-D-quadrature receiver.

Another important factor to be considered in the WDC system is the implementation cost [5-6]. The initial cost in the WDC system for EVs is significantly higher than the stationary wireless charger and the conventional conductive charger. The main driver for the high cost of the charging infrastructure is the primary side, which consists of power inverters, the associated resonant tank and especially the transmitter coils. A suitable design for minimizing the cost while maintaining good efficiency, therefore is of paramount importance. The total cost of the system is directly linked with the variation of the coupler's parameters. Therefore, the magnetic

design of coupler coils is of prime importance in order to satisfy the requirements of the targeted efficiency and cost.

In this Chapter, the efficiency-cost parametric-analysis of the three-phase WDC system is presented based on the finite-element analysis (FEA) simulation and analytical model. Firstly, a parametric-analysis process is proposed for the multiphase WDC system and the 3-phase system is used as an illustration in this work. Two coupler's factors of transmitter's width W_p and receiver's ferrite area A_r are utilized as variables in the analysis. W_p significantly affects the initial cost because of not only ferrite cost but the cost associated with the construction on the road. The FEA simulation is utilized to extract the coupling coefficient and quality factor of the two coils. At this point, compensation capacitors and inductors are calculated to guarantee the conditions of the output power and current following Chapter 4. A loss model is used to determine all losses in the multiphase system when both W_p and A_r are varied. Therefore, the cost and efficiency parametric-analysis curves are generated. The results indicate how the two performances of efficiency and cost are in a trade-off relationship. The parametric-analysis design is validated by means of simulation and experiment of WDC system with 240 cm transmitter length. Based on the parametric-analysis process and other constrains, such as budget and availability of space and material, a scaled-down prototype with the normalized cost factor of 0.845 is developed in the lab.

5.2 Parametric-analysis procedure of the three-phase WDC system

The efficiency-cost parametric-analysis process is outlined in Fig. 5.1 which focuses on the coupler's parameters. There are eight steps in the parametric-analysis process. It begins with the definition of the three-phase WDC charger specification including the output current, voltage, air-gap, operating frequency, and stray fields level limitation. The specification can be found in Table 5.1. Simultaneously the system must follow the design rules to provide a constant output power when the receiver is in motions along the driving direction. These design equations (e.g. section 4.3) are derived in Chapter 4 and are not repeated in this Chapter.

TABLE 5.1

SPECIFICATIONS OF THE WDC PROTOTYPE

Symbol	Parameters	Value
V_{in}	Input voltage	400 V
I_{bat}	Rated output current	6.5 A
V_{bat}	Rated output voltage	450 V
P_o	Rated output power	3 kW (constant when the EV is in motion along the driving direction)
D	Normal air-gap	15 cm
f	Switching frequency	85 kHz
	stray fields level	< 27 μT @ 1-meter far away from Transmitter

Step 1: Output power, current, voltage level, air-gap, frequency, EMI level limitations, etc

System Specifications

Step 2: hybrid length, I type shape with ferrite, 3 phases. Fix parameters: thickness, pole distances, No. turns

Select the coupler topology and some parameters

Step 3: transmitter width = (5cm, 21cm, ++2cm) Receiver's ferrite area = (0cm2, 0.36cm2, ++0.06 cm)

Select the boundary and step variation for optimization

Step 4: using the FEA software to simulate with different conditions of parameters in Step 3

Calculate the coupling, self-inductance L1 and L2

Step 5: other components such as capacitors and inductors are determined based on conditions in Step 1

Calculate other parameters of resonant tank

Step 6: calculate of loss in every single component of the prototype such as coil, capacitors, switches, diodes

Determine the total losses based on the loss model for each component

Step 7: calculate the total costs including the fixed and variable parts

Determine the total implemented costs

Efficiency   Cost

Step 8: Realize the trade-off relationship between efficiency and cost

Draw optimization curves

Fig. 5.1. Parametric-analysis process for the multiphase WDC system.

In the beginning stage (Step 2) of the parametric-analysis process, several transmitter's parameters are initialized, which include ferrite's thickness, pole distance and number of turns. The WDC couplers are presented in the following figures, in which the three-phase transmitters are shown in Fig. 5.2, while the receiver with a rectangular shape is depicted in Fig. 5.3. It should be noted that some coupler's parameters from Chapter 4 including $\{t_b, w_b, t_p, d_p, h_p, l_p, w_p$ and $t_{pp}\}$ are used again here. According to that, the length of 240 cm with the I-type shape core is selected for one transmitter's module. The multiphase system is designed and optimized for 3 phases as an example. Thickness values (T_b, T_{pp} and T_p) are selected such that saturation is avoided, therefore, these values have a minority influence on the coupling factor k. The pole distances d_p, on the other hand, has a significant impact on k. To simplify the parametric-analysis process, both thickness values and d_p are kept constant in this work. In the secondary side, the length and width of the receiver pad, l_r and w_r are designed to match with the selected d_p for maximum coupling factor under different lateral misalignment conditions. As a result, a dimension of 60 cm x 60 cm is implemented for the receiver. Table 5.2 summarizes the fixed parameters of the coupler.

TABLE 5.2
FIXED PARAMETERS OF THE COUPLER

Symbol	Parameters	Value
	Transmitter's parameters	
T_p	Pole thickness	1.5 cm
T_b	Bottom thickness	0.5 cm
T_{pp}	Pole plate thickness	0.5 cm
H_p	Pole height	4 cm
D_p	Pole distance	7.5 cm
$2l_o$	Length of 1 module	240 cm
	Rated Transmitter currents (RMS)	20 A
	Number of turns	4
	Receiver's parameters	
R_l	Length	60 cm
R_w	Width	60 cm
	Receiver's winding's width	5 cm
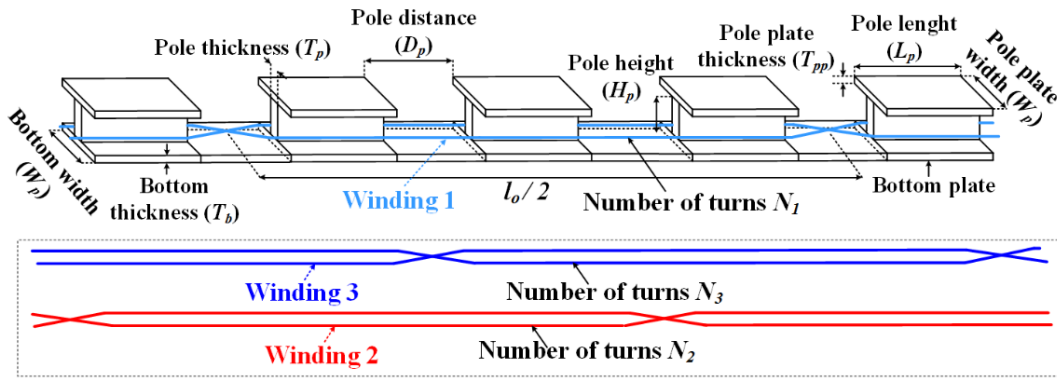
Fig. 5.2. The parameters of the three-phase transmitter coupler.
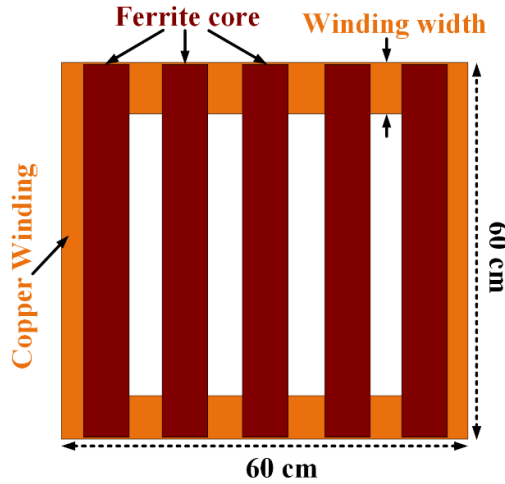
Fig. 5.3. The parameters of the receiver coupler.

After deciding on the fixed parameters above, the other two parameters in the coupler are varied for the parametric-analysis process, i.e. transmitter's width W_p and receiver's ferrite area A_r. A look-up table (i.e. Table 5.3) is then generated to describe the range and the incremental steps of each W_p and A_r. The FEA model is set up in Maxwell 3D software for each design point to compute their electromagnetic behaviour as shown in Fig. 5.4. To reduce the computation time, the Litz wire winding is created by a 3D lumped model with uniform current density. There are 63 different operating points in total resulted from the different combinations between W_p and A_r. Then, the self-inductances of transmitter and receiver (e.g. L_1 and L_2) as well as the coupling factor k are calculated using Maxwell 3D software as depicted in Step 4. This process is repeated for all the 63 combinations. After obtaining all values of L_1, L_2, and k, other parameters of the resonant tank are then calculated in Step 5 in accordance with the design rules described in Chapter 4 to satisfy the system specification of Table 5.1.

TABLE 5.3
SYSTEM VARIABLE PARAMETERS

Symbol	Parameters	Min	Max	# Points
W_p	Transmitter's Width	5 cm	21 cm	14 (Inc. of 2cm)
A_r	Receiver's ferrite area	0 cm^2	3600 cm^2	7 (Inc. of 600 cm^2)
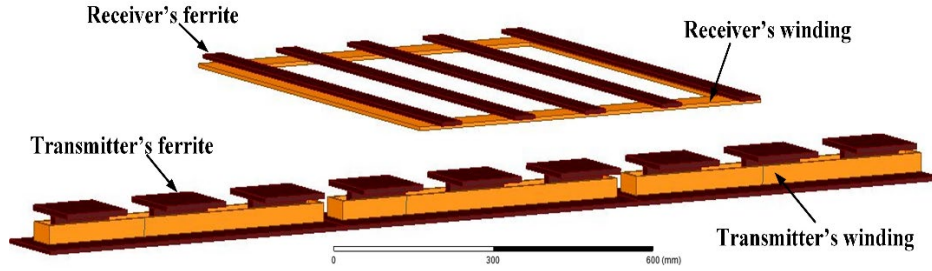
Fig. 5.4. Simulation model of the couplers with the fix parameters in Table 5.2 and the variable parameters in Table 5.3.

In Step 6, a loss model is developed to determine the total losses of the whole circuit, which includes the conduction and switching losses of the inverter, core and copper losses of resonant inductors and the coupler as well as the conduction losses of capacitors and diode rectifier. From that results, the estimated efficiency is calculated for all the 63 different operating points. The details of the loss calculation are presented in Section 5.3.

After determining the efficiency, the total cost of the system, which is divided into two parts, fixed and variable costs; can be obtained. Fixed costs include every component apart from ferrite cores in both transmitter and receiver, and the copper wires of the transmitter. It is because the variable cost only relates to the variable parameters of W_p and A_r. Furthermore, for simplicity, the cost of all resonant capacitors and inductors are assumed to be the same despite the fact that their values might slightly change. It is because the cost of capacitors and inductors do not vary substantially. Variable costs are associated with two variable parameters of W_p and A_r for transmitter and receiver. In this work, all costs are determined which associate with the specification in Table 5.1 while the detailed calculation is depicted in Section 5.3.

Finally, the system efficiency and the implemented costs are presented as the parametric-analysis curves according to two variables of W_p and A_r. From the results, a suitable design is chosen for the realization of a prototype, considering the trade-off between efficiency and cost as well as the budget and availability of space and material.

5.3 System efficiency calculation

The resulting data from Step 4 is post-processed to calculate the parameters of the circuit's resonant tank in Step 5. After that, the losses in the coupler and whole system are extracted. All the losses of every components are considered in the analysis. All loses are considered for the efficiency calculation, which include: coupler's coils (i.e. L_1, L_2, L_3 and L_s), inverter (i.e. conduction and switching losses), resonant inductors (i.e. L_{1a}, L_{2a}, L_{3a} and L_{1s}), resonant capacitors (i.e. C_{1a}, C_{1b}, C_{2a}, C_{2b}, C_{3a}, C_{3b}, C_{1s} and C_{2s}), and the diode rectifier. This section firstly presents the loss model and after that, the efficiency is calculated based on the total losses and the output power.

A. Losses in the wireless coils

The coupler losses include the copper losses (P_{cu}) and the ferrite losses (P_{fe}). P_{cu} constitutes P_{se} losses (caused by skin effects) and P_{pe} losses (caused by proximity effect). The equations for P_{se}, P_{pe} and P_{cu} are given as follows (5.1-5.3) based on [1-4].

$$P_{se} = n_{st}.R_{dc}.F_R(f).\left(\frac{I_{peak}}{n_{st}}\right)^2 \tag{5.1}$$

$$P_{pe} = n_{st}.R_{dc}.G_R(f).\left(H_e^2 + \frac{I_{peak}^2}{2\pi^2 d_a^2}\right) \tag{5.2}$$

$$P_{cu} = P_{se} + P_{pe} \tag{5.3}$$

In (5.1), n_{st} denotes the number of stands in the Litz wire (i.e. 600 strands in this work), R_{dc} is the DC resistance per unit length of a single strand Litz wire, I_{peak} is the transmitter current peak value and $F_R(f)$ is a frequency-dependent factor of skin effect [7]. In (5.2), d_a is the outer diameter of the single strand Litz wire, $G_R(f)$ depicts a frequency dependent factor of proximity effect while H_e represents the external magnetic penetrating the windings. The coefficients of $F_R(f)$ and $G_R(f)$ are obtained from [7] while R_{dc} is taken from the manufacturer data [10].

The ferrite core losses can be calculated based on the Steinmetz equation where V is the region of ferrite in three-dimensional space.

$$P_{fe} = \iiint_0^V k_s f^\alpha B^\beta \, dxdydz \tag{5.4}$$

In this work, the core material of PC47 from TDK Electronics is used [8]. The Steinmetz parameters k_s, α, and β of the PC47 material are 5.78, 1.35 and 2.46, respectively.

B. Losses of the inverter

The inverter's losses include conduction and switching losses. The total conduction loss is the sum of loss on every switch S_i $(i = 1,6)$. Since the losses of S_1, S_2, and S_3 are equal to S_4, S_5, and S_6, respectively, therefore the total conduction losses of the three-phase inverter P_{cd} can be found as follows:

$$P_{cd} = 2R_{ds}(I_{ds1}^2 + I_{ds2}^2 + I_{ds3}^2) \tag{5.5}$$

where, R_{ds} is the on-state resistance while I_{dsi} $(i = 1,3)$ are the RMS value of the drain current through switch S_i. On the other hand, the total switching losses in the three-phase inverter can be represented as follows:

$$P_{sw} = \sum_{i=1}^{6} \frac{1}{2} V_{DS} I_{dsi} f(t_{oni} + t_{offi}) \tag{5.6}$$

In (5.6), t_{oni} and t_{offi} are the turn-on and turn-off times of MOSFET switch S_i $(i = 1,6)$, respectively, f is the switching frequency while V_{DS} is identical with the input DC voltage V_{in}. Eq. (5.6) is a generic equation that include both switching losses of not achieving Zero-Voltage-Switching (ZVS) and Zero-Current-Switching, ZCS. In the experiment, ZVS is achieved for the whole range of operation, therefore the losses associated with the ZVS will not be considered in the efficiency calculation since they are zero. Furthermore, the losses associated with not achieving ZCS is very small and negligible for the MOSFET devices. Therefore, the switching loss P_{sw} are zero in the analysis.

From (5.5) and (5.6), the total losses of inverter P_{inv} can be calculated as (5.7):

$$P_{inv} = P_{cd} + P_{sw} \tag{5.7}$$

C. Losses of resonant tanks

Losses of resonant tanks include the losses of resonant inductors P_{ind} (i.e. L_{1a}, L_{2a}, L_{3a} and L_{1s}) and resonant capacitors P_{ca} (i.e. C_{1a}, C_{1b}, C_{2a}, C_{2b}, C_{3a}, C_{3b}, C_{1s} and C_{2s}). While P_{ind} is determined by the same procedure discussed in Section 5.3.A, the capacitor dielectric loss of each capacitor P_{cai} can be calculated as follows.

$$P_{cai} = \frac{\tan\delta}{2\pi f C} I_C^2 \tag{5.8}$$

The dissipation factor $\tan\delta$ in (5.8) is selected as 0.08% at 85 kHz based on the datasheet from KEMET [9]. I_C is the RMS current through each individual capacitor. Moreover, the resonant capacitors are constructed using several low-ESR capacitors connected in parallel to reduce the total dielectric loss P_{ca}.

D. Losses of the rectifier

The conduction losses on the secondary side rectifier are calculated using (5.9), where V_{fwD} and r_D are the forward voltage and the on-state resistance of the rectifier's diode, respectively.

$$P_{rec} = \frac{4\sqrt{2}}{\pi} V_{fwD} I_o + 2r_D I_o^2 \tag{5.9}$$

From the above analysis, the system efficiency (η) of the three-phase WDC system is then obtained by:

$$\eta = \frac{P_{out}}{P_{out} + P_{cu} + P_{fe} + P_{inv} + P_{ind} + P_{ca} + P_{rec}} \tag{5.10}$$

The parameters of the system components used to calculate losses are summarized in Table 5.4 below.

TABLE 5.4
SYSTEM PARAMETERS FOR LOSS CALCULATION

Inverter MOSFET	
Part number	C2M0025120D
On state resistance R_{ds}	25 mΩ
Switching frequency f_{sw}	85 kHz
Turn-on time t_{on}	14 ns
Turn-off time t_{off}	29 ns
Litz wire (for Inductors and Couplers)	
Litz wire AWG	38
Number of strands n_{st}	600 strands
DC resistance per meter	0.01Ω/ meter
Ferrite Core	
Manufacturer	EPCOS (TDK)
Part Number (ferrite core I N87)	B66297K0000X187
Capacitors	
Manufacturer	KEMET
Dissipation factor (DF)	0.08%
Rectifier Diodes	
Part number	IDW30G65C5
Forward voltage	1.5 V

5.4 Cost calculation

The total cost of the WDC system includes the fixed part C_f and the variable part C_v. Table 5.5 lists the fixed cost part whereas the variable cost is given as follows:

$$C_v = E_p W_p + E_w l_t + E_A A_r \tag{5.11}$$

Where E_p is the cost per unit size of the transmitter top and bottom ferrite plates (£/cm); W_p is the transmitter width (cm); E_w is the cost per unit of transmitter winding (£/m); l_t is the total length of the transmitter winding (meters); E_A is the cost per unit size of receiver's ferrite (£/m²); A_r is the total area of receiver's ferrite (m²).

TABLE 5.5

THE FIXED COST PART

Component	Quality	Manufacturer	Price (£)
Transmitter ferrite poles	24 pieces	TDK Electronics	143
Receiver's copper winding	20 meters	Osco (UK)	100
PCB Connectors	10	RS Components Ltd	15
DSP Controller	1	Texas Instrument	505
Gate driver	3	Cree Inc.	150
Inverter	1	Cree Inc.	535
PCB circuits	2	Newbury Electronics (UK)	55
Protection box	2	Schneider Electric	98
Resonant capacitors	32	Kemet	80
Resonant inductors	4	TDK Electronics (ferrite core only)	32
Rectifier diodes	4	Vishay Semiconductors	33.88
Capacitor filter	2	EPCOS (Ger.)	12.3
Total fixed cost			1759.2

The variable cost C_v depicted in Fig. 5.5 is calculated using (5.11), for different values of W_p

and A_r. As mentioned earlier, the total length of transmitter windings l_t is proportional with the value of W_p. Each pair of (W_p, A_r) creates one different value of C_v. However, if ferrite material is not used in the receiver, then A_r is equal zero.

For clearer presentation, the normalized cost is defined in (5.12), which is used instead of the real cost. In (5.12) the fixed cost $C_f = £1759.2$, while $C_{v\_max} = £1615$. Nevertheless, the variable cost, C_v varies according to the Fig. 5.5.

$$Normalized\ cost = \frac{C_f + C_v}{C_f + C_{v\_max}} \qquad (5.12)$$
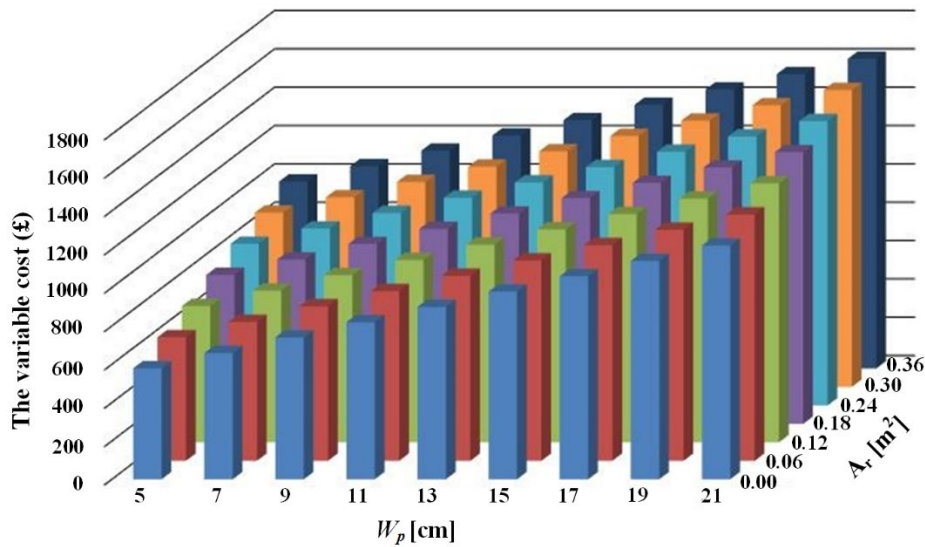
Fig. 5.5. The variable cost part with different values of W_p and A_r.

5.5 Parametric-analysis results and discussion

Based on the calculations of efficiency and cost in Section 5.3 and 5.4, the parametric-analysis results of the design examples are illustrated in Figs. 5.6-5.8. Furthermore, Figs. 5.6a and 5.6b represent the efficiency η and the normalized cost variations against W_p and A_r. Specifically, Fig. 5.6a shows that the efficiency η is proportional with both W_p and A_r. The reasons come from the fact that higher values of W_p and A_r result in an increase of coupling coefficient and coil quality factor as well as the transmission efficiency. Moreover, the incremental rate of η

100

versus A_r is not constant in which the rate is higher at the smaller values (i.e. 0.00 m^2 to 0.18 m^2) and slows down when A_r gradually reaches to the maximum value of 0.36 m^2. The situation is similar with W_p. On the other hand, the incremental rate of the cost is more linear with both W_p and A_r as shown in Fig. 5.6b. Hence, the operating points should not be selected when W_p and A_r are at high values to minimize the cost.
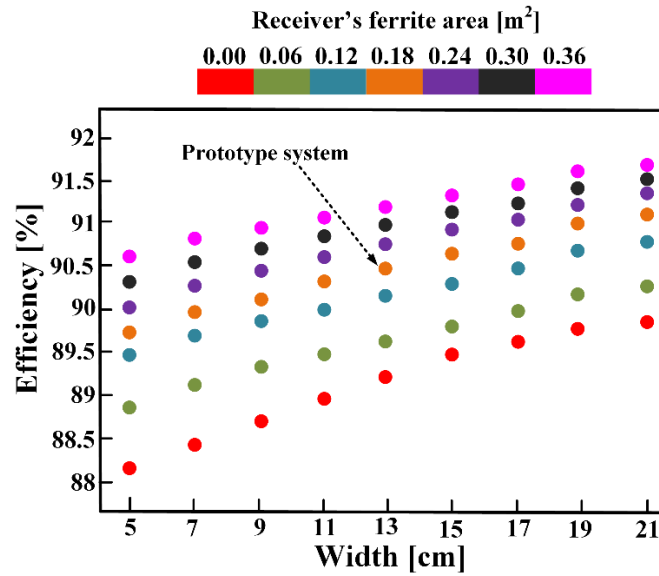
(a)
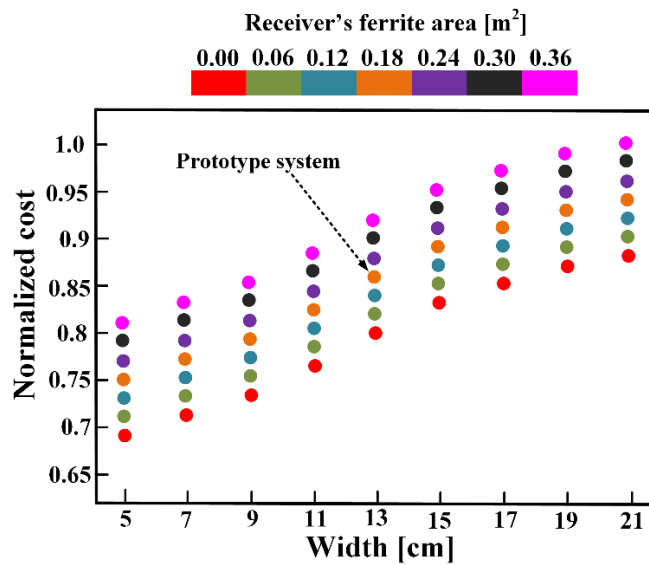
(b)

Fig. 5.6. (a) The efficiency versus transmitter's width and receiver's ferrite area. (b) The normalized cost versus transmitter's width and receiver's ferrite area.

Fig. 5.7 and 5.8 present the relationship between the efficiency and the associated cost with the variations of W_p and A_r. The calculated efficiency varies from 88.23% to 92.56% while the normalized cost factor varies between 0.691 to 1. One can clearly see that there is a trade-off between the efficiency and the associated cost. The maximum efficiency can be attained is 92.56% if the cost factor is set to 1.

Taking everything into consideration including the available resources in Lab to assemble the coupler coils, such as budget and availability of space and material, the proposed coupler is selected with W_p of 13 cm and A_r of 0.18 m². It reflects the cost factor of 0.845 and the calculated efficiency of 90.49%. This selection is heavily dominated by the available resources in the Lab such as budget limitation and availability of space and materials.
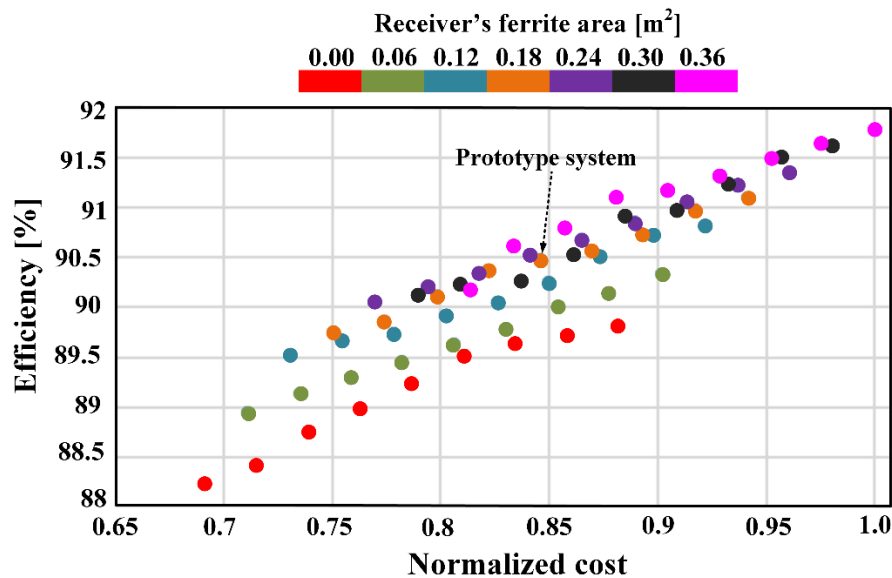
Fig. 5.7. The efficiency versus the normalized cost regarding the variation of receiver's ferrite areas.
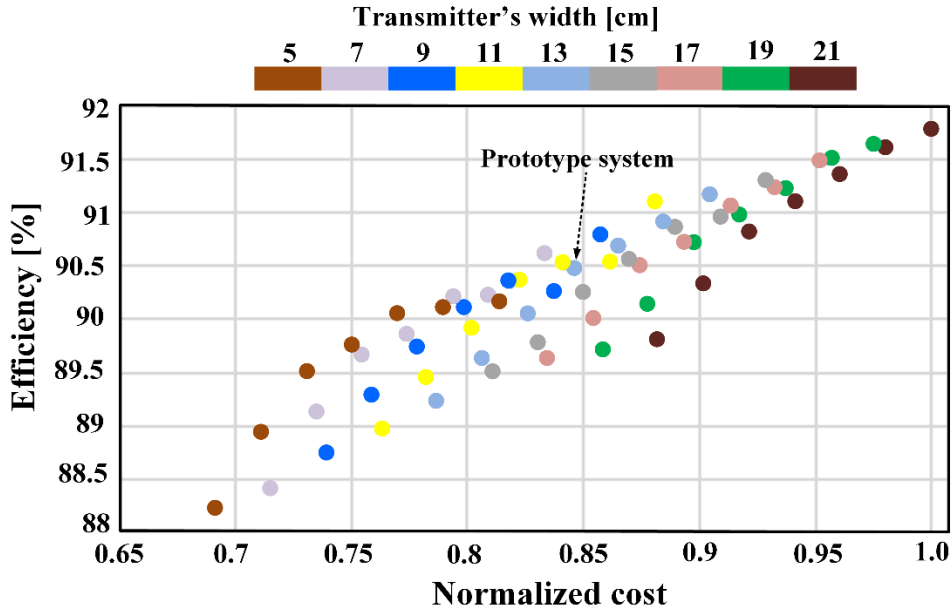
Fig. 5.8. The efficiency versus the normalized cost regarding the variation of transmitter's widths.

Moreover, the data of different 63 operating points from FEA simulation conducted by ANSYS Maxwell 3D is presented in Table 5.6. The table includes W_p, A_r, self-inductances of transmitters L_1 (μH) and receiver L_s (μH), maximum coupling factor k and quality factors of transmitters Q_1 and receiver Q_s. Please note that the three-phase transmitters built using three identical inductances L_1, L_2, and L_3 for which all their self-inductances and quality factor are equal.

TABLE 5.6
THE RESULTING DATA FROM FEA SIMULATION OF COUPLERS

Operating points	W_p (cm)	A_r (m²)	L_1 (μH)	L_s (μH)	k	Q_1	Q_s
1	5	0	131.0154	66.36422	0.063279	349.8636	186.5432
2	7	0	154.325	66.62694	0.066313	412.1095	187.2817
3	9	0	162.4301	66.76452	0.072836	433.7534	187.6684
4	11	0	169.7557	67.10298	0.078296	453.3156	188.6198
5	13	0	177.4497	67.14289	0.083668	473.8618	188.7319

6	15	0	177.6953	67.17173	0.087942	474.5176	188.813
7	17	0	190.6667	67.4409	0.092851	509.1565	189.5696
8	19	0	196.8092	67.47746	0.097393	525.5593	189.6724
9	21	0	203.152	67.64975	0.101604	542.497	190.1567
10	5	0.06	131.2026	88.86068	0.076718	350.3633	249.7785
11	7	0.06	155.4474	89.65048	0.081508	415.1068	251.9985
12	9	0.06	163.6831	89.95244	0.08934	437.0993	252.8473
13	11	0.06	171.4876	90.13876	0.096655	457.9406	253.371
14	13	0.06	179.559	91.47691	0.103525	479.4945	257.1324
15	15	0.06	179.891	89.66167	0.109481	480.3809	252.03
16	17	0.06	193.2706	91.47967	0.115399	516.1098	257.1402
17	19	0.06	199.5265	90.00046	0.120914	532.8156	252.9823
18	21	0.06	206.0002	90.15628	0.126281	550.103	253.4203
19	5	0.12	131.8461	102.019	0.083015	352.0819	286.7653
20	7	0.12	155.5069	103.2305	0.08773	415.2657	290.1706
21	9	0.12	164.6882	103.8133	0.096398	439.7833	291.8087
22	11	0.12	172.3003	104.2788	0.104334	460.1107	293.1172
23	13	0.12	180.6357	104.6963	0.111363	482.3695	294.2907
24	15	0.12	181.0495	104.7364	0.117841	483.4747	294.4036
25	17	0.12	194.1729	102.8572	0.122572	518.5194	289.1213
26	19	0.12	200.2855	104.9497	0.129891	534.8425	295.0031
27	21	0.12	207.1345	103.1101	0.133664	553.132	289.8321
28	5	0.18	132.1148	116.3883	0.088532	352.7994	327.1559
29	7	0.18	156.1918	116.4035	0.093796	417.0945	327.1987
30	9	0.18	164.851	117.134	0.102661	440.2182	329.2519
31	11	0.18	172.8243	117.8515	0.111405	461.51	331.2689
32	13	0.18	180.7808	117.5037	0.118862	482.7569	330.291
33	15	0.18	181.7402	117.5903	0.125814	485.3189	330.5345
34	17	0.18	194.739	118.5951	0.132417	520.031	333.3589
35	19	0.18	201.8807	118.7175	0.138688	539.1023	333.7031
36	21	0.18	208.0775	118.8506	0.144513	555.6502	334.077
37	5	0.24	132.5598	122.9908	0.092885	353.9878	345.7148
38	7	0.24	155.8097	128.5607	0.099335	416.0743	361.3713
39	9	0.24	165.5354	127.0499	0.109387	442.0457	357.1245
40	11	0.24	173.4489	127.995	0.118638	463.178	359.781
41	13	0.24	181.5026	126.8244	0.125917	484.6846	356.4908
42	15	0.24	182.3575	125.6161	0.132339	486.9675	353.0943
43	17	0.24	196.0074	127.5886	0.140066	523.4181	358.6388
44	19	0.24	202.7933	129.0334	0.147252	541.5392	362.6999
45	21	0.24	209.6991	128.1938	0.15338	559.9804	360.3399
46	5	0.3	132.9904	132.4763	0.09901	355.1377	372.3775
47	7	0.3	156.4928	134.7925	0.105942	417.8983	378.8882

5.6 Chapter summary

The parametric-analysis of a three-phase WDC system for EV application in terms of efficiency and cost was demonstrated in this Chapter. A design procedure is proposed based on the input and output specifications in the first step. The parametric-analysis process mainly focused on the coupler design using FEA analysis. The coupler's parameters are fixed and varied to realise different system performances. Building upon Chapter 4, the transmitter's width W_p and receiver's ferrite area A_r are variable.

In order to calculate the system efficiency, the losses calculation is conducted based on the loss model of all components in the prototype such as wireless coupler, inverter, resonant tank, and rectifier. For the cost calculation, a cost model is proposed to determine both fixed and variable costs. For a better presentation, the normalized cost is defined based on the calculated results.

The parametric-analysis results showed trade-off between efficiency and cost. Nevertheless, the prototype in this work is built with a cost factor of 0.845 and an efficiency of 90.49%, taking into account the Lab resources and budget availability.

5.7 References

[1] R. Bosshard, J. W. Kolar, J. Mühlethaler, I. Stevanovi´c, B. Wunsch, and F. Canales, "Modeling and η-α-Pareto optimization of inductive power transfer coils for electric vehicles," IEEE Journal of Emerging and Selected Topics in Power Electronics, vol. 3, no. 1, pp. 50–64, Mar. 2015.

[2] S. Bandyopadhyay, V. Prasanth, P. Bauer, and J. A. Ferreira, "Multiobjective optimisation of a 1-kW wireless IPT systems for charging of electric vehicles," 2016 IEEE Transportation Electrification Conference and Expo (ITEC), Dearborn, MI, Jun. 2016, pp. 1–7.

[3] R. Bosshard, U. Iruretagoyena, and J. W. Kolar, "Comprehensive evaluation of rectangular and double-D coil geometry for 50 kW/85 kHz IPT system," IEEE Journal of Emerging and Selected Topics in Power Electronics, vol. 4, no. 4, pp. 1406–1415, Dec. 2016.

[4] S. Bandyopadhyay, V. Prasanth, J. Dong and P. Bauer "Comparison of Magnetic Couplers for IPT-Based EV Charging Using Multi-Objective Optimization," IEEE Transactions on Vehicular Technology, vol. 68, no. 6, pp. 5416 - 5429, Jun. 2019.

[5] Y. D. Ko and Y. J. Jang, "The optimal system design of the online electric vehicle utilizing a wireless power transmission technology," IEEE Transactions on Intelligent Transportation Systems, vol. 14, no. 3, pp. 1255–1265, Sep. 2013.

[6] S. Jeong, Y. J. Jang, and D. Kum, "Economic analysis of the dynamic charging electric vehicle," IEEE Transactions on Power Electronics, vol. 30, no. 11, pp. 6368–6377, Nov. 2015.

[7] J. Mühlethaler, "Modeling and multi-objective optimization of inductive power components," Ph.D. dissertation, Swiss Federal Inst. Technol. Zurich, ETHZ, Zürich, Switzerland, 2012.

[8] [Online] Characteristics of Mn-Zn ferrite materials - TDK Product Center. Available: https://product.tdk.com.

[9] [Online] Film capacitor.   Available: https://ec.kemet.com/film

[10] [Online] Litz Brochure. Available: http://www.osco.uk.com

CHAPTER 6

Experimental results

6.1 Experimental test-rig

According to the parametric-analysis results in Chapter 5 combined with the available resources in Lab, a laboratory prototype of the 3-kW three-phase WDC with a cost factor of 0.845 is implemented and tested to validate the analysis carried out in previous chapters. The specified power of 3kW is selected for the demonstrator due to this being the smallest possible scale for the EV charging level 1 [1]. As mentioned earlier, the transmitter width W_p is selected as 13 cm while the receiver's ferrite core area A_r is chosen as 1800 cm^2. The photograph of the whole test-rig is shown in Fig. 6.1. Input DC voltage is provided by a DC power supply ESS 400-25 from Electronic Measurements Inc. The efficiency of the system is measured by a Yokogawa WT1600 digital power meter while the waveforms are captured by voltage, current probes and are displayed on a Tektronix MSO 4034 oscilloscope. A Chroma 63210 DC electronic load is used to emulate the EV battery. The resistive load is varied within the test to demonstrate the WDC system with different power levels. In order to measure the component's temperature within the testing, thermal imaging camera FLIR E5 is used. The stray fields level surrounding the coupler is also measured using a SPECTRAN NF-5030 gauss meter. The measured stray field is expected to be smaller than 27 µT within the distance of one metre from the transmitter's centre to guarantee safety for surrounding humans.

The schematic and prototype of the primary side inverter are illustrated in Fig. 6.2. The inverter consists of four legs in which three legs form the three-phase inverter and one spare leg. The switches from U_1 to U_8 are constructed of using SiC MOSFET, C2M0025120D from Cree. The input DC voltage is supplied into the circuit by the header J_6 while the output AC voltages need to go through the header J_{12}. Capacitors (i.e. C_1-C_5) are used for filtering function and high resistances (i.e. R1, R2) are utilized for discharging voltage. The maximum input DC voltage is 450 V. The inverter and gate driver are protected from overcurrent where the current sensors are utilized to measure the inverter's output current. Then the DSP controller will trip the whole system by stopping the PWM signals if overcurrent occurs.
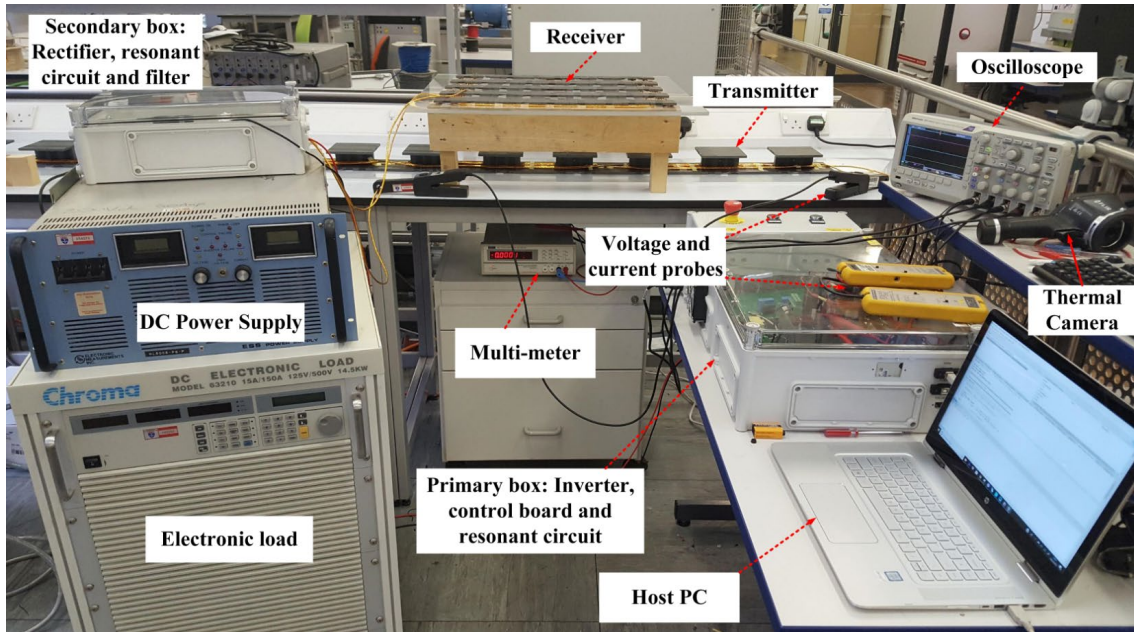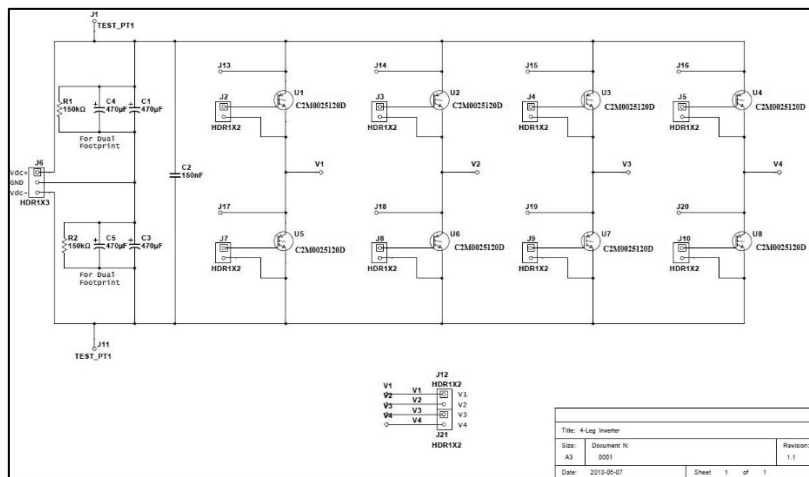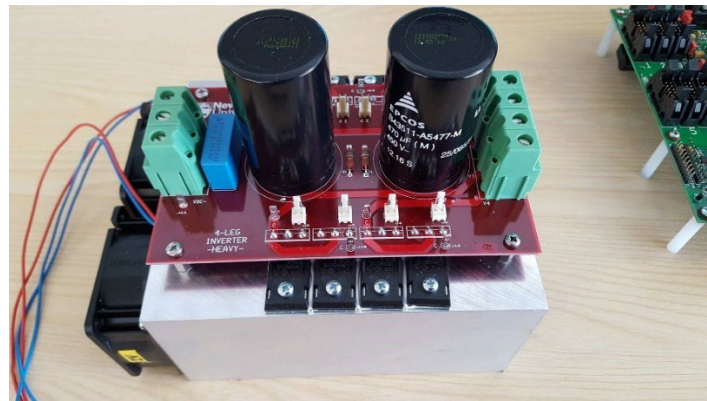
Fig. 6.1. Experimental test-rig of the proposed multiphase WDC system.

(a)

(b)

Fig. 6.2. The primary side inverter. (a) Schematic and (b) Prototype

In order to drive the primary side inverter, the dual-gate driver is utilised for each leg. The driver board contains two identical gate drive circuits and a common input control interface circuit. The gate drive circuit is based on an ACPL-332J opto-coupled driver device. The gate drive circuits can be either operated independently or as a complementary pair when driving two devices in one leg. As the two gate drive circuits are identical, circuit component references are for circuit-A only. The gate drive output circuits are completely isolated from each other and the low voltage control interface. Each gate drive circuit has an isolated DC-DC converter to provide gate drive power. Power and interface signals for both gate drive circuits enter the board on a single 10-way ribbon cable header. The photograph of the gate driver prototype is provided in Fig. 6.3 while detailed design and schematic are given the Appendix A.
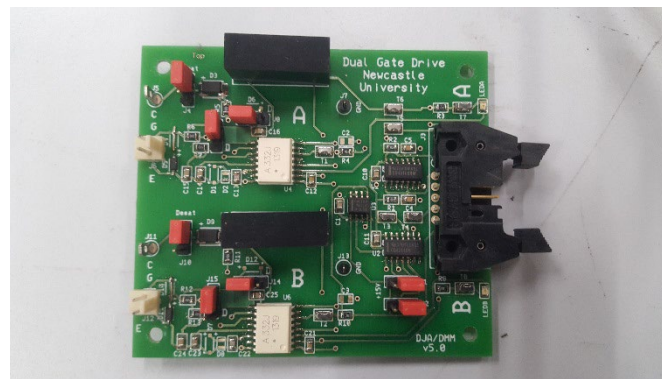

Fig. 6.3. The figure of the dual gate driver's prototype for primary inverter.

The parameters of the transmitter and receiver are tabulated in Table 4.1 of Chapter 4. As shown in Fig. 6.4, the transmitter windings are arranged in three layers isolated from each other using plastic sheets. Furthermore, Kapton-tape-shield litz wire is used to further improve the isolation between different loops of the same phase's winding. The receiver shown in Fig. 6.5 is constructed using five-long-bar ferrite core and eight-turn litz wires. As highlighted in Chapter 4, the dimension of the receiver is 60 cm × 60 cm while the maximum air-gap between the transmitter and receiver is tested at 15 cm. On both sides, the litz wire of 600-strand and s38-AWG from OSCO (UK) is chosen for winding both transmitter and receiver coils to reduce the skin effect and proximity effect losses in the coils' windings. The self-inductances and mutual inductance of the couplers are measured by LCR METER Agilent 4263B. During the testing, the receiver moved manually along the driving direction of the transmitters along with some misalignments to the left or the right are also considered.
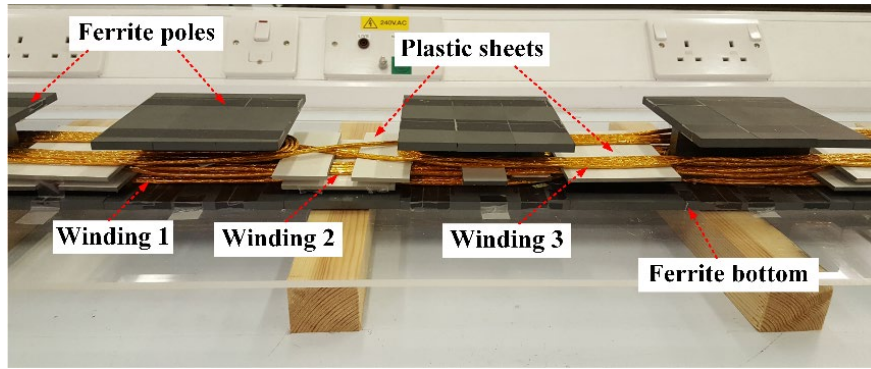
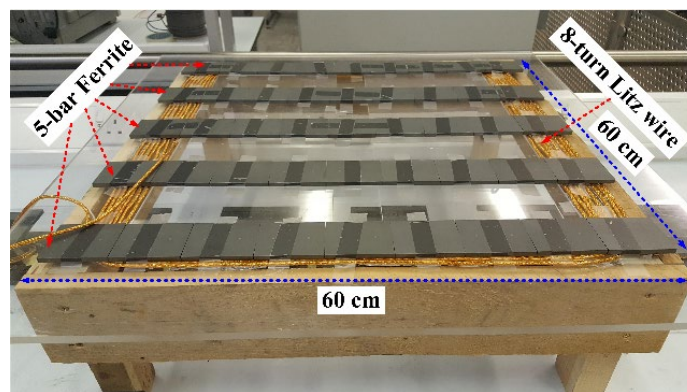Fig. 6.4. Experimental prototype of the three-phase transmitter system.

Fig. 6.5. Experimental prototype of the receiver used in the test.

The SiC- Schottky-diodes, HFA50PA60 are selected for the rectifier on the output side. The operating frequency is selected as standard at 85 kHz [2]. The controller is implemented with a Texas Instruments TMS320F28335 DSP to generate the required PWM signals for the three-phase inverter. The detailed controller implementation is provided in Appendix B. For protection purposes, the input current and voltage are sensed by an LEM LA 55-P current transducer and LEM LV 25-P voltage transducer, respectively. These signals are fed to the general-purpose board to guarantee that the current and voltage in the circuit do not exceed the maximum limits.

Polypropylene film capacitors are chosen for the resonant capacitors owing to their low equivalent series resistance and high current carrying capability. With the power level of 3 kW, then resonant inductors are constructed using ferrite core and litz wire. However, if the power level is higher, then the air-core might be better option to avoid the saturation issues in ferrite cores. Furthermore, the detailed schematic design and layout of these circuits are provided in Appendix A.

In order to meet the Lab safety requirement by conducting the testing, the enclosures are required on both the primary and secondary sides. Fig. 6.6 (a) shows the detailed schematic for the primary enclosure with exact dimensions. It is required that all primary components except the coupler coils are covered inside the enclosure and all components are connected to the outside equipment through the shrouded connectors. Primary components include auxiliary power supply, general control board, driver circuits, inverter, fan, the primary resonant circuit as well as the current sensor. Moreover, in order to display the waveforms into the oscilloscope, then extra spaces for voltage and current probes are required as well. Fig. 6.6 (b) presents the porotype figure of the primary enclosure.
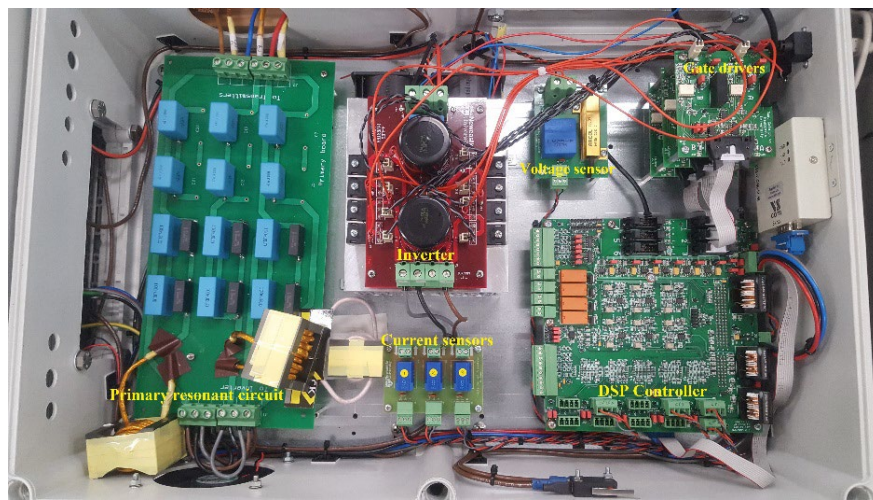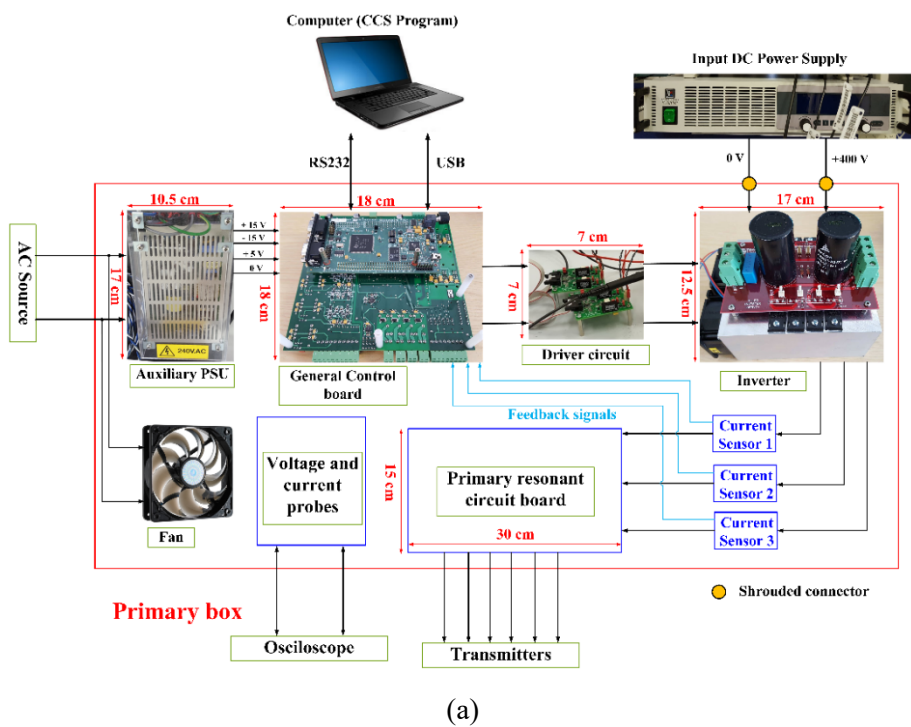

(a)

(b)

Fig. 6.6. Component arrangement and primary enclosure for the test. (a) Schematic. (b) Prototype

The secondary side enclosure is much simpler as it contains only the secondary resonant circuit board, rectifier circuit and voltage (current) probes. It is also required to connect to the outside parts of the receiver and the electronic load through the shrouded connectors. The dimension of the secondary box is much smaller than the primary box. The detailed schematic of the secondary box is displayed in Fig. 6.7.
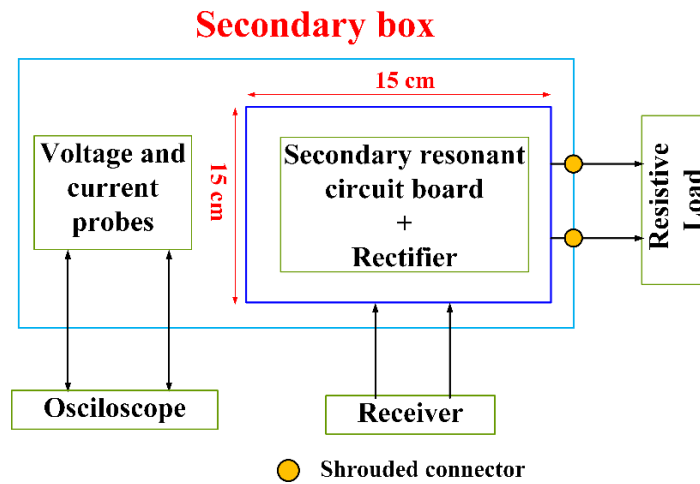
Fig. 6.7. The detailed schematic for the secondary protection enclosure.

The specifications of the proposed WDC are summarized in Table 6.1 along with the parameters of the resonant circuit. It should be noted that the compensation capacitors C_{com1}, C_{com2}, C_{com3} are adjusted from 76.22 nF in simulation to 66.5 nF in the experiment to ensure Zero-Voltage-Switching (ZVS) of all the inverter's switches. Fig. 6.8 illustrates the measured value of mutual inductances between transmitters and receiver when the receiver moves along the driving direction, x.

Fig. 6.8. Measurement of mutual inductances of the three-phase transmitter system.

TABLE 6.1

SPECIFICATION AND PARAMETERS OF THE PROPOSED WDC SYSTEM

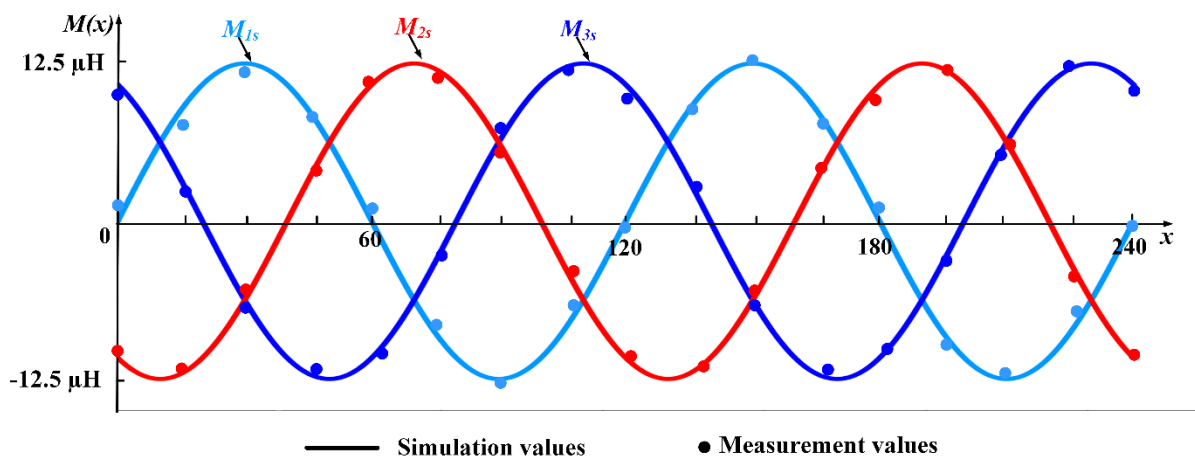| Symbol	Parameter	Simulated values	Practical values
V_{in}	Input voltage	400 V	400 V
I_{bat}	Rated output current	6.5 A	6.45 A
P_o	Rated output power	3 kW	2.91 kW
L_1, L_2, L_3	Self-inductance of transmitters	182 μH	178.6 μH, 180.2 μH, 179.6 μH
L_s	Self-inductance of receiver	118 μH	120.5 μH
M_o	Maximum mutual inductance	12.6 μH	12.48 μH
M_{12}, M_{13}, M_{23}	Crossing mutual inductances	-46 μH	-44.5 μH, -45.8 μH, -47.1 μH
L_{1a}, L_{2a}, L_{3a}	Primary additional inductors	37 μH	36.2 μH, 37.3 μH, 37.5 μH
C_{1a}, C_{2a}, C_{3a}	Primary parallel capacitors	95 nF	95.2 nF, 95.1 nF, 95.2 nF
C_{1b}, C_{2b}, C_{3b}	Primary series capacitors (without compensated capacitors)	24.2 nF	24.2 nF
$C_{com1}, C_{com2}, C_{com3}$	Primary compensated capacitors	76.22 nF	66.5 nF
L_{1s}	Secondary additional inductors	35 μH	36.2 μH
C_{2s}	Secondary parallel capacitors	100 nF	100.6 nF
C_{1s}	Secondary series capacitors	42.2 nF	42.5 nF
f	Switching frequency	85 kHz	85.05 kHz

6.2 Key waveforms of the proposed system

Firstly, in order to verify the performance of the single-phase WDC system, testing with only one phase is conducted. The circuit configuration of the single-phase system is depicted in Fig. 6.9 while the full bridge inverter is adopted. The primary resonant tank utilizes an LCC circuit which consists of L_{1a}, C_{1a} and C_{1b}. The testing was conducted at different positions of the receiver as shown in Fig. 6.10 with the corresponding mutual inductance. For the single-phase experiment, only the first transmitter L_1 was involved (i.e. while other two transmitters are open-circuit) and therefore only M_{1s} was considered.
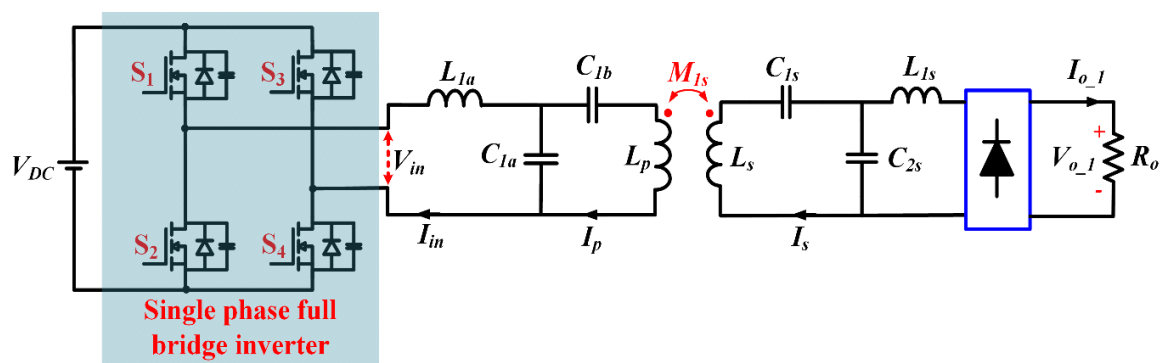

Fig. 6.9. The circuit configuration of the single-phase WDC system.
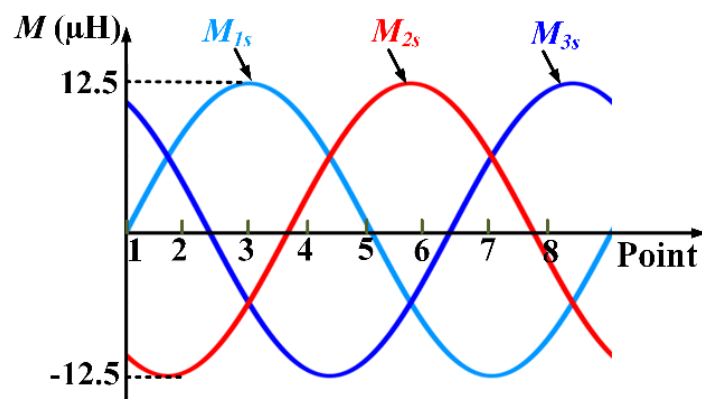
Fig. 6.10. Testing at different receiver positions with the corresponding mutual inductances.

The key waveforms of the single-phase system are shown in Fig. 6.11 in which the load resistance is adjusted to the value of 40 Ω. As described, the receiver is in the process of moving along the driving direction from point 1 => point 3 => point 5. Only one transmitter, L_1 with M_{1s} curve is considered while the other transmitters L_2 and L_3 are open-circuit within the test. Output inverter V_{12}, primary coil current I_p and the receiver current I_s are presented. Fig. 6.11(a) and Fig. 6.11(b) depict the results at points 3 and 5, respectively. Fig. 6.11(c) illustrates the result when the receiver is in motion between point 1 and point 5. In the whole testing process,

the input DC voltage was kept at 400 V, therefore V_{12} and I_p are unchanged. It is clearly shown that the attained power from the receiver is varied (i.e. represented by the receiver current I_s in Fig. 6.11(c)) with the motions of the receiver. The magnitude of I_s and output power are directly proportional to the mutual inductance, M_{1s}. It verifies of the high output power variation when the receiver is in the process of moving.

(a)   (b)
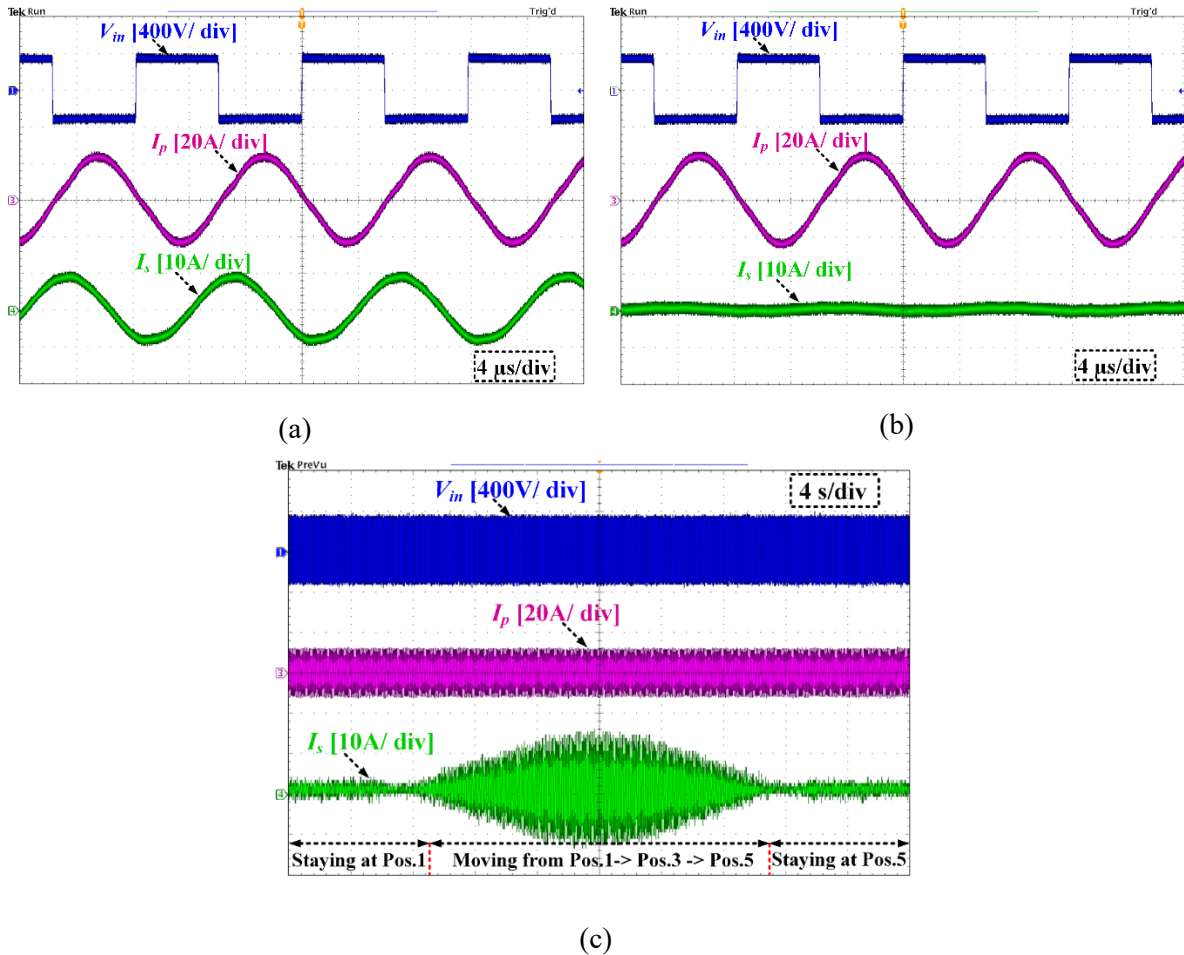

(c)

Fig. 6.11. Experimental waveforms of the single-phase system when the receiver is located at (a) the highest value of M_{1s} at point 3, (b) the lowest value of M_{1s} at point 5 and (c) the receiver moving between point 1 => point 3 => point 5.

Moving to the three-phase system, Fig. 6.12 illustrates the key operating waveforms of the primary side circuit. Specifically, Fig. 6.12(a) depicts the PWM signals of the three-phase inverter, while the inverter's output voltages V_{12}, V_{23} and V_{31} can be seen in Fig. 6.12(b). The corresponding transmitter currents I_1, I_2 and I_3 are shown in Fig. 6.12(c), where they have the same amplitude and a phase-shift of 120 degrees apart from each other. Fig. 6.12(d) depicts the measured voltage V_{ds} and current I_{ds} of the MOSFET switches (i.e. S_1, S_3 and S_5) at the rated power of 3 kW. It can be seen that the turn-on ZVS is achieved for all switches, leading to a significant reduction in switching losses of the inverter.
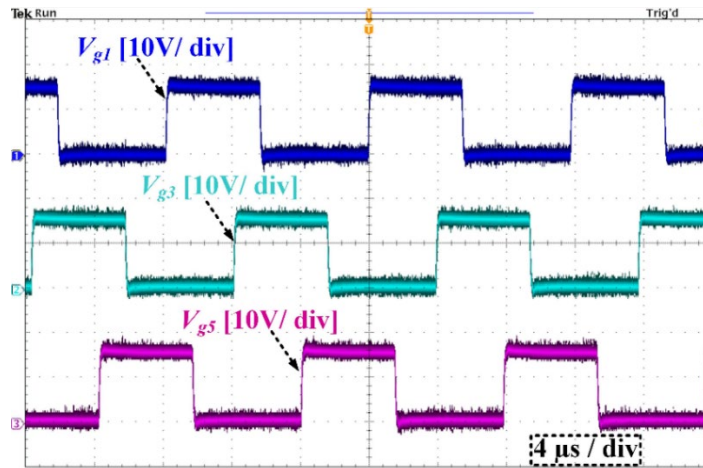
(a)
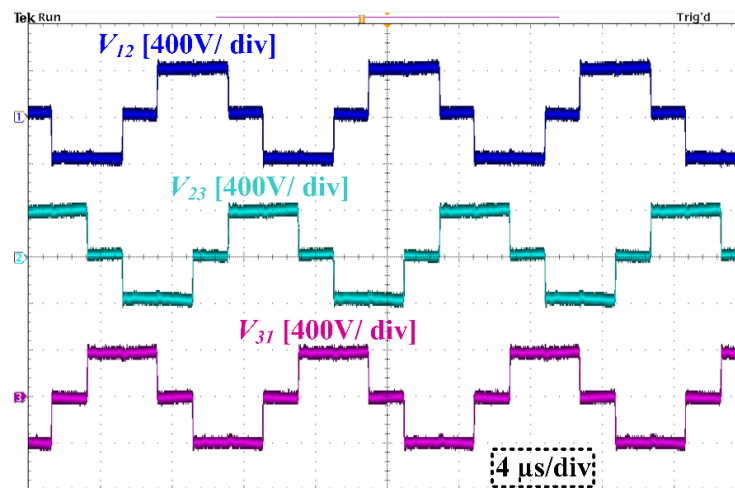
(b)
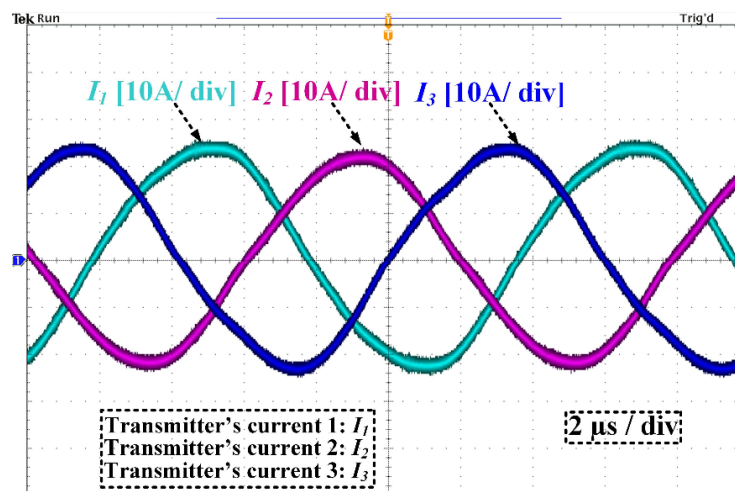
(c)

(d)

Fig. 6.12. Key waveforms of the primary side. (a) Gate signal of the three-phase inverter. (b) Inverter's voltage. (c) Transmitter currents. (d) Inverter switches' voltage V_{ds} and current I_{ds} under the rated load condition (at position 5 of the receiver's displacement).

It is noted that there are small distortions in the current waveforms in Fig. 6.12(c). The possible reason for this issue comes from a measurement error. In detail, the bandwidth of the current probes using in the test bandwidth is smaller 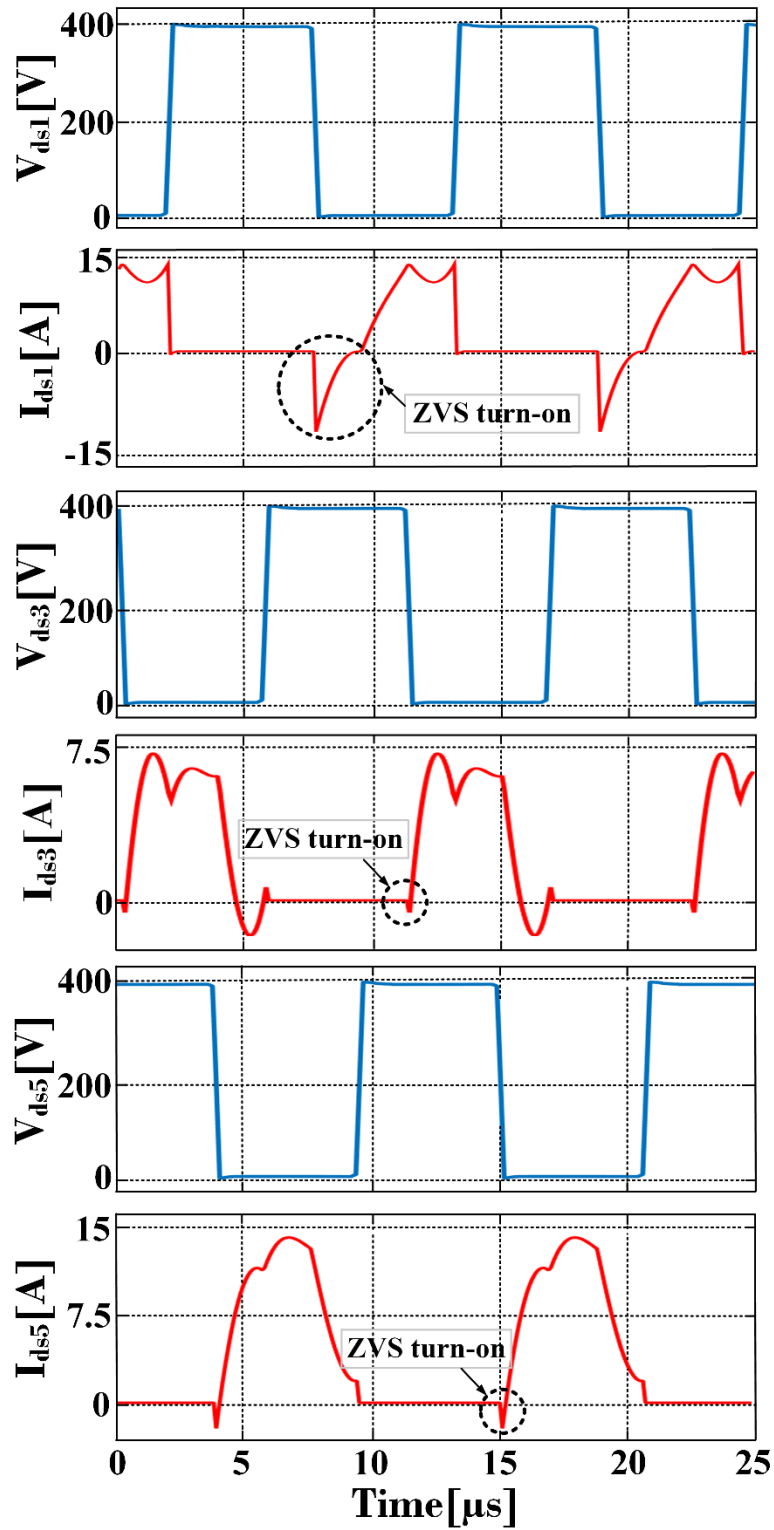than the current frequency (i.e. 85 kHz). Fig. 6.13 further demonstrates the operation of the proposed system under different load conditions (i.e. 17 Ω, 40 Ω and 70 Ω) when the receiver is in motion along with the transmitter. It is noted that the output of the WDC system is a current source as mentioned in chapter 4. Therefore, the DC output voltage has different values when the load resistance changes. The DC output voltage of the WDC system is measured at the steady-state condition while the receiver is in motion along the driving direction. As predicted, the output voltage stays nearly constant regardless of the receiver's positions at different load conditions.
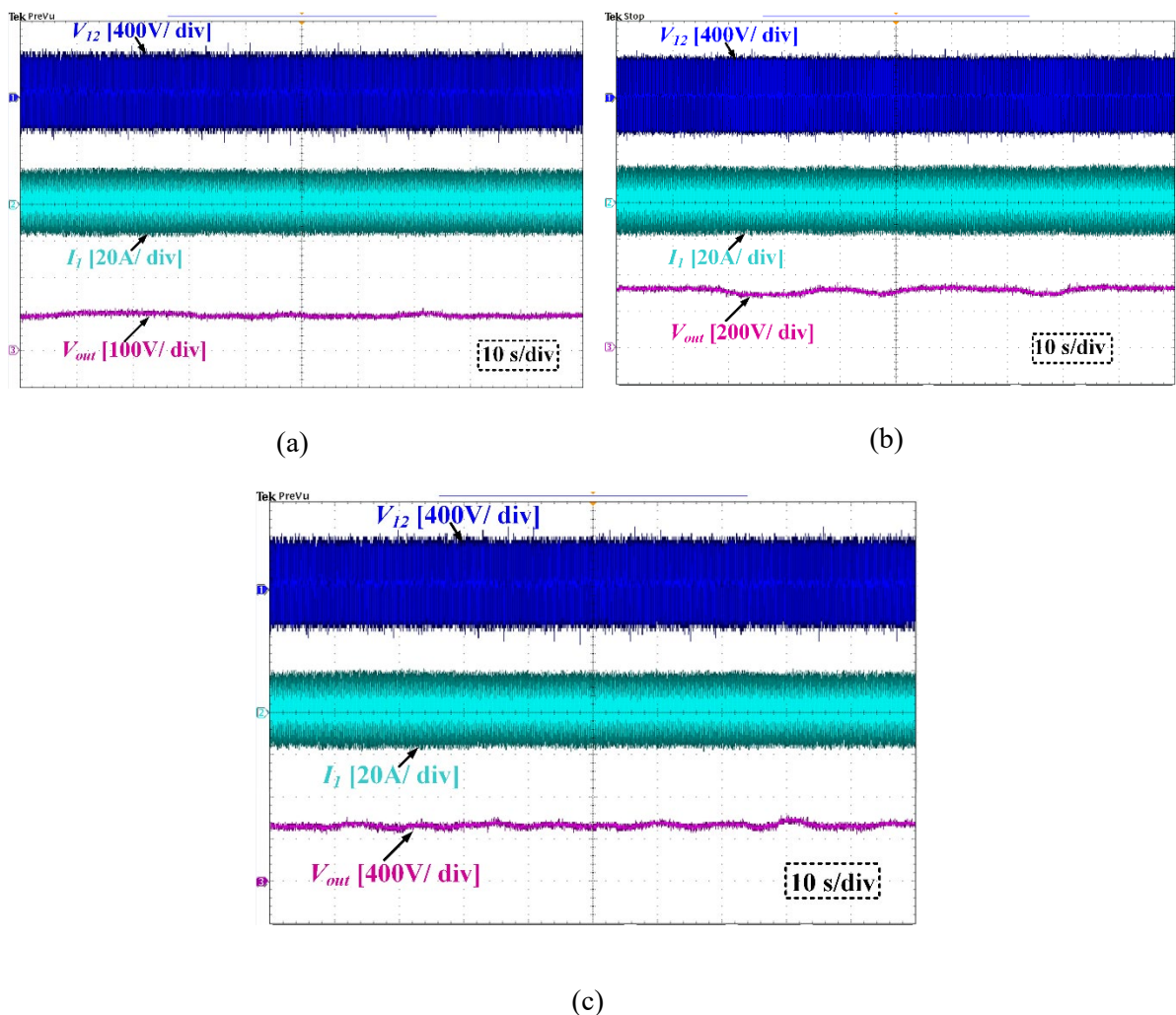

(a)

(b)

(c)

Fig. 6.13. Experimental waveforms with different loads while the receiver moves along the driving direction. (a) $R_o = 17$ Ω. (b) $R_o = 40$ Ω. (c) $R_o = 70$ Ω.

6.3 Output power when the receiver is in motion

The spatial output power variation of the two systems (i.e. single-phase and three-phase) along the driving direction x, of transmitters is measured and compared in Figs. 6.14–6.15. For the single-phase system in Fig. 6.14, the output power (i.e. with a load resistance of 40 Ω) is proportional with the value of $|M_{Is}|$ in which there are four operating points (i.e. x = 0, 60, 120, 180 and 240 cm) where the output power nearly reaches zero.

Fig. 6.14. Measured output power of the single-phase system under different receiver's positions along the driving direction.

Fig. 6.15 presents spatial output power P_o for the three-phase system with different load resistances of 17 Ω, 40 Ω and 70 Ω. It should be noted that x starts only from 15 cm and ends at 225 cm. It is clearly shown that P_o is constant regardless of the receiver's displacement. Moreover, when the load resistance increases, the output power increases accordingly.

Power fluctuation is defined as $\Delta P = \left(\frac{P_{max} - P_{min}}{P_{max}} \right) * 100\%$, where for this particular experiment. ΔP is found to be 4.9%, 5.6% and 5.1% for 17, 40 and 70 Ω loading conditions, respectively.
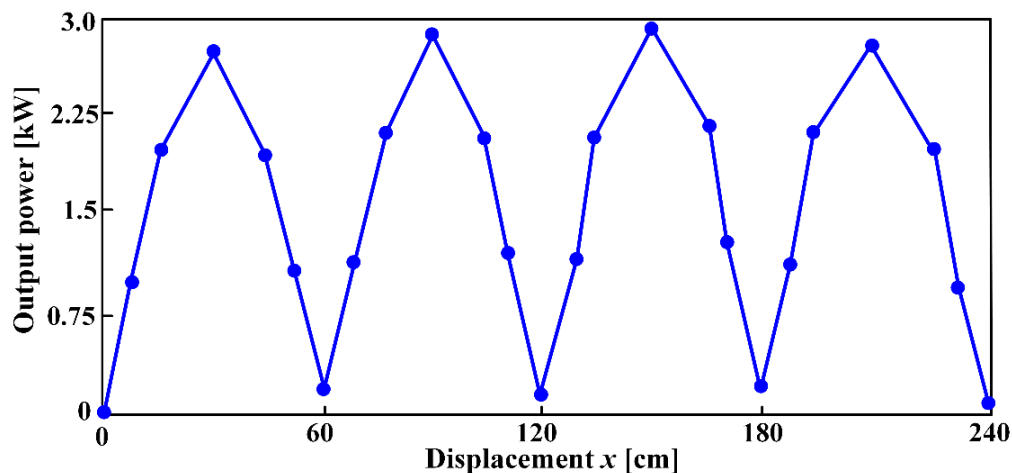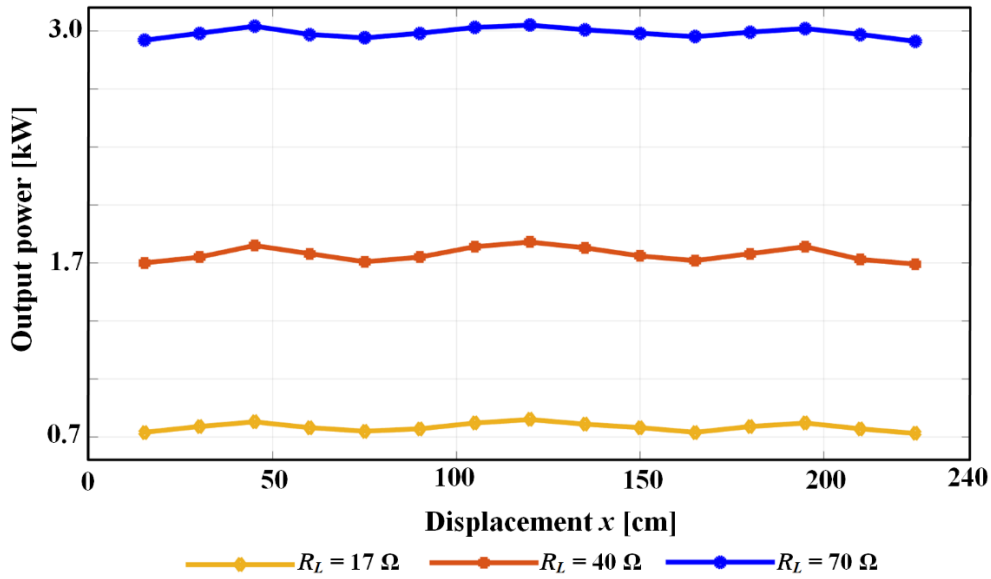
Fig. 6.15. Measured output power of the three-phase system under different receiver's positions along the driving direction.

6.4 Efficiency measurement and losses analysis

Fig. 6.16 compares the efficiency performance of the conventional single-phase system (one transmitter) and the proposed three-phase one. The DC-to-DC efficiency of the WDC system is measured by a Yokogawa WT1600 power meter. During both tests, the receiver only moves along the driving direction from displacement x of 60 cm to 120 cm with the reference point at the beginning of the transmitter. Resistive load is adjusted so that output powers are 1 kW and 3 kW for the single- and three-phase system, respectively. The results indicate that efficiency drops significantly to nearly zero in the single-phase system at the displacements of 60 and 120 cm (i.e. null-mutual-inductance points). Efficiency then increases when the receiver moves either from 70 to 90 cm or in the reverse direction from 110 to 90 cm with a maximum of 89.6% at 90 cm. In contrast with the single-phase system, the proposed three-phase system offers nearly a constant efficiency along the driving direction as the output power is always constant. The highest efficiency was measured around 87.8% at the rated power of 3 kW.
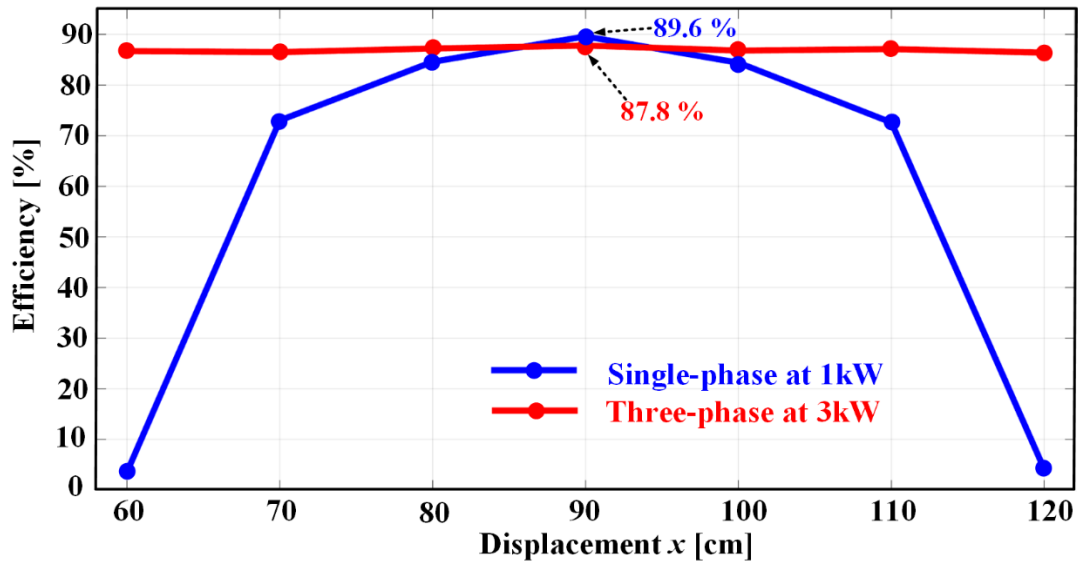
Fig. 6.16. Comparison of measured efficiencies between the single-phase and three-phase systems.

In order to further analyse the results of Fig. 6.16, the loss breakdown is provided in Fig. 6.17 based on the losses model presented in Chapter 5. Both systems have maximum output power of 2.9 kW. Furthermore, it was found that the wireless coils contribute the most percentage of the total losses in both, single- and three-phase systems. For the single-phase system (i.e. Fig. 6.17a), the total losses vary according to different receiver positions. Although output power is zero at several positions such as 1 and 5, there is still around 142 W power loss in the entire circuit, which mainly comes from the primary coil L_1. On the other hand, the losses of the three-phase system are almost constant across the entire travel distance of the receiver, as shown in Fig. 6.17b.
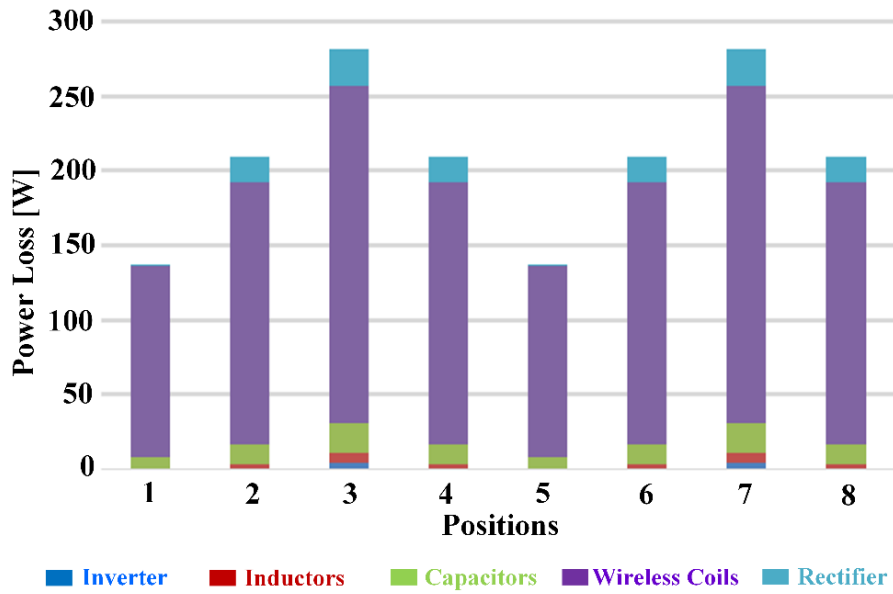
(a)
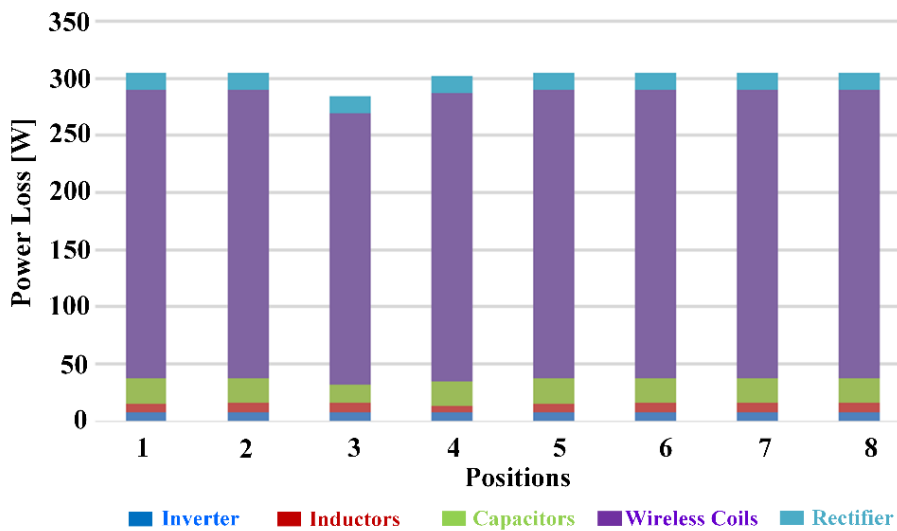
(b)

Fig. 6.17. Losses breakdown of (a) the single-phase and (b) the three-phase WDC systems.

Likewise, the calculated efficiency comparison between the two systems is depicted in Fig. 6.18. As can be clearly seen, the effeceicny of signle-phase system significantly drops at poisitions 1 and 5 and that is due to the zero-mutual-inductance value at these positions. On the other hand, the three-phase system maintains a near-constant efficiency regardless of the receiver position. Although the efficiency of the two systems are similar at maximum-mutual-inductance positions (i.e. Pos. 3 and 7), the single-phase system offers a slightly higher efficiency as compared to the three-phase counterpart (91.4% and 90.7%, respectively).
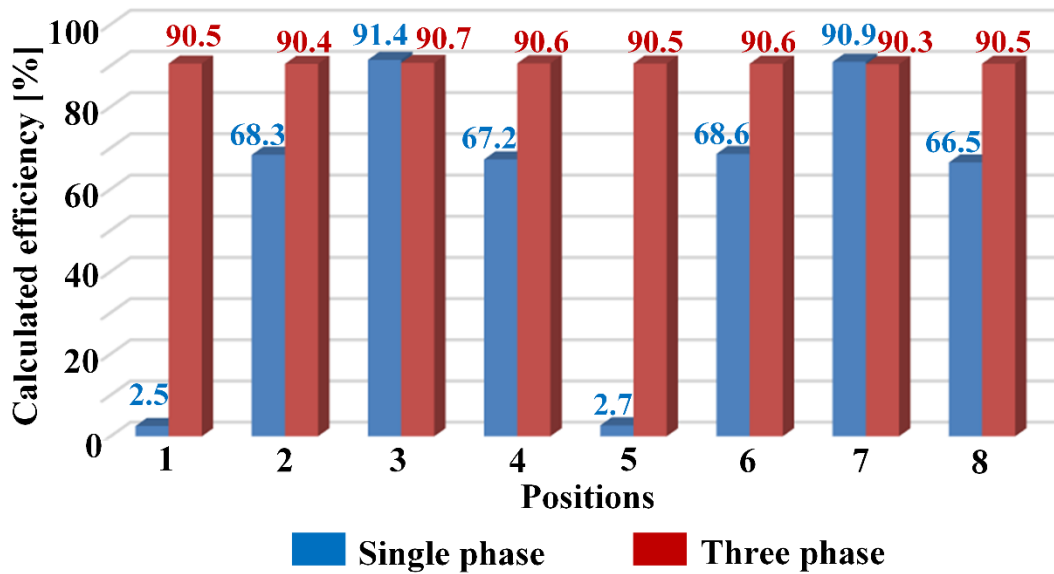
Fig. 6.18. Comparison of calculated efficiencies between the conventional single-phase and the proposed three-phase WDC systems.

The average efficiency comparison between the two systems is depicted in Fig. 6.19 when the receiver travels of a distance of 120 cm. The result shows that 57.26% and 90.49% are achieved for the single-phase and three-phase system, respectively. As efficiency depends heavily on the mutual inductance, the average efficiency of the single-phase system is therefore significantly lower than the three-phase one. This is a strong advantage of the three-phase system over the conventional single-phase one.
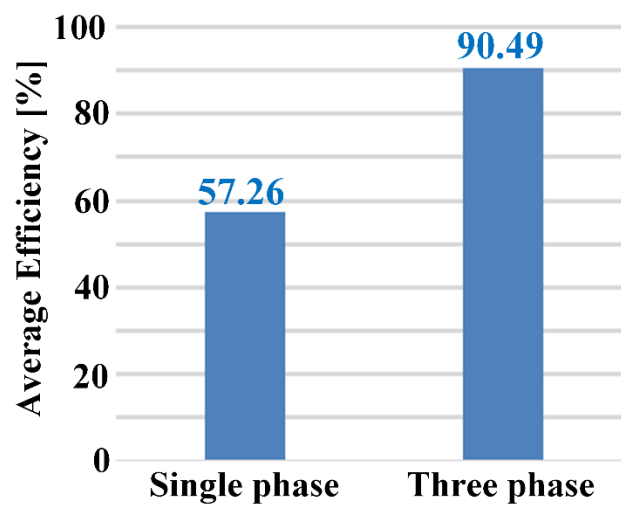
Fig. 6.19. Average efficiency comparison between the two systems for one period of receiver movement.

6.5 System performance under different lateral misalignment

The performance of the proposed WDC is further investigated under lateral misalignment with a different air-gap, *h* of 5, 10 and 15 cm. As demonstrated in Fig. 6.20(a), the output power reduces with higher lateral misalignment between the receiver and the transmitter. The output power also drops as the air-gap between the receiver and transmitter increases. For instance, with 15-cm air-gap and 30-cm misalignment, then the output power drops to as low as 29% of the maximum power of 3 kW. Furthermore, Fig. 6.20(b) illustrates the system efficiency across a wide range of misalignment as well as for different air-gaps. As expected, higher efficiency is attained with smaller misalignment, as can be seen from the same figure.
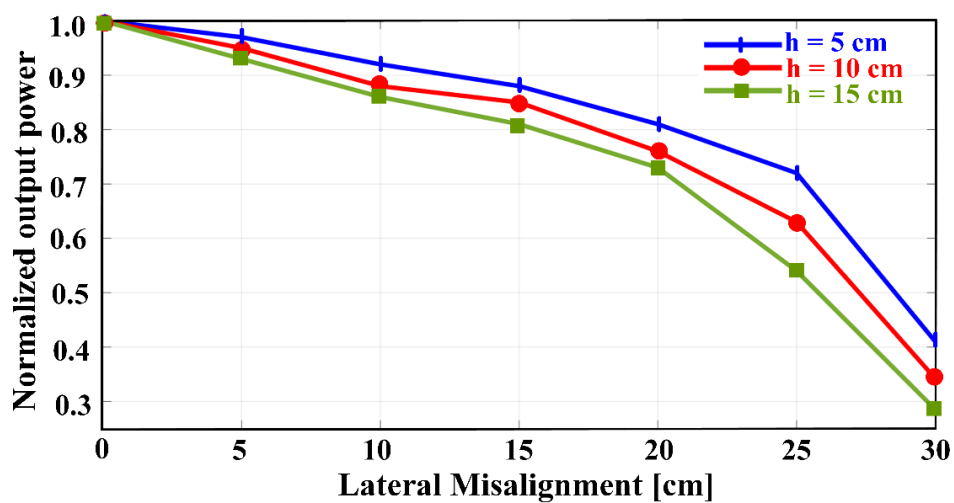
(a)
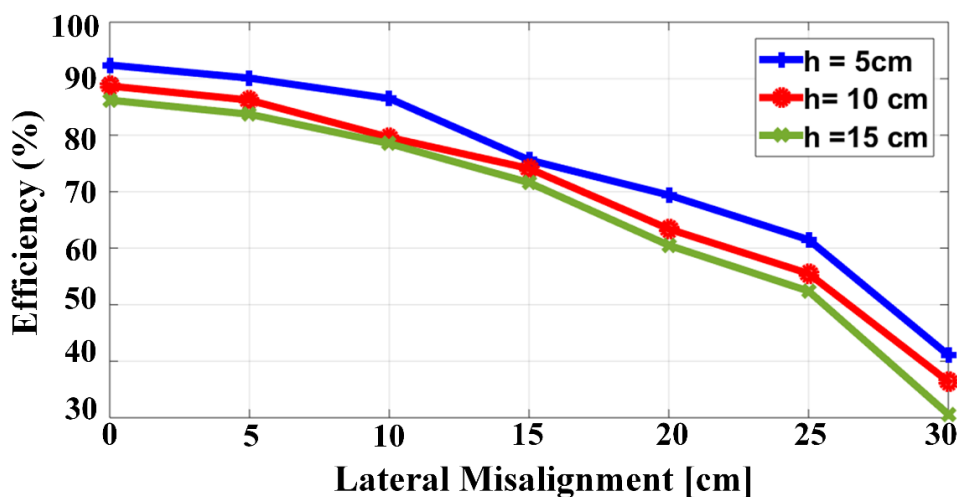
(b)

Fig. 6.20. System performance under different lateral misalignments and airgaps at the rated power (R_o = 70 Ω). (a) Normalized output power. (b) Measured output efficiency.

6.6 Crossing couplings effects

To realise the effect of the crossing couplings between the multiple windings on the performance of the system, in particular, inverter's switches and resonant components; two different tests are carried out with and without compensation capacitors C_{com1}, C_{com2} and C_{com3}. Although the crossing induced voltages by the crossing couplings do not affect the receiver's induced voltage V_s and output power P_o , however, they cause higher current stresses on the inverter and the resonant components L_{ia} and C_{ia}. For that reason, the temperature of the inverter switches changes significantly if these compensation capacitors were included or removed.

In both tests, the temperature of the semiconductor devices of the primary inverter is measured using an FLIR E5 thermal imaging camera. As can be observed from Fig. 6.21(a), before adding the compensation capacitors, the temperature on the power MOSFET reaches 123°C with only 0.2 kW output power and 300 V input DC voltage. However, once the compensation capacitors are added, the temperature does not exceed 105°C at full load (i.e. 3 kW), as shown in Fig. 6.21(b). Hence, the crossing mutual inductances in the multiphase transmitter system must be carefully compensated to attain the maximum power transfer without exceeding the thermal limits.

| (a) | (b) |
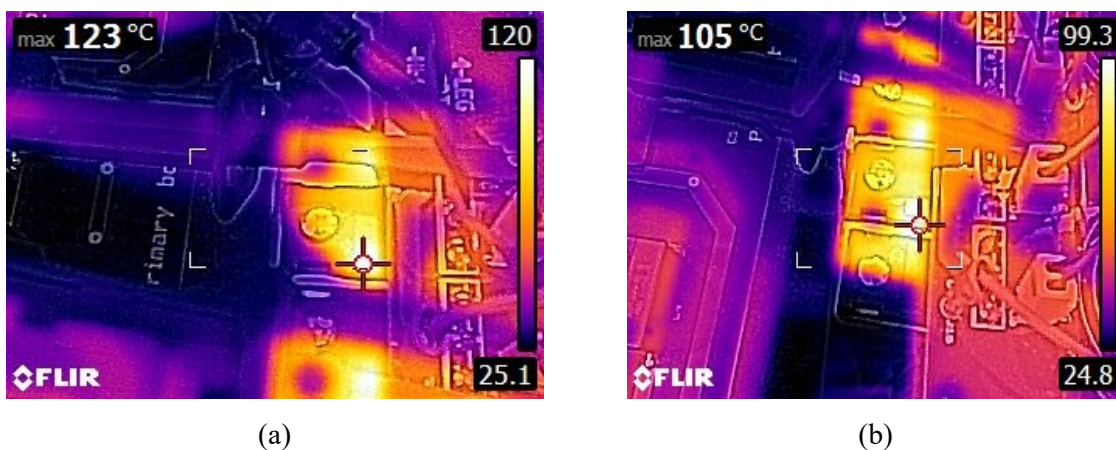
Fig. 6.21. Thermal measurement of inverter's switches (e.g. MOSFET type) under different test conditions. (a) Without compensation capacitors when P_o = 200 W, (b) With compensation capacitors when P_o = 2960 W.

For completeness, the effect of the crossing mutual inductances on the primary side components is also investigated. Table 6.2 summarises the current stress on the inverter switches (S_1, S_2, S_3, S_4, S_5, S_6), the additional inductors (L_{1a}, L_{2a}, L_{3a}) and the parallel capacitors (C_{1a}, C_{2a}, C_{3a}), with and without compensation capacitors. It should be noted that the current

through the series capacitors and the transmitters will not be affected by the crossing mutual inductances. The temperature of power MOSFETs can be very high without compensation capacitors, therefore only simulation results are provided in this case. The parameters of mutual inductances M_{1s}, M_{2s} and M_{3s} in simulation are adjusted to match the experimental parameters (i.e. $M_{1s} = -6.18 \, \mu H, M_{2s} = 12.5 \, \mu H, M_{3s} = -6.27 \, \mu H$). Load resistances in both cases are set as 45 Ω. The difference in current stresses is clearly depicted in Table 6.2 between the two cases, where the RMS currents on switches and components go up to a very high value when compensation capacitors are not included. Conversely, these currents became significantly reduced once the compensation capacitors are included which help to suppress crossing induced voltages on each transmitter.

TABLE 6.2

COMPARISON OF RMS CURRENT STRESSES ON PRIMARY COMPONENTS

Components	Excluding compensated capacitors (simulation results) [A]	Including compensated capacitors (experimental results) [A]
S_1	24.3	1.78
S_2	24.4	7.13
S_3	29.3	6.98
S_4	24.3	1.78
S_5	24.4	7.13
S_6	29.3	6.98
L_{1a}	22.6	3.23
L_{2a}	22.7	6.46
L_{3a}	18.4	3.56
C_{1a}	38.4	18.75
C_{2a}	38.2	18.87
C_{3a}	27.3	14.45

6.7 Magnetic field measurement and safety recommendations

Finally, the stray fields surrounding the transmitter coils is measured at different distances from the coil's centre, d_1 and with different displacement x along the driving direction, as shown in Fig. 6.22. The SPECTRAN NF-5030 gauss meter is used as the measurement sensor

tool. It is understandable that the stray fields level gradually reduces when the measured point is far away from the coupler center.

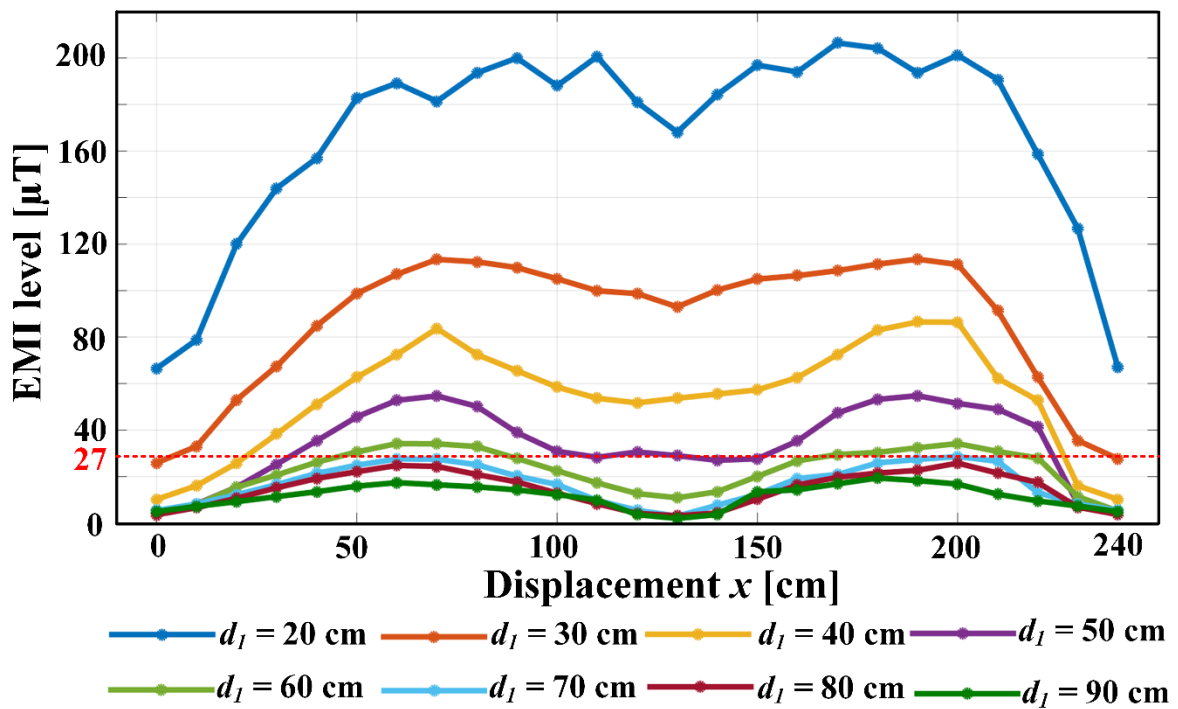Fig. 6.22. Magnetic field measurement at different horizontal conditions.

According to ICNIRP exposure limits [3], the measured flux density below 27 μT needs to be guaranteed for the safety of humans and animals in general. On that basis, the safety level is 0.8 metres away from the transmitter, as shown in Fig. 6.23.
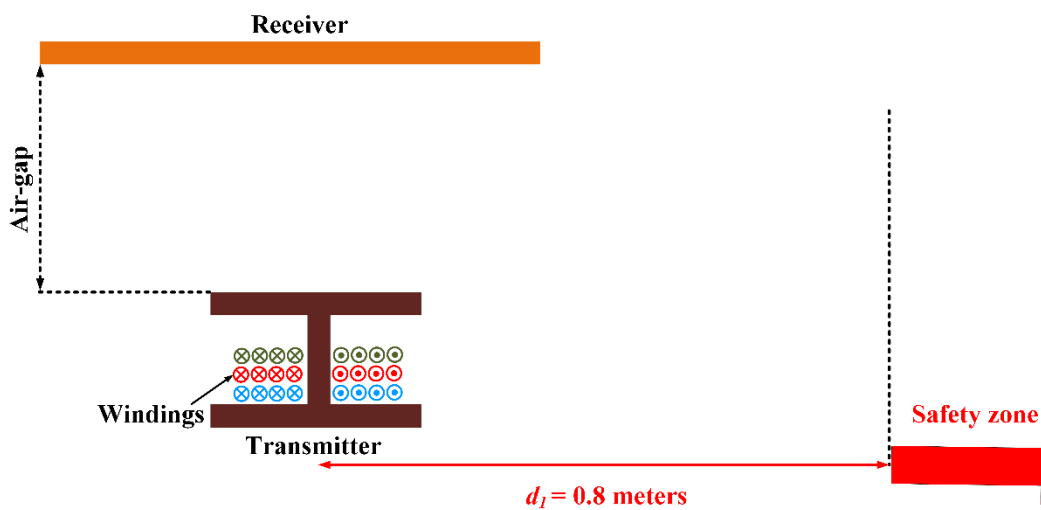

Fig. 6.23. Safety zone in the WDC system of 0.8 metres away from the transmitter.

6.8 Chapter summary

The feasibility of the proposed system was experimentally validated in this chapter using a 3-kW laboratory prototype, which tested under different operating conditions. Firstly, the Lab prototype is described in detail, which includes every component (i.e. inverter, coupler, resonant capacitors, etc.). The key waveforms of voltage and current in both primary and secondary sides are provided.

As expected, the single-phase WDC system suffers from a large power fluctuation while the receiver is in motion along the driving direction. A similar test was also conducted for the three-phase system, where the constant output power feature is verified. According to that, the power fluctuation factor at the rated load is 5.6% while maximum efficiency reaches 87.8%.

The negative effects of crossing couplings on the inverter switches are demonstrated by including or excluding the compensation capacitors, respectively. If compensation capacitors are not used, then the inverter switches will exceed temperature limits even with a small amount of power. Compensating the induced voltages caused by crossing coupling in the multiphase transmitters system is recommended.

Other system performances such as efficiency and magnetic field level are measured and explained in detail. Based on the ICNIRP exposure limits standard, the safety zone for humans and animals is 0.8 metres away from the transmitter's centre with the output power of 3 kW.

6.8 Reference

[1] SAE J1772 - Electric Vehicle and Plug in Hybrid Electric Vehicle Conductive Charge Coupler," published by SAE International, Oct. 2017.

[2] SAE J2954 - Wireless Power Transfer for Light-Duty Plug-in/Electric Vehicles and Alignment Methodology, published by SAE International, Oct. 2020.

[3] "ICNIRP guidelines for limiting exposure to time-varying electric, magnetic and electromagnetic fields (1 Hz to 100 kHz)," Health Physics, vol. 99, pp. 818–836, 2010.
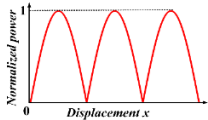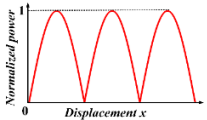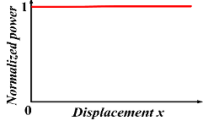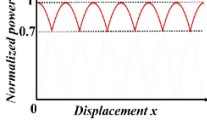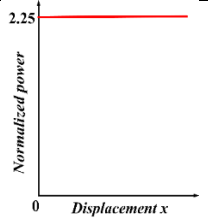
CHAPTER 7

Comparison with other WDC systems

In order to demonstrate the benefits of the proposed multiphase WDC system, a comparison with other similar WDC systems [1-5] that have the advantages of low stray fields and narrow transmitter's width is carried out in this Chapter. It is noted that only the narrow-width transmitter WDC systems are concluded in this chapter. Before performing the comparison, the key features of other systems are summarized. In [1] and [2], the transmitters namely I-type and S-type are proposed with a width of 10 and 4 cm, respectively. Additionally, by adopting the alternating magnetic polarity for adjacent poles, the magnetic stray fields around the transmitter coils can be substantially reduced through electromagnetic field cancelation between two adjacent magnetic poles of opposite polarity. In [3], The N-type transmitter structure is proposed to reduce the volume of ferrite core further while maintaining the advantages of I-type structure in [1]. All WDC systems in [1-3] are the single-phase transmitter where the transmitter coil is powered up by a single-phase full-bridge inverter. Therefore, they all have the disadvantage of power fluctuation while the receiver is in motion. In order to address the above issue, the multi-phase receivers and two-phase transmitters systems are proposed in [4] and [5], respectively.

The first feature to consider is of the output power capability. For the sake of a sensible comparison, the following assumptions are considered: 1) output power is normalized by having the same transmitter current, coupling factor, switching frequency and load resistance for each system. 2) the same compensation circuit at the secondary side of each system. Please note that output power in [3], [4] depends on the number of receiver's windings (phases). The case of two parallel receiver phases is reported here. As it can be seen from Table 7.1, the proposed WDC system offers a constant and high output power (i.e. 2.25 times higher as compared to other systems). This is a clear advantage when high power demand is required.

TABLE 7.1
COMPARISON OF VARIOUS WDC SYSTEMS

	Ref. [1] (Korea Advanced Institute of Science and Technology)	Ref. [2] (Korea Advanced Institute of Science and Technology)	Ref. [5] (Korea Advanced Institute of Science and Technology)	Ref. [3], [4] (Harbin Institute of Technology)	The proposed system (Newcastle University)
Tested Output Power	35 kW	22 kW	250 W (Scale down)	10 kW	3 kW (can be increasable)
Operating frequency (kHz)	20	20	20	20	85
Maximum Efficiency (%)	74	71	-	-	87.6
Normalized output power versus the driving direction*					
Output power variation along driving direction	Not stable	Not stable	Stable	Not Stable	Stable
Number of primary inverters	1 (Single phase full-bridge)	1 (Single phase full-bridge)	2 (Single phase full-bridge)	-	1 (conventional three phase)
Transmitter's width (cm)	10 (I type core shape)	4 (S type core shape)	10 (*dq* I-type core shape)	10 (N type core shape)	12 (*Multiphase* I-type core)
Transmitter's copper length (m)	8000 (1 transmitter's winding)	6000 (1 transmitter's winding)	16000 (2 transmitter's winding)	12000 (1 transmitter's winding)	20400 (3 transmitter's winding)
Receiver's dimension	80 cm x 100 cm (1 winding)	80 cm x 100 cm (1 winding)	90 cm x 100 cm (1 winding)	90 cm x 108 cm (2 windings in parallel*)	60 cm x 60cm (1 winding)
Air gap (cm)	20	20	15	20	15
Possibility of multiple vehicle charging	No	No	No	-	Yes
Load-dependent measurement	Yes	Yes	Yes	Yes	No

Note: - *means no information available from the reference*

* *x-axis expresses different displacement along the driving direction*

Other comparisons can be found from Table 7.1. Apart from [5], other systems are incapable of producing constant power, however two inverters are required in [5] as opposed to only one inverter in the proposed WDC. Although the output power is different from one system to another, however the proposed system achieves higher efficiency, when tested at a full load. This apparently because the system is optimized to achieve the highest magnetic coupling and also the utilization of the state of the art of SiC MOSFETs, which have low on-state resistance.

Interestingly, the control of the secondary side is independent from the primary one, which is not the case with other reported systems. This makes the proposed system more attractive when multiple vehicle charging is needed. However, in the case of other systems, mutual inductances and load resistances information are essential, which makes infeasible with multiple EVs in motion.

On the other hand, transmitter's copper lengths between different systems are calculated and compared for one kilometre of dynamic charging road. It should be noted that the proposed system requires more copper wire at the transmitter side. However, this can be justified with the extra benefits that are gained. Nevertheless, different winding arrangement can be considered to reduce the required copper length as discussed in Chapter 3.3. Finally, the comparison is summarised in Table 7.1.

7.1 References

[1] J. Huh, S. W. Lee, W. Y. Lee, G. H. Cho, and C. T. Rim, "Narrow-width inductive power transfer system for online electrical vehicles," IEEE Transactions on Power Electronics, vol. 26, no. 12, pp. 3666–3679, Dec. 2011.

[2] S. Y. Choi, S. Y. Jeong, B. W. Gu, G. C. Lim, and C. T. Rim, "Ultraslim S-type power supply rails for roadway-powered electric vehicles," IEEE Transactions on Power Electronics, vol. 30, no. 11, pp. 6456–6468, Nov. 2015.

[3] Zhiyuan Wang, Shumei Cui, Shouliang Han, Kai Song, Chunbo Zhu, Milyaev Igor Matveevich, Ostanin Sergei Yurievich, "A Novel Magnetic Coupling Mechanism for Dynamic Wireless Charging System for Electric Vehicles", IEEE Transactions on Vehicular Technology, vol. 67, no. 1, pp. 124-133, 2018.

[4] S. Cui, Z. Wang, S. Han, C. Zhu and C. C. Chan, "Analysis and Design of Multiphase Receiver with Reduction of Output Fluctuation for EV Dynamic Wireless Charging System," IEEE Transactions on Power Electronics, vol. 34, no. 5, pp. 4112–4124, May. 2019.

[5] C. Park, S. Lee, S. Jeong, G.-H. Cho, and C. Rim, "Uniform power I-type inductive power transfer system with DQ-power supply rails for on-line electric vehicles," IEEE Transactions on Power Electronics, vol. 30, no. 11, pp. 6446– 6455, Nov. 2015.

CHAPTER 8
Conclusions and Future Works

There are several technical challenges in implementing wireless dynamic charging (WDC) for electric vehicles. The main challenge is the ability to provide constant and high output power to one or multiple vehicles simultaneously. Other equally important factors include: charging efficiency, magnetic stray fields, implementation cost and system complexity. While not all of the above challenges are easy to address, this work attempted to focus on the transmitter design, which plays an essential role in the WDC system. A summary of the individual findings is given at the end of each previous chapter. Therefore, only the main conclusions are presented in this chapter. Suggestions for future research directions of WDC for EVs are also highlighted.

8.1 Conclusions

WDC systems are free from serious issues regarding the on-board energy storage such as heavy, large, and expensive battery packs as well as long charging time, because the vehicles get power directly from the road while moving. WDC helps to increase the penetration of EVs in the market compared to traditional vehicles. The core element of WDC systems is the transmitter coils, which are broadly classified into short-individual transmitters or long-track transmitters according to the transmitter's length. Each transmitter type has its own advantages and disadvantages. However, they both have some common challenges such as output power fluctuation, the need of high-power capability, high implementation cost, the need of communication between two sides as well as electromagnetic field exposure concern.

The work in this thesis attempted to improve the performance of the WDC system for EV applications by focusing on the transmitter design. Extensive literature studies on different WDC systems have been conducted to identify the main challenges of this technology. Output power fluctuation is found to be one of the most serious problems in WDC, in both short-track and long-track transmitter systems. The main objective of this thesis therefore was to propose and develop a multiphase WDC system to achieve the constant output power when the vehicle is in motion along the driving direction. Moreover, the proposed system was also able to increase the power transfer capability. The core element of the proposed system is the

multiphase transmitters in which the multi windings are combined with the alternative ferrite poles to effectively produce a constant coupling magnetic flux between the transmitters and the receiver. Furthermore, the proposed transmitter layout also helps to mitigate the stray fields level for surrounding pedestrians. The transmitters' detailed layout, winding methods and the conditions of the transmitter currents are analysed and discussed. The design procedure of the multiphase WDC system with three phases is reported as an illustrative example. An optimization analysis of the magnetic coupler using Maxwell 3D simulation is carried out to achieve the highest coupling factor by using minimum ferrite material and copper cable. Besides the output power variation, implementation cost and charging efficiency are also two other important performances. Therefore, the parametric-analysis is demonstrated for the proposed three-phase WDC system in terms of efficiency and cost to realise the trade-off relationship between two factors. All the inverter switches are achieved ZVS to operate under the soft-switching operation, which helps to reduce the system losses. The effectiveness of the proposed system is analytically demonstrated and experimentally verified using a 3-kW laboratory prototype.

The obtained results proved that nearly constant output power with a ripple factor of 5.1% at the rated power can be achieved while the receiver is in motion. This resolves one of the most serious issues of the WDC system. Furthermore, the proposed system has also the advantages of using simple control, which eliminates communications between the primary and secondary side and also delivers a normalized power of 125% higher compared to conventional single-phase systems. By using the best available materials and device technologies combining with the coupler optimization, the high efficiency of 87.6% has been attained at a full load. Although the output power is different from one system to another, the proposed system achieves higher efficiency than other similar WDC systems that have the advantages of low stray fields and narrow transmitter's width. Therefore, the proposed system is a viable candidate as a charging technology for the future electric vehicle systems.

However, the proposed multiphase WDC system has several challenges compared with the conventional single-phase system. Firstly, the multiphase transmitters require more copper wire at the primary side compared to the single-phase transmitter. To minimize the required copper length, different winding arrangements are considered. It is noted that the ferrite core volume is similar between the single-phase and multiphase WDC system. The second challenge related to crossing mutual inductances between different windings of the multiphase transmitters. These mutual inductances induce voltages within each transmitter phase winding

that, cause large current stresses on the inverter and some components of the compensation tank. Consequently, higher temperature and higher conduction losses are observed on the inverter's switches and compensation tank. The most effective way to compensate these above negative effects of crossing mutual inductances is to use compensation capacitors connected in series with each transmitter winding, which has been successfully implemented in the proposed WDC system.

8.2 Future Works

The work presented in this thesis leads to the possibility of further studies as follows:

➢ Investigating the effects of the length of the transmitter coupler to the system efficiency and the total cost when designing a system to cover a certain length of roadway. Longer transmitter coils will require higher inductances and thus higher voltages across the resonant capacitors for a given current.

➢ Studying different receiver coupler topologies for combining with the proposed multiphase transmitter (e.g. circular coil, double-sided D coil, double-sided DQ coil).

➢ Further elimination of power fluctuation under the lateral misalignment of the receiver can be considered by applying the receiver-side control.

➢ Implementing the constant current/constant voltage (CC/CV) charging for the on-board battery. The on-board DC/DC converter may be utilized to implement this task.

➢ Testing the proposed system with different vehicle velocities can be considered.

➢ Design and testing the WDC system with multiple receivers to evaluate the system's performance.

➢ Further investigation of the implementation and maintenance cost at higher power levels. For example, several hundred kW or MW power levels.

➢ Consider the effects of the WDC system on the power network at higher power levels. The worst-case scenario for the network should be in the rush hour (i.e. 4-7 pm). What solutions can be made if the power demand exceeds the supply capability?

➢ Expanding the results for the wireless stationary charging system for electric vehicles, especially when the high-output power capability is required.

Appendix A
Hardware implementation

A.1 Gate drivers

The detailed schematic and design of the dual-gate driver board are presented in this session. The gate drive circuit is based on an ACPL-332J opto-coupled driver device (U2). The ACPL-332J input circuit requires a 5V power supply which is available from the 10-way header (J3).

For high noise immunity, 15V input gate drive signals are used. The gate drive signal inputs PWM-A and PWM-B routed to CD40106BT inverters (U1A and U1B) which have built-in hysteresis for added noise immunity. Pull-up resistors (R1, R2) are provided on the inputs of the CD40106BT to ensure the gate drive outputs are in the OFF condition if inputs (PWM-A, PWM-B) on J3 are not connected. Pads are provided to allow small capacitors (C4, C5) to be fitted at inputs to filter noise if necessary.

The output signals from U1A and U1B are fed to logic which prevents both drives being turned on at the same time (U2A, U2B, J1, J2). This is very important because noise on the input lines can cause this condition even when the gate drive signals from the controller are correct. The jumpers J1 and J2 can be used to enable/disable this logic. The logic comprising gates U1C, U1D and U2C are included for testing purposes only by indicating a potential shoot-through condition on test point T3.

The output signals form U2A and U2B are then routed to U3. This CD40107B CMOS dual 2-input NAND buffer is used to interface the 15V logic signals to the ACPL-332J input LED circuit. To maximise dv/dt immunity, the LED within the ACPL-332J is slightly overdriven by selecting a 1k resistor for R4.

The isolated output side of the ACPL-332J drives the IGBT/MOSFET via connectors J5 and J6. A gate resistor (R6) is included to adjust the power device switching speed. Two back-to-back 18V zener diodes (D4 and D5) are provided between gate and emitter terminals to prevent transient overvoltage due to stray inductance in the gate circuit.

Gate drive output side power is provided by a TMV0515DEC isolated DC-DC converter (U5). The TMV0515DEC is supplied at 5V from connector J3. This device has a high level of isolation which is important for safety and reliability in this application. The DC-DC converter also has a low leakage capacitance in the isolation barrier. This is important to minimise unwanted dv/dt related noise current flowing into the control circuits which may affect sensitive signals.

The gate drive output circuit requires ±15V which is provided by the TMV0515DEC. This bipolar supply allows the gate drive circuit to be configured to apply a negative gate turn-off voltage for preventing dv/dt induced turn-on of the IGBT/MOSFET. Jumpers J8 and J9 are provided to allow different turn-off voltages to be selected. Notes on the circuit schematic diagram (Dual Gate Drive v5.PDF) give details of jumper positions and other component changes. The component values shown on the schematic, are for turn-off voltage options are 0V, -15V and -4.7V. However, with a different choice of zener D6 and resistor R8 it is possible to provide other negative voltage levels.

The ACPL-332J includes DESAT detection to turn off the IGBT/MOSFET in the event of a major short circuit fault. The DESAT sensing circuit includes a fast recovery diode (D3) connected to the IGBT/MOSFET collector (drain) terminal. This diode must be rated for exposure to the power circuit DC bus voltage. The diode protects the gate drive circuit from high voltage when the IGBT/MOSFET is turned off. Under-voltage and DESAT fault protection are built-in features of the ACPL-332J. After DESAT tripping the gate drive is automatically re-enabled on the next switching cycle.

It is important that the track length in the gate circuit loop is short to minimise stray inductance. This stray inductance interacts with the gate capacitance to produce ringing during switching. This can be damped by increasing the gate resistance, but this increases IGBT switching time.

There must be a minimum isolation distance of 5mm between the HV and LV sides of the gate drive circuit and between individual gate drive circuits. This is necessary to minimise stray capacitance and hence the effects of dv/dt induced leakage current as explained earlier.

The gate drive board should be mounted as close as possible to the IGBT/MOSFET it drives. This allows short wiring between the gate drive and the IGBT/MOSFET to minimise gate circuit inductance. The gate-emitter connections should be made using twisted-pair wiring. To drive for the three-phase Inverter, three identical dual-gate drivers are utilized. The schematic and PCB layout for one gate driver are illustrated in Fig. A.1 and A.2, respectively.
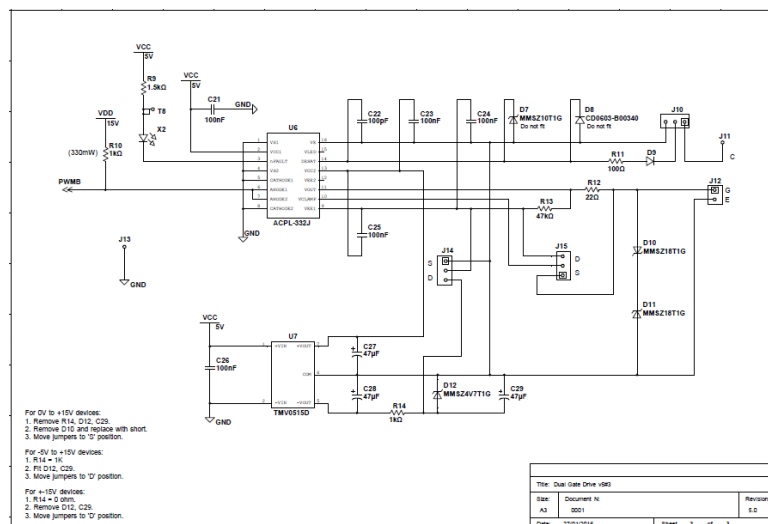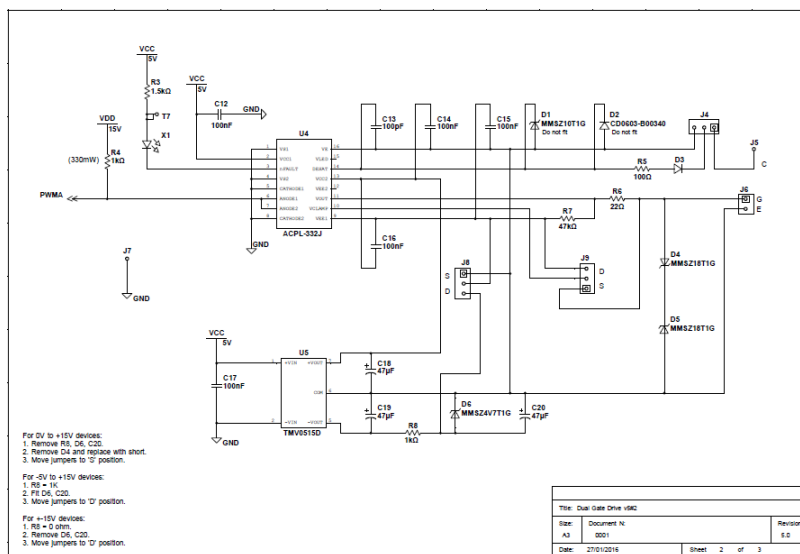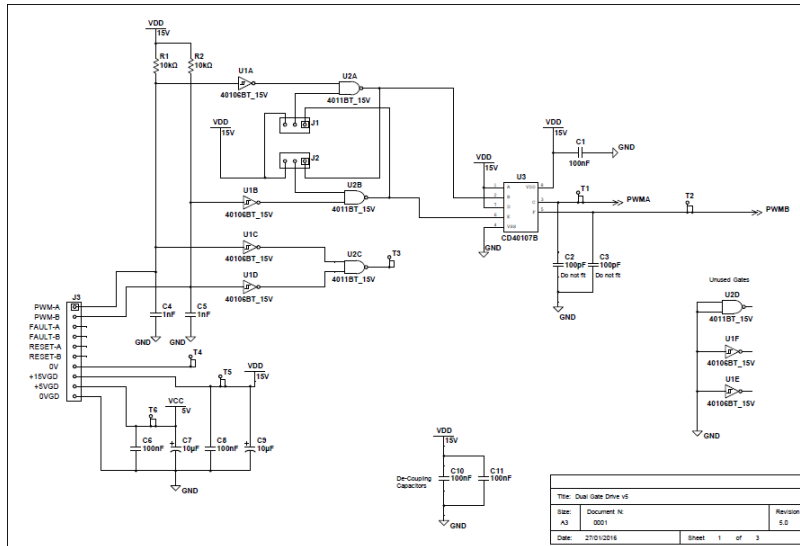
Fig. A.1. Schematic of one gate driver circuits.
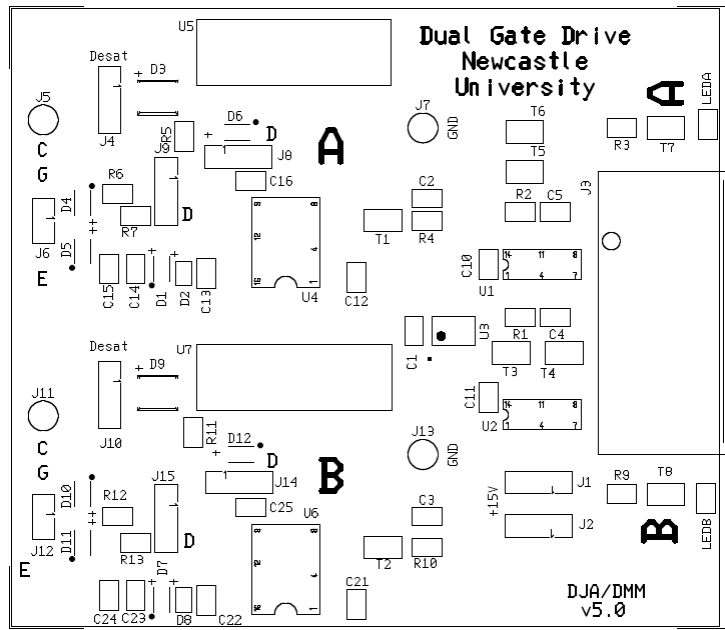
Fig. A.2. Layout of a dual gate driver circuit.

A.2 Resonant tank circuit and rectifier

A.2.1 Primary side

The schematic of primary side resonant circuit can be found in Fig. A.3 while the prototype can be found as a part of Fig. 6.6. As mentioned before, multiple film capacitors are connected in series and parallel to enhance the current rating.
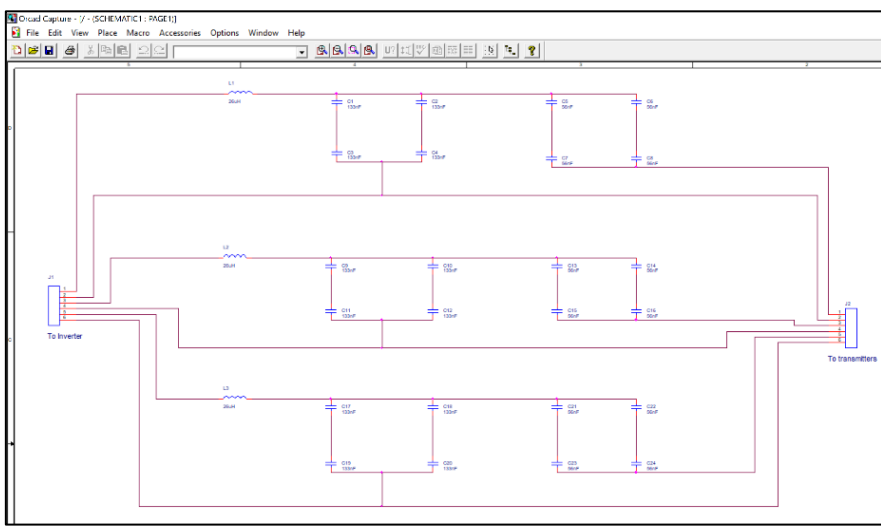
Fig. A.3. Schematic of the primary resonant tank.

A.2.2 Secondary side and rectifier circuit

The secondary resonant tank is combined with the rectifier in the same PCB for more compact. It consists of resonant capacitors, inductor, full-bridge rectifier, and the capacitor filter. Two connectors J1 and J2 are required to connect the board with the receiver coil and the electronic load, respectively. Fig. A.4 provides the circuit schematic while the photograph of the secondary side prototype is shown in Fig. A.5.


Fig. A.4. Schematic of the secondary side circuit.

Fig. A.5. Photograph of the secondary side circuit prototype.

Appendix B
Controller implementation

B.1 Digital Signal Processor (DSP) Board

The power converters are typically digitally controlled by DSP, which is based on electronics (semiconductor) chips. The controller used in this work develops based on the Texas Instrument TMS320F28335 [1]. The DSP board consists of several important parts such as PWM peripheral comprising six pairs of (ePWM) module, analog-to-digital converter (ADC) module with 16 input chan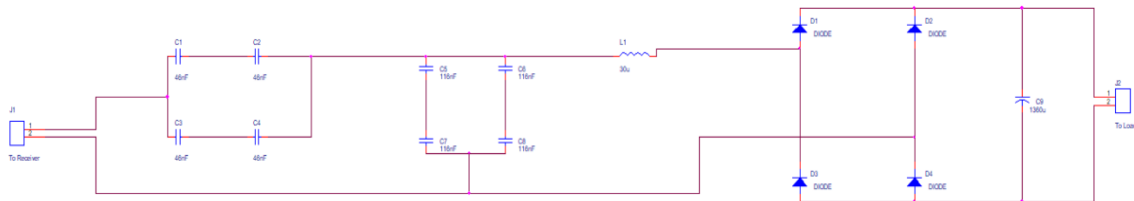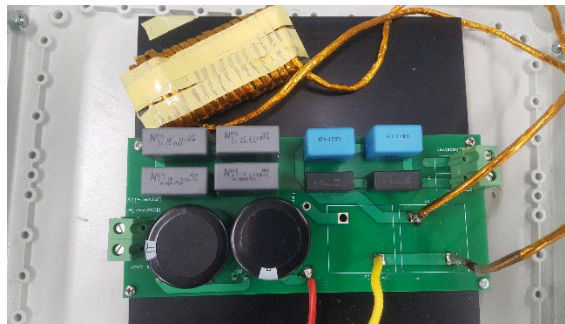nels, two encoder interfaces, etc. The communication task is conducted by four communication ports which can be configured to allow data transfer between the code composer studio (CCS) environment installed in the host computer to the target via JTAG interface. Detail information and specifications of TMS320F28335 DSP board can be found in [2]. In this project, a general-purpose power interface board based on the Spectrum F28335 eZdsp [3] is utilized for control and protection functions. The general-purpose board has been developed at Electrical Power Group, Newcastle University for different types of projects such as high-power converter and control motor [4]. The block diagram of the board can be found in Fig. B1 while the prototype circuit is illustrated in Fig. B2. The board is designed to be flexible, catering for a wide range of power electronic control applications. The on-board interfaces have been designed to cater for a range of different external sensors and gate drive circuits. In some interface sections on the board, links are included to provide options for microcontroller signal use. When interfacing with high voltage, high switching speed power circuits there is always an increased risk of EMI problems. The board layout is designed to minimise these problems. A 4-layer board is used with one of the internal layers dedicated to a common ground plane. The ground plane shape is designed to try and prevent sensitive analog signals being contaminated by digital signal return path currents. In particular, there is a risk of interference from high-frequency leakage currents flowing from the gate drivers. This occurs due to stray capacitance in the gate driver galvanic interface. Separate gate drive power tracks are included to direct these currents away from sensitive parts of the circuit. The following sections of B.2 and B.3 express in details of using the general-purpose board for two functions namely (1) gate drive interface and (2) sensor out-of-range trip circuit
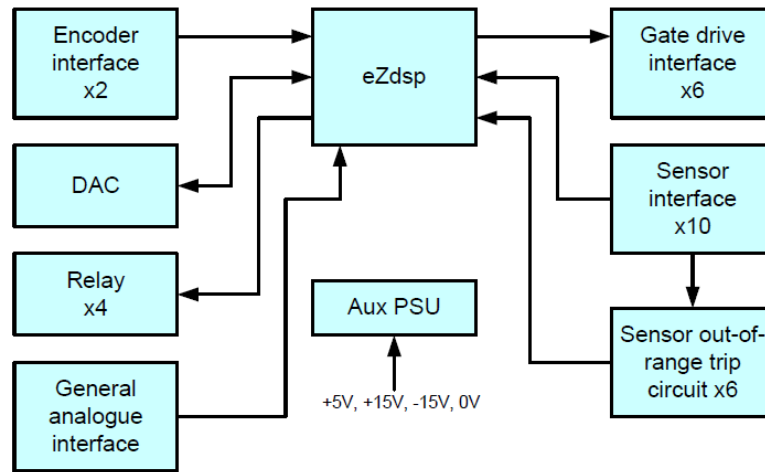
Fig. B.1. The general-purpose power interface board.
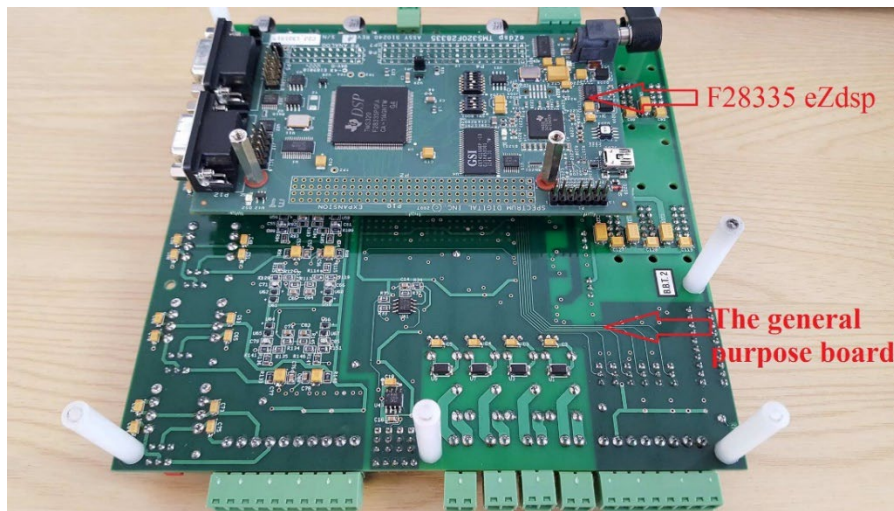
Fig. B.2. The prototype of the general-purpose board including the DSP board.

B.2 Gate drive interface

The gate drive interface allows the eZdsp PWM output pins to interface to external gate drive boards or modules. There are 6 pairs of PWM outputs on the F28335 microcontroller and so 6 interface circuits are provided. Each interface includes two PWM signals. The interface caters to gate drivers with 15V or 5V power requirements. A SN75372 dual MOSFET driver is used to produce the PWM outputs from the board. A link is used to select 5V or 15V for the VCC2 on the SN75372 which sets the output voltage level. Transmitting gate drives signals at 15V gives more noise immunity and is preferred if cables are long.

A separate power track arrangement is provided (+15VGD, +5VGD, 0VGD) for the external gate drive modules and the VCC2 supply on the SN75372. These tracks are routed directly

from the input power connector. This approach is to provide a bypass route around the ground plane for any high-frequency common-mode interference currents flowing from the gate drives.

Often gate drive circuits have a fault indication output signal. A pair of LEDs are provided to indicate the status of these fault signals. Many gate drive modules require a fault reset signal. Two pins Reset-A and Reset-B are provided on the gate drive connector for this function. All reset signals are wired together and driven via a MOSFET from GPIO32 on the microcontroller. The MOSFET is included to boost current levels so that 12 reset signals can be driven if all gate drives are used.
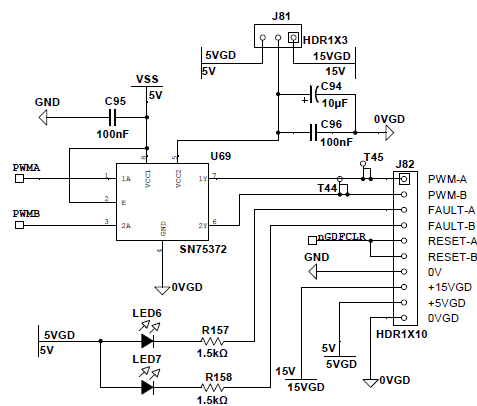
Fig. B.3. The circuit schematic of the gate drive interface.

B.3 Sensor out-of-range trip circuit

This circuit employs a voltage window detector to detect if a sensor signal goes out of the normal range. The most obvious application of this circuit is for fast hardware overcurrent protection. In this work, the window detector is utilized to detect whether the currents from Inverter reach over the limitation or not.

The window detector is based on an LM393 dual voltage comparator. A positive feedback network is included to provide a small amount of hysteresis to prevent oscillation when the comparator switches. The sensor signal is passed through a low pass RC filter before it is monitored by the window detector. A pair of Schottky clamp diodes protect the comparators in the event of overvoltage from the sensor circuit. The comparator ±15V supplies are low-pass filtered with 10R and 0.1uF to prevent noise from entering the device. The upper and lower

trip threshold is set using the trimpots in the potential dividers. The appropriate trip levels are determined by the choice of the sensor as different sensors have different signal voltage ranges. A capacitor to 0V is included on each trimpot slider to filter noise.

The comparators have an open collector output. A logic low condition produces an output close to -15V. Comparator outputs are wire-or'ed so that both positive and negative overvoltage produces a logic low output from the circuit. A link block is used to connect an out-of-range trip circuit output to the microcontroller Trip Zone input pin TZ4/. A Schottky diode is provided to limit the logic low voltage to -0.3V to protect the TZ/ input pin from excessive negative voltage. A small capacitor can be fitted across the TZ4/ input to prevent nuisance tripping on narrow voltage spikes. When all comparator outputs are at logic high, the TZ4/ input is pulled to 3.3V and is therefore inactive. If any comparator output goes low then the TZ4/ input is pulled low. The microcontroller is configured in software so that when the Trip Zone input TZ4/ goes low, it immediately switches off all PWM outputs. The detailed schematic can be found in Fig. B.4 while the input signals are from current sensors that measure the Inverter's output current. These sensors are shown in Fig. B5.
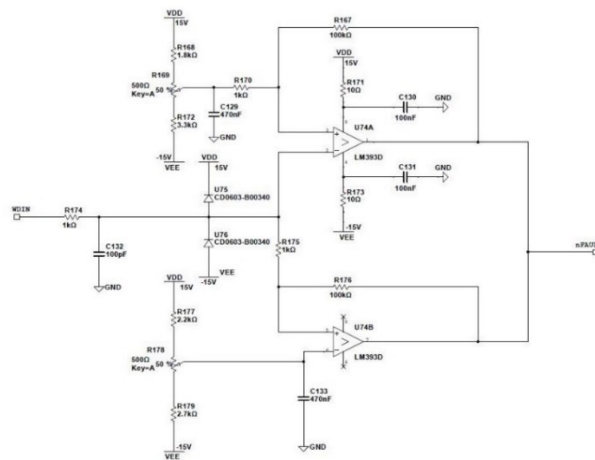

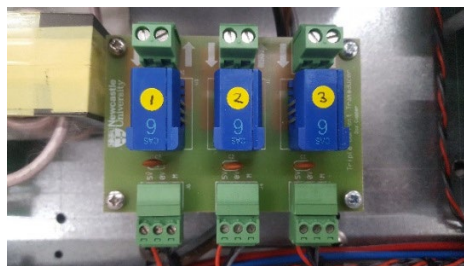Fig. B.4. The circuit schematic of the window detector function.

Fig. B.5. The figure of current sensors of Inverter's output current.

B.4 Software implementation

In order to generate the correct PWM to control the primary three-phase Inverter, a program is coded in the Code Composer Studio 8.0 installed in the host computer. The computer is then connected to the DSP controller via JTAG interface. The following codes are required for the open-loop control loop.

```c
#include "DSP28x_Project.h"      // Device Headerfile and Examples Include File
void Gpio_select(void);
void Setup_ePWM(void);
interrupt void cpu_timer0_isr(void);
//###########################################################################
//          main code
//###########################################################################
void main(void)
{
    int counter=0;  // binary counter for digital output
    InitSysCtrl();  // Basic Core Init from DSP2833x_SysCtrl.c
    EALLOW;
    SysCtrlRegs.WDCR= 0x00AF;   // Re-enable the watchdog
    EDIS;          // 0x00AF  to NOT disable the Watchdog, Prescaler = 64
    DINT;           // Disable all interrupts
    Gpio_select();     // GPIO9, GPIO11, GPIO34 and GPIO49 as output
                    // to 4 LEDs at Peripheral Explorer)

    Setup_ePWM();      // init of ePWM1, ePWM2 and ePWM3
    InitPieCtrl();     // basic setup of PIE table; from DSP2833x_PieCtrl.c
    InitPieVectTable(); // default ISR's in PIE
    EALLOW;
    PieVectTable.TINT0 = &cpu_timer0_isr;
    EDIS;
    InitCpuTimers();    // basic setup CPU Timer0, 1 and 2
    ConfigCpuTimer(&CpuTimer0,150,100000);
    PieCtrlRegs.PIEIER1.bit.INTx7 = 1;
    IER |=1;
    EINT;
```

145

```
        ERTM;
        CpuTimer0Regs.TCR.bit.TSS = 0;  // start timer0
        while(1)
        {
            while(CpuTimer0.InterruptCount == 0);
            CpuTimer0.InterruptCount = 0;
            EALLOW;
            SysCtrlRegs.WDKEY = 0x55;  // service WD #1
            EDIS;
            counter++;
            if(counter&1) GpioDataRegs.GPASET.bit.GPIO9 = 1;
               else GpioDataRegs.GPACLEAR.bit.GPIO9 = 1;
            if(counter&2) GpioDataRegs.GPASET.bit.GPIO11 = 1;
               else GpioDataRegs.GPACLEAR.bit.GPIO11 = 1;
            if(counter&4) GpioDataRegs.GPBSET.bit.GPIO34 = 1;
               else GpioDataRegs.GPBCLEAR.bit.GPIO34 = 1;
            if(counter&8) GpioDataRegs.GPBSET.bit.GPIO49 = 1;
               else GpioDataRegs.GPBCLEAR.bit.GPIO49 = 1;
        }
}
void Gpio_select(void)
{
    EALLOW;
    GpioCtrlRegs.GPAMUX1.all = 0;      // GPIO15 ... GPIO0 = General Puropse I/O
    GpioCtrlRegs.GPAMUX1.bit.GPIO0 = 1; // ePWM1A active
    GpioCtrlRegs.GPAMUX1.bit.GPIO1 = 1; // ePWM1B active
    GpioCtrlRegs.GPAMUX1.bit.GPIO2 = 1; // ePWM2A active
    GpioCtrlRegs.GPAMUX1.bit.GPIO3 = 1; // ePWM2B active
    GpioCtrlRegs.GPAMUX1.bit.GPIO4 = 1; // ePWM3A active
    GpioCtrlRegs.GPAMUX1.bit.GPIO5 = 1; // ePWM3B active

    GpioCtrlRegs.GPAMUX2.all = 0;      // GPIO31 ... GPIO16 = General Purpose I/O
    GpioCtrlRegs.GPBMUX1.all = 0;      // GPIO47 ... GPIO32 = General Purpose I/O
    GpioCtrlRegs.GPBMUX2.all = 0;      // GPIO63 ... GPIO48 = General Purpose I/O
```

```
    GpioCtrlRegs.GPCMUX1.all = 0;        // GPIO79 ... GPIO64 = General Purpose I/O
    GpioCtrlRegs.GPCMUX2.all = 0;        // GPIO87 ... GPIO80 = General Purpose I/O

    GpioCtrlRegs.GPADIR.all = 0;
    GpioCtrlRegs.GPADIR.bit.GPIO9 = 1;  // peripheral explorer: LED LD1 at GPIO9
    GpioCtrlRegs.GPADIR.bit.GPIO11 = 1; // peripheral explorer: LED LD2 at GPIO11

    GpioCtrlRegs.GPBDIR.all = 0;         // GPIO63-32 as inputs
    GpioCtrlRegs.GPBDIR.bit.GPIO34 = 1; // peripheral explorer: LED LD3 at GPIO34
    GpioCtrlRegs.GPBDIR.bit.GPIO49 = 1; // peripheral explorer: LED LD4 at GPIO49
    GpioCtrlRegs.GPCDIR.all = 0;         // GPIO87-64 as inputs
    EDIS;
}


void Setup_ePWM(void)
{
    EPwm1Regs.TBCTL.bit.CLKDIV =  0;    // CLKDIV = 1
    EPwm1Regs.TBCTL.bit.HSPCLKDIV = 1; // HSPCLKDIV = 1
    EPwm1Regs.TBCTL.bit.CTRMODE = 2;    // up - down mode
    EPwm1Regs.AQCTLA.all = 0x0006;      // ZRO = set, PRD = clear
    EPwm1Regs.TBPRD = 442;         // 85KHz - PWM signal

    EPwm1Regs.CMPA.half.CMPA  = 221;    // 50% duty cycle first

    EPwm1Regs.DBRED = 30;               // 10 microseconds delay
    EPwm1Regs.DBFED = 30;               // for rising and falling edge
    EPwm1Regs.DBCTL.bit.OUT_MODE = 3;  // ePWM1A = RED
    EPwm1Regs.DBCTL.bit.POLSEL = 2;    // S3=1 inverted signal at ePWM1B
    EPwm1Regs.DBCTL.bit.IN_MODE = 0;   // ePWM1A = source for RED & FED

    // For initializing a pair of EPwm2
    EPwm2Regs.TBCTL.bit.CLKDIV =  0;    // CLKDIV = 1
    EPwm2Regs.TBCTL.bit.HSPCLKDIV = 1; // HSPCLKDIV = 1
    EPwm2Regs.TBCTL.bit.CTRMODE = 2;    // up - down mode
```

```
    EPwm2Regs.AQCTLA.all = 0x0006;      // ZRO = set, PRD = clear
    EPwm2Regs.TBPRD = 442;         // 85KHz - PWM signal


    EPwm2Regs.DBRED = 30;               // 10 microseconds delay
    EPwm2Regs.DBFED = 30;               // for rising and falling edge
    EPwm2Regs.DBCTL.bit.OUT_MODE = 3;   // ePWM1A = RED
    EPwm2Regs.DBCTL.bit.POLSEL = 2;     // S3=1 inverted signal at ePWM2B
    EPwm2Regs.DBCTL.bit.IN_MODE = 0;    // ePWM3A = source for RED & FED

//   EPwm1Regs.TBCTL.bit.SYNCOSEL = 1;  // generate a syncout if CTR = 0


    EPwm2Regs.TBCTL.bit.PHSEN = 1;      // enable phase shift for ePWM2
    EPwm2Regs.TBCTL.bit.SYNCOSEL = 0;   // syncin = syncout
//  EPwm2Regs.TBPHS.half.TBPHS = 221;   // 1/2 phase shift Update 6 Oct 2017
    EPwm2Regs.TBPHS.half.TBPHS = 442;   // 1/2 phase shift Update 6 Feb 2018


    // For initializing a pair of EPwm3


    EPwm3Regs.TBCTL.bit.CLKDIV =  0;    // CLKDIV = 1
    EPwm3Regs.TBCTL.bit.HSPCLKDIV = 1;  // HSPCLKDIV = 1
    EPwm3Regs.TBCTL.bit.CTRMODE = 2;    // up - down mode
    EPwm3Regs.AQCTLA.all = 0x0006;      // ZRO = set, PRD = clear
    EPwm3Regs.TBPRD = 442;         // 85KHz - PWM signal


    EPwm3Regs.DBRED = 30;               // 10 microseconds delay
    EPwm3Regs.DBFED = 30;               // for rising and falling edge
    EPwm3Regs.DBCTL.bit.OUT_MODE = 3;   // ePWM3A = RED
    EPwm3Regs.DBCTL.bit.POLSEL = 2;     // S3=1 inverted signal at ePWM3B
    EPwm3Regs.DBCTL.bit.IN_MODE = 0;    // ePWM3A = source for RED & FED


    EPwm1Regs.TBCTL.bit.SYNCOSEL = 1;  // generate a syncout if CTR = 0


    //Delay for EPwm2
    EPwm2Regs.TBCTL.bit.PHSEN = 1;      // enable phase shift for ePWM2
```

```
    EPwm2Regs.TBCTL.bit.SYNCOSEL = 0;   // syncin = syncout
    EPwm2Regs.TBPHS.half.TBPHS = 295;   // 2/3 phase shift Update 30 Aug 2018



    //Delay for EPwm3
    EPwm3Regs.TBCTL.bit.PHSEN = 1;      // enable phase shift for ePWM3
    EPwm3Regs.TBPHS.half.TBPHS = 589;   // 4/3 phase shift for EPwm3
}


interrupt void cpu_timer0_isr(void)
{
    CpuTimer0.InterruptCount++;
    EALLOW;
    SysCtrlRegs.WDKEY = 0xAA;   // service WD #2
    EDIS;
    PieCtrlRegs.PIEACK.all = PIEACK_GROUP1;
}
//===============================================================================
// End of SourceCode.
//===============================================================================
```

B.5 References

[1] TMS320F28335, *Analog-to-Digital Converter (ADC) Module.* Texas Instrument, Reference Guide SPRU812A, 2007.

[2] TMS320F28335, T.F., TMS320F28332, *Digital Signal Controllers (DSCs).* Texas Instrument, Data Manual SPRS439B, 2007.

[3] eZdsp TM F28335, *Technical Reference*, Spectrum Digital, Inc, 2007. Available online at http://c2000.spectrumdigital.com/ezf28335/docs/ezdspf28335c_techref.pdf

[4] Dave Atkinson, *General Purpose Power Interface Board*, Newcastle University, 2016.